Universität Ulm
Sektion Kernresonanzspektroskopie

Electro-hydrodynamic investigations of fluids in complex systems by NMR mapping experiments and computer simulations

DISSERTATION

zur Erlangung des Doktorgrades Dr. rer. nat.
der Fakultät Naturwissenschaften
der Universität Ulm

vorgelegt von
Bogdan Buhai
aus Dej, Rumänien

Ulm, 2006

Amtierender Dekan: Prof. Dr. Klaus-Dieter Spindler

Erstgutachter: Prof. Dr. Rainer Kimmich

Zweitgutachter: Prof. Dr. Harmut Jex

Tag der Promotion:

Electro-hydrodynamic investigations of fluids in complex systems by NMR mapping experiments and computer simulations

Abstract

Nuclear Magnetic Resonance (NMR) techniques offer valuable insights into the transport phenomena in complex systems like porous media. This cumulative thesis presents a number of experimental NMR mapping techniques for retrieving and recording valuable information about transport quantities in simple and complex geometries. NMR investigation protocols have been developed for velocity mapping, acceleration mapping, ionic current density mapping and electro-hydrodynamic mapping. Complementary information about the same objects can be obtained in most situations with the aid of Computational Fluid Dynamics (CFD) simulations. This procedure allowed us a direct comparison between the experimental and simulated data. The simple objects presented here are to be seen as test devices for microfluidics, and the complex percolation structures as model objects for real porous materials.

The acceleration mapping technique developed here allows the direct measurement of spatial acceleration distributions in simple and complex test objects. Experimentally recorded acceleration maps highlighted the tortuous pathway of the fluid in site-correlated percolation objects.

The correlated site-percolation models presented here try to mimic the high connectivity of the real porous materials, as they occur in nature. Well established NMR investigation protocols and CFD simulations permitted us to characterize the test objects only from the geometrical (percolation threshold, correlation length, fractal dimension) but also from the dynamic point of view.

Transport phenomena under combined action of pressure and electrical field gradients are of interest for many microfluidics applications. Electroosmotic flow patterns are strongly modified by hydrodynamic pressure gradients and ionic current density distributions built up in the pore system. The appearance of closed loops and vortices was detected. Electro-osmotic flow and current density mapping reveal dissimilarity in the Helmholtz/Smoluchovski equation for such complex systems. All NMR experiments mentioned above (velocity, acceleration, electro-osmosis and current density mapping) can be performed independently

of each other but in the same model object offering a broad range of information on the existing transport phenomena.

Contents

1 Introduction 2

2 Theoretical Background 3

2.1 Site-Percolation models 3

2.2 Pressure driven flow 5

2.3 Electroosmotic flow 6

3 Experimental and Computational Fluid Dynamics methods 8

3.1 Fabrication of test objects 8

3.2 Computational Fluid Dynamics (CFD) 8

3.3 Nuclear Magnetic Resonance Mapping 12

4 Results 15

4.1 Mapping of the higher orders of fluid motion – acceleration mapping 15

4.2 Ising-Correlated Percolation Models 17

4.3 Dissimilar behaviour of electro-osmotic flow and ionic current 21

5 Discussion and Conclusions 24

6 Literature 27

7 Zusammenfassung 29

8 Original papers for cumulative thesis 30

1 Introduction

Transport phenomena in microsystem devices are of general interest in many applied fields like protein separation in chromatographic analysis [1], mixing of fluids in narrow channels and capillaries [2] or efficient pumping of fluids at large flow rates in micron scale structures [3]. Other applications can be found extensively described in Ref. [4].

The cumulative thesis presented here deals with the investigation of transport phenomena of liquids and electrolytes under hydrodynamic pressure and electrical field gradients in different test objects. The test objects can be seen as microsystem devices as they are used in many microfluidics applications, where different transport phenomena act alone or in a combined way. For example, we have used a simple test structure composed of semicircles connected in series and parallel, to prove that higher order motions like acceleration, can be directly recorded [I]. On the other hand, simple structures often do not model complex systems like real porous materials. Therefore we chose site-percolation models as paradigms for porous materials. These sorts of systems are characterized by a good mathematical description and reproducibility. As method of investigation in such complex systems, we performed experiments based exclusively on Nuclear Magnetic Resonance (NMR) mapping techniques and, wherever possible, simulations consisting of Computational Fluid Dynamics (CFD) protocols.

The main research directions focus on 3 topics: developing new NMR techniques to access supplementary flow parameters (acceleration [I]), constructing and investigating Ising correlated structures as phantoms of real porous materials [II] and comparing combined electro-hydrodynamic phenomena (electroosmosis, current density, pressure driven flow) in polar and non-polar matrices [III], [IV].

Under hydrodynamic pressure gradients the distributions of the velocity and acceleration vectors in simple structures consisting of semicircles connected in series and parallel were recorded. A new NMR mapping technique was developed for recording such acceleration distribution maps. Once the technique was established to be reliable, the same procedures were applied in a site-percolation model highlighting especially the positions were the fluid is strongly accelerated or decelerated [I].

It was observed that natural porous materials sustain the transport of fluids even at very low porosities. Purely random site-percolation clusters cannot describe flow at such low porosities. That is why the Ising correlated percolation cluster mimic better the structure of real porous material, a result which was confirmed through CFD simulations and NMR experiments [II]. Such models could be of interest, for example, for modelling urban growth [5].

The combined electro-hydrodynamic phenomena with their similarities or dissimilarities are of particular interest in this thesis. Compared to flow under a pressure gradient, where the polarity of the surface plays no role, an electrolyte in contact with a polar surface will develop a net electro-osmotic flow (EOF) in the entire sample under the effect of an applied electrical field. Main questions arise in the case where the similitude between the applied electrical field and the resulting electro-osmotic flow is no longer obeyed as discussed in Ref. [6]. Such similitude problems were investigated in a 7 parallel channels structure in a closed configuration. The velocity distribution in a percolation cluster for such flows was investigated in comparison with other transport quantities like current density or pressure induced velocity. The recorded maps and the corresponding CFD simulations probed the similitude between fluid velocity and electric field. All three phenomena referred to, the electro-osmotic flow, the current density distribution and the pressure-induced flow were mapped separately in the same object by NMR mapping techniques [III], [IV]. This is a strong argument for such types of investigations in microsystem devices.

The theoretical background of the models and the phenomena presented here are detailed in Chapter 2. The NMR techniques and the CFD simulations are described in Chapter 3. Following the measuring and simulation protocols established and described previously, Chapter 4 presents intensively the results obtained in simple test structures and in more complex percolation clusters. Chapter 5 draws a set of conclusions and opens new problems and questions for further discussions and investigations.

2 Theoretical Background

2.1 Site-Percolation models

The percolation theory describes the behaviour of interconnected clusters randomly distributed in a given matrix. Percolation models have applications in physics, chemistry, and biology, where a random distribution of site occupation may describe physical, chemical or biological properties. Here we used the site-percolation model as paradigm for the structure of real porous materials with the clear advantage of a good mathematical description. The mathematical description of the percolation clusters allows a parallel investigation through CFD simulations and NMR experiments.

A site percolation cluster can be described as follows: consider a two-dimensional square lattice where each site can be either occupied randomly with a probability p or unoccupied with a probability $1-p$. Two situations can now occur. If the occupation probability still has a low value below a defined threshold value $p < p_c$, only isolated clusters appear inside the lattice composing the percolation model. If the occupation probability increases over the threshold value $p \geq p_c$, an "infinite" cluster appears connecting the two ends of the lattice (see Figure 1 left). We thus have a *sample spanning cluster*. A typical two-dimensional site percolation model based on a square lattice can be seen in Figure 1 (right). The isolated clusters shown in different colours (other than blue) have been eliminated from Figure 1 (left) since they do not participate to the transport phenomena of interest. The percolation threshold p_c, as parameter characterizing the site-percolation cluster, depends only on the type of the lattice (square in our case) and on the Euclidean dimension of the cluster (two for the discussed case). The dimension of the lattice was assumed to be infinite and the value of the percolation threshold is fixed at 0.592746 [7].

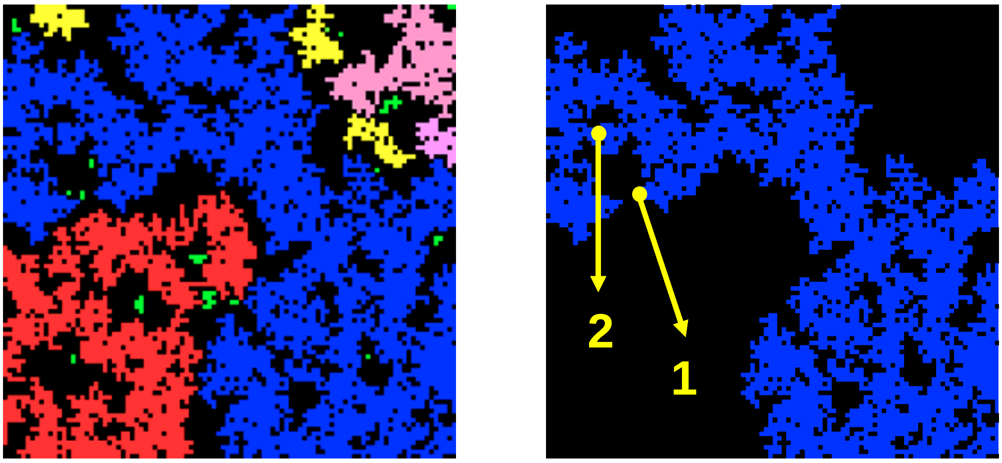

Figure 1. Example of a random two-dimensional site-percolation model with porosity $p = 0.6$ based on a square lattice with 100x100 sites. Black means "unoccupied" that is the matrix. Left: The entire site-percolation model with the composing clusters each render with a different identification colour. Right: The cluster marked in blue colour was extracted as representing the "infinite" percolating cluster and separated from the other non-percolating clusters. The area marked by the numbers 1 and 2 refer to plots in Figure 14.

Together with other key parameters, the site-percolation model can be completely described. The porosity p defined as the ratio between the occupied and the total number of sites, makes the connection with the real porous materials. The percolation probability P_∞ defines the condition for a site to belong to the "infinite" cluster. The correlation length ξ is the characteristic length in the percolation describing the mean distances between two sites of the same finite cluster at $p < p_c$. Near p_c, on length scales smaller than the correlation length ξ, the "infinite" cluster is self-similar and can be described by the fractal dimension d_f, another important parameter present in the description of the dynamic on the percolation clusters. Above the percolation threshold p_c, the "infinite" cluster can be seen as a homogeneous system composed of many unit cells of ξ. Such percolation structures could be computer generated and used as computational domain for simulations [8] or as specimen for manufacturing real samples for NMR experiments [9].

2.2 Pressure driven flow

The motion of an incompressible viscous fluid under laminar conditions and negligible gravitational forces is governed by the set of Navier-Stokes equations:

$$\begin{aligned}&\rho\frac{\partial\vec{v}}{\partial t}+\rho(\vec{v}\cdot\nabla)\vec{v}=-\nabla p+\eta\nabla^2\vec{v}+\vec{F}\\&\nabla\cdot\vec{v}=0\end{aligned} \tag{1}$$

where ρ represents the mass density and η is the dynamic viscosity of the fluid. The flow velocity field is represented by $\vec{v}=\vec{v}(\vec{r})$, the pressure is designated by p and $\vec{F}$ represent the so-called body force [10], [11]. The convective term $(\vec{v}\cdot\nabla)\vec{v}$ can be rewritten as

$$(\vec{v}\cdot\nabla)\vec{v}=\begin{pmatrix}v_x\,\partial v_x/\partial x+v_y\,\partial v_x/\partial y\\v_x\,\partial v_y/\partial x+v_y\,\partial v_y/\partial y\end{pmatrix} \tag{2}$$

corresponding to an Eulerian description of the fluid motion.

Under steady-state conditions, all explicit time dependences vanish, i.e. $\partial v_x/\partial t=\partial v_y/\partial t=0$, and using the Eulerian description from equation (2) the acceleration field $\vec{a}=\vec{a}(\vec{r})$ can be written component-wise for a two-dimensional case as

$$a_x=\frac{\partial v_x}{\partial x}v_x+\frac{\partial v_x}{\partial y}v_y \tag{3}$$

$$a_y = \frac{\partial v_y}{\partial x} v_x + \frac{\partial v_y}{\partial y} v_y \tag{4}$$

This formulation was used in the simulation procedure from Ref. [I], where the subject of investigation was the distribution of acceleration vectors in a simple test structure as well as in a correlated site-percolation model.

2.3 Electroosmotic flow

When an electrolyte solution comes in contact with a polar surface (e.g. ceramics), it becomes charged due to dissociation of polar groups of the material [12], [13]. The surface charges are compensated by the surplus counterions in the solution and an “electrical double layer” (EDL) is formed at the surface in conditions of thermal equilibrium. This net charge density decays from the highest value in the immobile “compact layer” directly at the surface down to zero across the mobile “diffuse layer”. This situation is represented schematically in Figure 2 for a two-dimensional channel.

The electrostatic potential due to the electric double layer, Φ_{EDL}, obeys the Poisson equation,

$$\nabla^2 \Phi_{EDL} = -\frac{1}{\varepsilon_0 \varepsilon} \rho_q, \tag{5}$$

where ε is the dielectric constant of the electrolyte solution, and ε_0 is the electric field constant. The charge density, ρ_q, is distributed in the electrostatic potential according to a Boltzmann factor,

$$\rho_q = e \sum_i c_{i0} z_i \exp\left\{ -\frac{z_i e \Phi_{EDL}}{k_B T} \right\}, \tag{6}$$

where e is the positive elementary charge, c_{i0} and z_i are the bulk concentration and the valence of the *i*-th ionic species, respectively, k_B is Boltzmann’s constant, and T is the absolute temperature.

In the high-temperature approximation, that is $\left| z_i e \Phi_{EDL} \right| << k_B T$, the right-hand side of Eq. (6) can be approximated linearly. That is the Debye/Hückel approximation valid for $\Phi_{EDL} < 25\ \mathrm{mV}$. The boundary condition for Eq. (5) is given by the ς potential on the surface and zero at infinity [12], [13]. The Debye/Hückel parameter is defined by

$$k^2 = \frac{2z_i^2 e^2 n_{i,\infty}}{\varepsilon\varepsilon_0 k_b T}, \tag{7}$$

where $n_{i,\infty}$ is the bulk concentration of the ion species *i*. The Debye/Hückel parameter describes the width of the electrical double layer and is in the order of $1/k$.

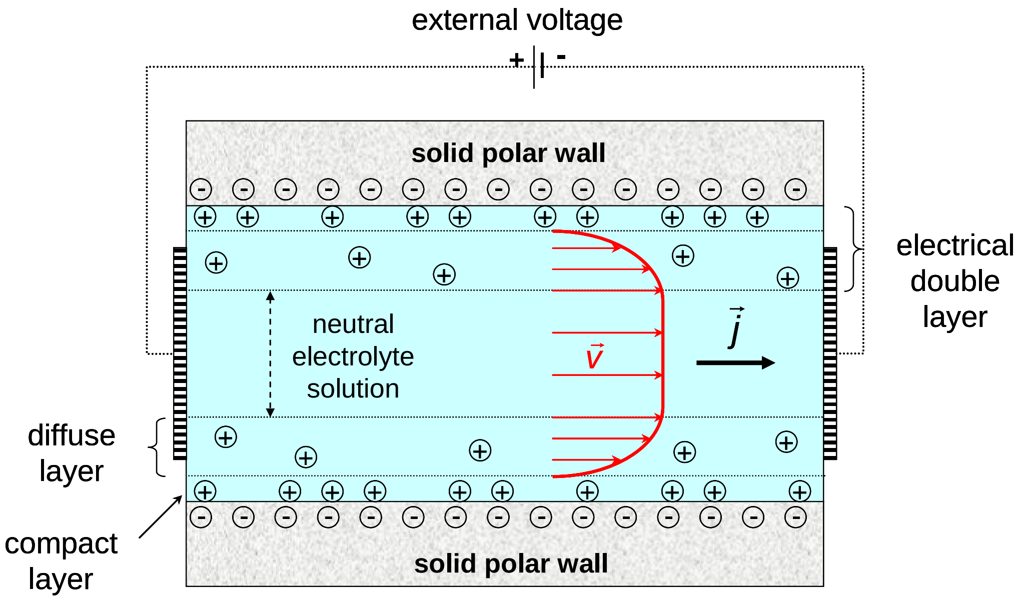

Figure 2. Schematic illustration of the electroosmotic phenomenon in a two dimensional tube

Applying an external electrical field, $\vec{E}_{ext}$, the mobile surplus counterions in the diffuse layer are driven towards the co-electrode. That is, viscous friction between the surplus counterions and the solvent causes shear flow in the diffuse layer whereas the electrically neutral solution in the middle of the channel is characterized by a flat velocity profile (Ref. [14], [15]) as can be seen in Figure 2.

The flow velocity field $\vec{v} = \vec{v}(\vec{r})$ can be described by the Navier/Stokes equation assuming incompressible fluids and negligible gravitational forces. Under steady state conditions, this equation reads for external electrostatic forces

$$\rho\left(\vec{v}\cdot\vec{\nabla}\right)\vec{v} + \vec{\nabla}p - \eta\nabla^2\vec{v} = \rho_q\vec{E}_{ext}, \tag{8}$$

while $\vec{\nabla}\cdot\vec{v} = 0$. The pressure in the fluid is designated by p. The quantities ρ and ρ_{q} are the mass and charge densities, respectively, η is the dynamic viscosity of the fluid, and $\vec{E}_{ext}$ is the external electrical field strength. At the walls the implicit “no-slip” boundary condition should be valid, i.e. $v_{wall} = 0$. The mean EOF velocity is predicted to be

$$\langle v_{EOF}\rangle \approx \frac{\varepsilon}{\eta}\varsigma E_{ext}. \tag{9}$$

NMR experiments revealing the characteristic EOF flat velocity profile have been published in Ref. [15], [16], [17] but no such experiments have been reported for more complicated structures like in the present study.

3 Experimental and Computational Fluid Dynamics methods

3.1 Fabrication of test objects

All the test objects used in the NMR experiments were fabricated with the aid of a computer controlled micro-milling plotter LPKF VC 101/F (“Leiterplatten Konturfräsen”). The computer generated structures were fed in polystyrene plates (BASF GmbH [18]) with non-polar characteristics or in ceramic materials (MACOR, Schröder Spezialglastechnik [19]). The ceramic materials were able to develop an electrical double layer in contact with an electrolyte solution exhibiting polar properties. The milling depth was around 2 mm in the case of polystyrene and 1 mm in the case of ceramic structures, respectively. For sensitivity reasons up to 10 identical but independently micro-milled plates were stacked together at a time. This configuration ensured also the quasi two-dimensionality of the studied objects. The complete fabrication process can be found in Ref. [I], [II], and [IV]. A typical photograph of such micro-machined structures can be seen for example in Ref. [I] Fig.3B.

3.2 Computational Fluid Dynamics (CFD)

A large number of applications from numerical simulation methods are concerning fluid dynamics under different physical conditions in different geometries. This particular area of numerical simulation is known under the general name of **C**omputational **F**luid **D**ynamics (CFD). The main idea of CFD is that starting from a real physical description of flow fields and continuing with the adoption and implementation of proper discrete numerical models, we can predict accurately, the flow fields. The CFD algorithms differentiate between them by the method used to approximate the physical equations which form the basis of the flow phenomenon. These are the finite differences method (FDM), the finite element method (FEM) and the finite volume method (FVM). As an example, a typical two dimensional flow field under pressure gradient can be seen in a contour representation in Figure 3. More details about all the mentioned models can be found in Refs.[17], [21].

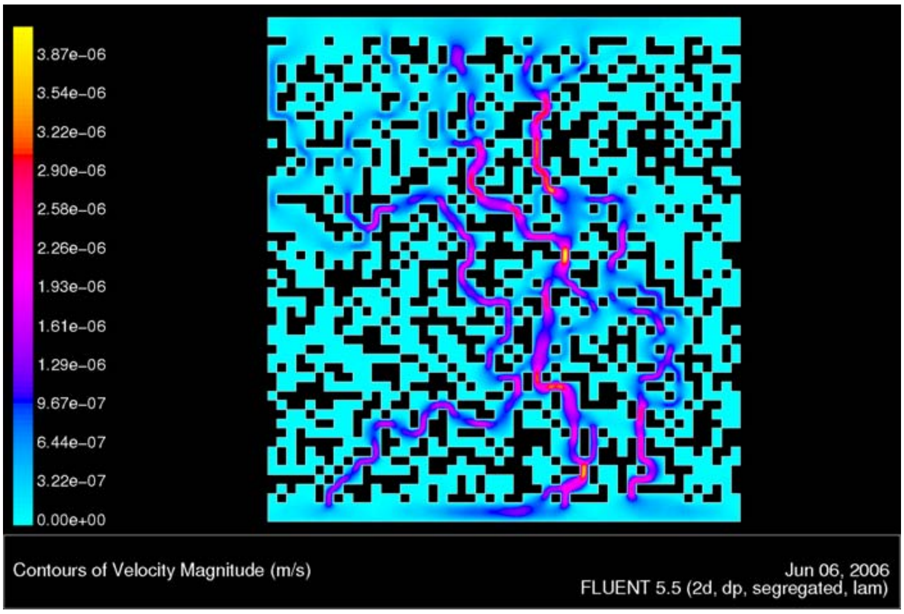

Figure 3. Contours of velocity magnitude in a two dimensional percolation cluster obtained through CFD simulations based on a Finite Volume Method.

All the flow and current density maps of the presented thesis were simulated for the (two-dimensional) geometries of the test objects with the aid of algorithms described in Refs [22], [23]. All simulations were based on two-dimensional computational grids. Three-dimensional treatments were avoided because of the limited computer capacity.

Two different commercial computational fluid dynamics programs were employed depending on the best adaptation to the problem to be solved. The first one, FEMLAB Ref. [24], based on the finite element method (FEM) is suitable for solving electro-osmotic flow and current density distributions. Simulations using this software were based on a network of triangular meshes with typically 65156 elements implying 452715 degrees of freedom.

The material parameters needed for the simulations were taken from the literature [13], [25]. The value of the dielectric permittivity was set $\varepsilon_w = 7.127 \times 10^{-10}$, the value of the zeta potential $\zeta = -100 mV$.

The electro-osmotic flow calculations were simplified by the fact that the Debye/Hückel approximation was valid and that the electric double layer couldn’t be resolved in the experiments, and hence need not be resolved in the simulations either. Corresponding boundary conditions at the walls were assumed to take this simplification into account.

Formally, the Navier/Stokes equations can be written without external force, as

$$\begin{aligned}&\rho_m\left(\vec{v}\cdot\vec{\nabla}\right)\vec{v}+\vec{\nabla}p-\eta\nabla^2\vec{v}=0,\\&\vec{\nabla}\cdot\vec{v}=0,\end{aligned}\tag{10}$$

by modifying the boundary condition according to

$$v_{wall}=-\frac{\varepsilon_w\varsigma_0}{\eta}E_{ext}\tag{11}$$

instead of the "no-slip" form mentioned earlier. ε_w is the value of the dielectric permittivity at the walls, and ζ_0 represents the zeta potential. At the surfaces of the electrodes, a "no slip" boundary condition, $v_{electrodes}=0$, was anticipated for "closed systems" without in- and outflow. This is in contrast to "open systems" where unrestricted flow across the electrode boundaries was assumed. A typical example of simulated electroosmotic velocity map can be seen in Figure 4a.

The electrical potential in an ionic solution without current sources and externally generated currents obeys the continuity equation for the current density, $\vec{j}$

$$\vec{\nabla}\cdot\vec{j}=\vec{\nabla}\cdot\left(-\sigma\vec{\nabla}\Phi\right)=0.\tag{12}$$

The boundary conditions are given by

$$\begin{aligned}&\Phi_{wall}=\infty \quad (\hat{=}\,\text{insulation}),\\&\Phi_{electrodes}=\Phi_0.\end{aligned}\tag{13}$$

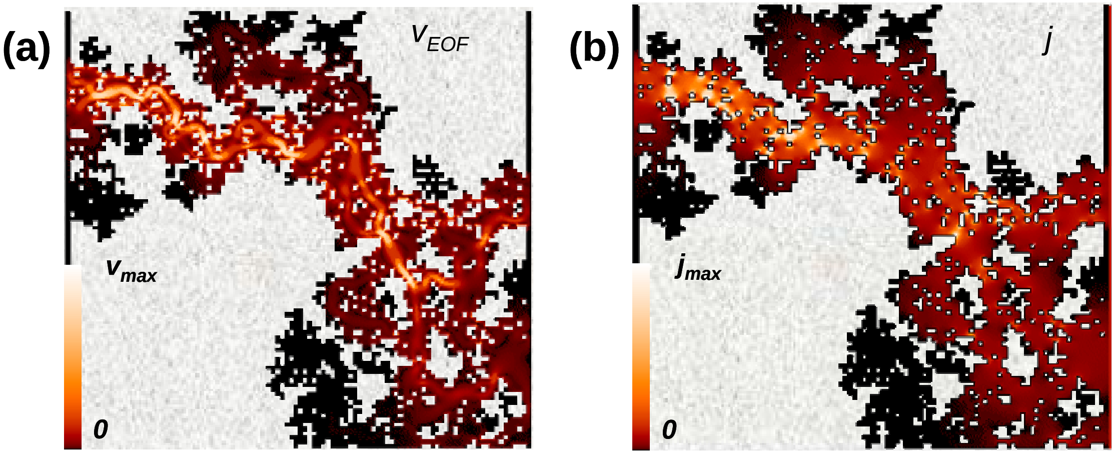

Figure 4. Typical simulated maps of the magnitudes of different transport parameters in the two-dimensional percolation cluster shown in Figure 1 (left). The matrix is rendered in gray and has the properties of the polar-matrix (MACOR). (a) Electro-osmotic velocity in a closed configuration (impermeable electrodes), v_{EOF}. (b) Electric current density, j.

Any effects due to chemical reactions at the walls and electrodes were neglected. Figure 4b shows a common simulated current density map based on the described algorithm.

Using computer simulations, various scenarios that are difficult to realize experimentally can be examined. In this sense, electro-osmotic velocity maps were investigated for open (permeable) electrodes in addition to maps for closed (impermeable) ones.

The second commercial software, FLUENT [26], based on the finite volume method (FVM) is appropriate for solving hydrodynamic flows generated by pressure gradients (see for example Figure 3). Nonetheless, an improvement through a third part program IDL (Interactive Data Language) Ref. [27] had to be specially made for solving the acceleration flow fields. In this case, the number of triangular mesh elements was typically 87080.

The simulation of the velocity fields is a simple task, assuming a two dimensional model and the flow in the steady-state laminar regime. Solving the Navier-Stokes equations (1) with the following set of boundary conditions

$$\begin{aligned} &v_{wall} = 0, \text{ no-slip wall treatment} \\ &v_{inlet} = v_0, \text{ inflow} \\ &p_{outlet} = p_0, \text{ outflow} \end{aligned} \tag{14}$$

we obtain the velocity flow field.

The simulation of the acceleration fields, as previously mentioned, requires the combined use of two commercial software packages, Fluent and IDL. The algorithm is based on the equations set (3) again for a steady-state flow. The derivatives $\frac{\partial v_x}{\partial x}, \frac{\partial v_x}{\partial y}, \frac{\partial v_y}{\partial y}, \frac{\partial v_y}{\partial x}$ in relations (3) and(4), are provided by the FLUENT package. The boundary conditions are similar to that of equation (14). For further processing, the IDL software was employed resulting in the desired acceleration component fields. The magnitude is then obtained from

$$a = \sqrt{a_x^2 + a_y^2} \tag{15}$$

Note that the acceleration components given in Eqs (3) and (4) depend on the (voxel) position but not on time since all velocity components are assumed to be locally stationary and merely change from position to position. Typical maps obtained in this way can be seen in Figure 7 and Figure 8.

3.3 Nuclear Magnetic Resonance Mapping

Nuclear Magnetic Resonance imaging, also referred to as Nuclear Magnetic Resonance Microscopy encompasses a great number of techniques and applications. The ability to provide in a non-invasive manner spatially resolved data sets of well-defined quantities make it of general interest for experimentally recording maps of physical parameters like spin density, velocity, acceleration, ionic current density, electro-osmosis, diffusion or thermal convection. In such context we speak therefore of Nuclear Magnetic Resonance Mapping techniques. A complete description of all mentioned techniques can be found in the monographs Ref. [28], [9] and [29].

Spin density maps emerging from an *x/z* fluid slice of the object (e.g. a percolation cluster as that in Figure 1), $\rho(x, y)$ can be obtained with the pulse scheme presented in Figure 5.

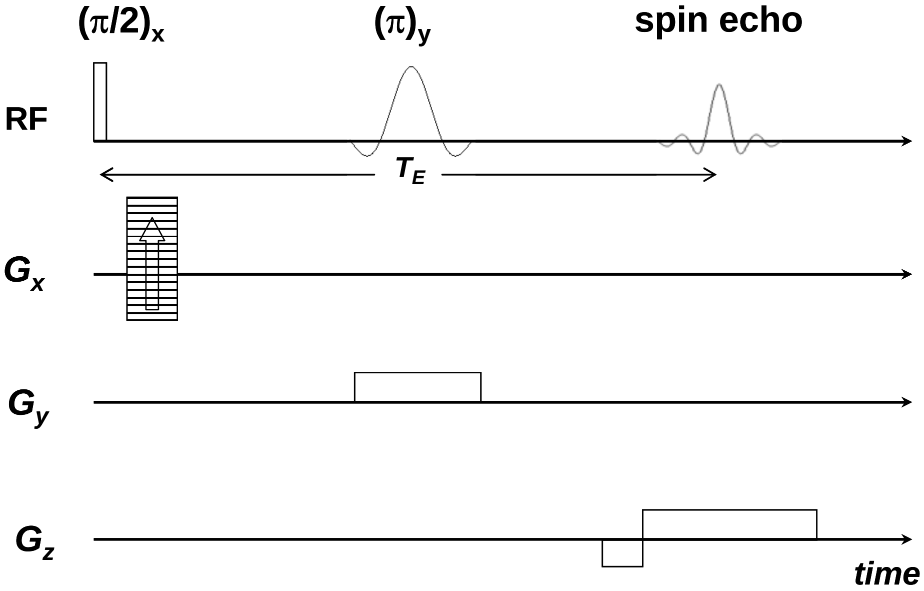

Figure 5. RF and field gradient pulse scheme for two-dimensional Fourier transform (2DFT) NMR imaging. A standard Hahn RF pulse sequence generates the spin echo signal with the characteristic echo time T_E. A “phase encoding gradient” is applied in the first RF pulse interval and is incremented in a series of subsequent transients. The second RF pulse is shaped and applied in the presence of a “slice selection gradient”. The spin echo is recorded in the presence of a “frequency encoding gradient”.

The Hahn echo signal refers only to the fluid, whereas the solid matrix does not contribute. The two spatial coordinates *x, z* are in phase and frequency encoded, respectively. The spin density map is then only the result of a two-dimensional Fourier transform analysis on the echo signal. The spatial resolution achieved with this pulse sequence and the given hardware configuration was better than 300 μm so that all details of the models used in this study could be accurately recorded.

Velocity and acceleration mapping technique is based on the modified version of the pulse sequence presented in Figure 5 by adding more gradient pulses as can be seen in Figure 6A and B. The additional gradients are necessary for encoding the desired information to be rendered. In the case of the velocity, the additional phase shift in the echo signal comes from two symmetrically (placed with respect to π-pulse) phase encoding gradients, $G_{x,y}$. The data set obtained represents actually a four-dimensional experiment, with two spatial coordinates (x, z) and two velocities (v_x, v_z). More details can be found in the Ref. [28], [9], [29], [I].

To acquire a *map of the electro-osmotic velocity,* the mapping of the velocity must be synchronised with a current pulse as shown in Figure 6C. Then, the entire necessary pulse sequence is composed of Figure 5, Figure 6A and Figure 6C, respectively. The only condition which must be properly taken into consideration is the length of the current pulse. It has to be long enough to achieve a steady-state condition before the velocity mapping experiment begins. A characteristic time to reach steady state in porous materials can be estimated based on the mean pore size of the system. Details can be found in Ref. [13], page 129. After steady-state electro-osmotic flow has been established, the procedure is similar to that of flow induced by pressure gradients.

Ionic current density maps can be recorded with the aid of the pulse sequence shown in Figure 5, plus the ionic current pulses from Figure 6D. The principle is based on Maxwell's fourth equation for stationary electromagnetic fields,

$$\vec{j}\left(\vec{r}\right)=\frac{1}{\mu_0}\vec{\nabla}\times\vec{B}\left(\vec{r}\right), \tag{16}$$

where $\vec{j}(\vec{r})$ is the electric current density at position $\vec{r}$, $\vec{B}\left(\vec{r}\right)$ is the magnetic flux density, and μ_0 is the magnetic field constant. The equation (16), in Cartesian components reads

$$j_x=\frac{1}{\mu_0}\left(\frac{\partial B_z}{\partial y}-\frac{\partial B_y}{\partial z}\right), j_y=\frac{1}{\mu_0}\left(\frac{\partial B_x}{\partial z}-\frac{\partial B_z}{\partial x}\right), j_z=\frac{1}{\mu_0}\left(\frac{\partial B_y}{\partial x}-\frac{\partial B_x}{\partial y}\right). \tag{17}$$

If we restrict ourselves to a quasi two-dimensional current distribution, invariant along the z-direction, we have $j_z=0,\ \partial B_y/\partial z=0$ and $\partial B_x/\partial z=0$.

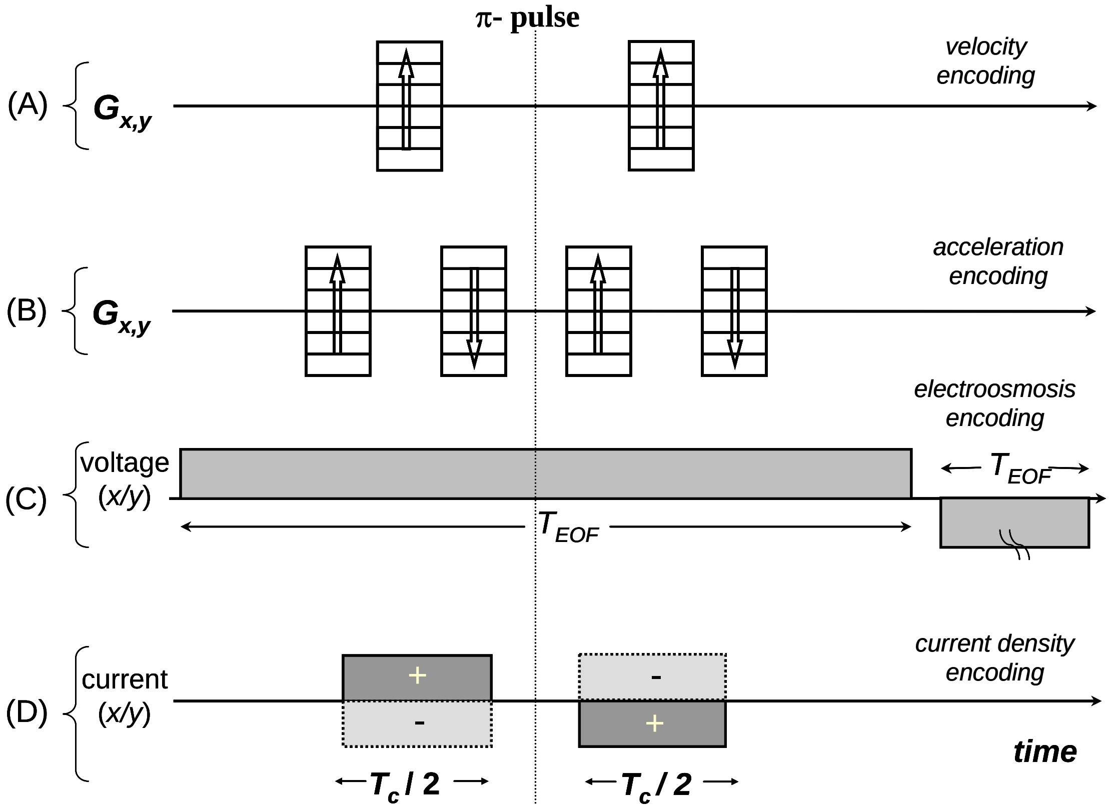

Figure 6. *Velocity mapping* (A): Maps of the velocity induced by pressure gradients can be recorded combining this gradient pulse sequence with that from Figure 5. The arrows indicate the direction in which the pulse gradients are incremented in subsequent transients. That is, two three-dimensional data sets are acquired for each component of the velocity $v_x(x, y)$ and $v_y(x, y)$. *Acceleration mapping* (B): Gradient pulse train composed of four gradient pulses that again in combination with pulse sequence from Figure 5 allows for acquiring the acceleration flow field map by its components $a_x(x, y)$ and $a_y(x, y)$. All other influences (spin density, velocity field) are reduced to zero due to the arrangement of the pulse train. *Mapping of the EOF* (C): The two voltage pulses combined with the pulse sequences from Figure 5 and the gradient pulse sequence (A) allows for recording the electro-osmotic velocity map, $v_{EOF}(x, y)$. The length of the pulse is marked by T_E. The second voltage pulse is used to protect the electrodes by reversing the electrolytic effects. *Mapping of the current density* (D): In samples invariant along the *z*-axis, two-dimensional current density maps of the *x/y* plane, $j(x, y)$, can be recorded based on the phase shifts produced by sequence (D) [30]. T_C is the total application time of ionic currents. Note that, in contrast to the EOF pulse scheme from (C), the phase shifts induced by the current pulses before and after the π-pulse do not cancel each other out owing to the polarity. The polarity is alternated in subsequent experiments while subtracting the current densities from each other according to $j_{x,y} = \left(j_{x,y\pm} - j_{x,y\mp} \right) / 2$. In this way, undesired offsets are eliminated. Note that all these maps can be recorded in the same object just by choosing the appropriate combination of pulse sequences.

Now, the only finite components are

$$j_x(\vec{r}) = \frac{1}{\mu_0}\left(\frac{\partial B_z(\vec{r})}{\partial y}\right), j_y(\vec{r}) = \frac{1}{\mu_0}\left(-\frac{\partial B_z(\vec{r})}{\partial x}\right) \tag{18}$$

The problem which we have to solve for this NMR mapping technique is to determine the two finite partial derivatives $\partial B_z/\partial x$ and $\partial B_z/\partial y$. Detailed descriptions of the method can be found in Refs [30], [31]. The values of the derivatives can be obtained by evaluating the local precession shifts caused by the current pulses, where T_C is the total evolution time (see Figure 6D). Deriving numerically such phase shifts one obtains the desired local derivatives of the current induced magnetic flux density. Another problem is that the maps of the precession phase shifts due to the local current density are “wrapped”. An “unwrapping” algorithm must be used. Goldstein’s two-dimensional unwrapping algorithm turned out to provide reliable results [32].

4 Results

4.1 Mapping of the higher orders of fluid motion – acceleration mapping

A comparison between the experimental and simulated acceleration component maps can be seen in Figure 7. As test object for validating the simulated and experimental protocols a combination of arc circles with varying radius connected in series and parallel was used. The complete description of the test object used in this experiment can be found in Ref. [I], Fig. 3A. The mean radial acceleration depends on the circle arc radius as

$$a = \frac{v^2}{r} \tag{19}$$

which in the context of constant mean velocity becomes $a \sim 1/r$. This theoretical prediction was reproduced with reasonable accuracy in the experiment (see Figure 7d) validating not only qualitatively but also quantitatively our investigation methods for accelerated fluid motion.

In Figure 8, maps of the mean acceleration and mean velocity in a random site percolation cluster are shown both for experimental and simulated data. The complete description of the percolation cluster used in the experiment is given in Ref. [I], Fig. 3B.

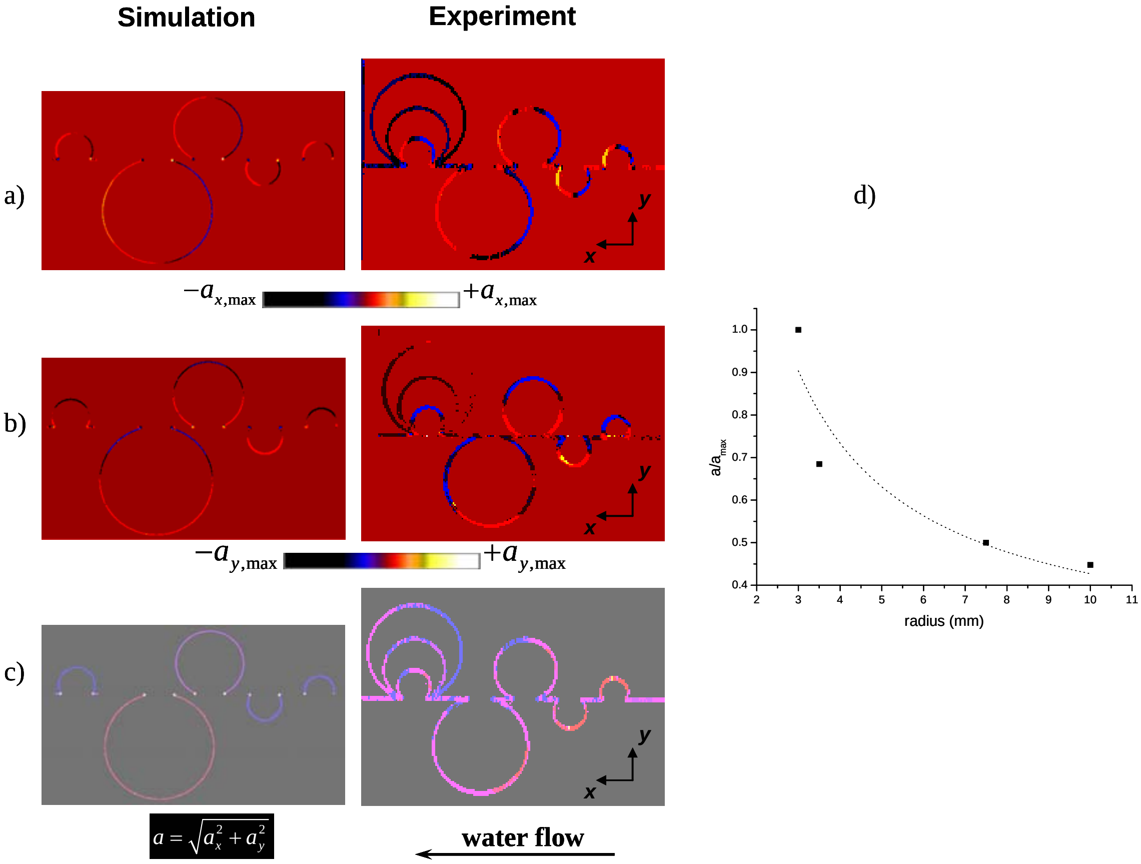

Figure 7. Maps of the x component (a), y component (b), and the magnitude (c) of the mean acceleration for a test structure composed of arc circles of various radii connected in series or parallel. Details of the test structure are provided in Ref. [I], Fig. 3A. (d) Mean radial acceleration as a function of the circle arc radius in the test object. The black rectangles represent experimental data, and the dotted line was fitted according to Eq. (19).

The simulation technique was presented in section 3.1. The experimental method is based on a phase encoding sequence based on bipolar gradients. It was already explained in detail in section 3.3. In the case of acceleration and velocity the experimental flow patterns are well reproduced in the simulations. Anyway there are significant changes between the accelerated motion and the stationary flow velocity. The velocity map shows a more continuous character in contrast with the acceleration map where strong fluctuations can be identified along the main flow path. That is, the magnitude of the acceleration vectors is above the experimental noise level only in certain voxels. This indicates the spots where the fluid is strongly accelerated or decelerated.

In the Appendix of Ref. [I] a new method, “polygon rule”, was introduced as general rule to design simple gradient pulse sequences necessary for encoding of any type of motion under gradient pressure, e.g. velocity or acceleration. As we have already shown, the "polygon rule" can be successfully applied to acceleration mapping.

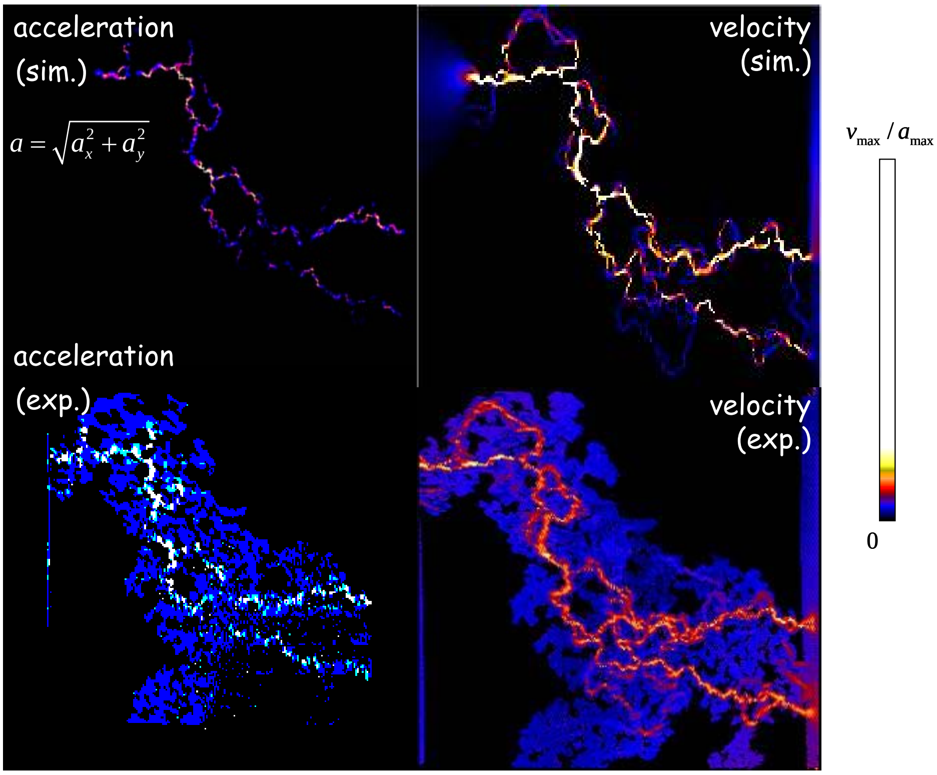

Figure 8. Experimental and simulated maps of the mean acceleration magnitude $a=\sqrt{a_x^2+a_y^2}$ (left column) and the mean velocity magnitude $v=\sqrt{v_x^2+v_y^2}$ in a site percolation cluster $(p=0.6, p-p_c=0.02)$. The model object can be seen in Ref. [I], Fig. 3(B).

4.2 Ising-Correlated Percolation Models

In contrast with the purely random site-percolation model, the Ising-correlated model mimics the growth history of natural porous materials as presented in Refs. [33], [34]. Based on a characteristic parameter, the correlation factor $f_c = w_{growth}/w_{nucl}$ (defined as the quotient between the nucleation probability w_{nucl} and the growth probability w_{growth} relative to the occupation of the neighbouring sites) a computer algorithm was developed for a two dimensional lattice. This can be seen in detail in Ref. [II], Fig. 1. The results can be seen in Figure 9 where there is a strong difference between an uncorrelated site-percolation model ($f_c=1$, left) and a strongly correlated one ($f_c=10\,000$, right).

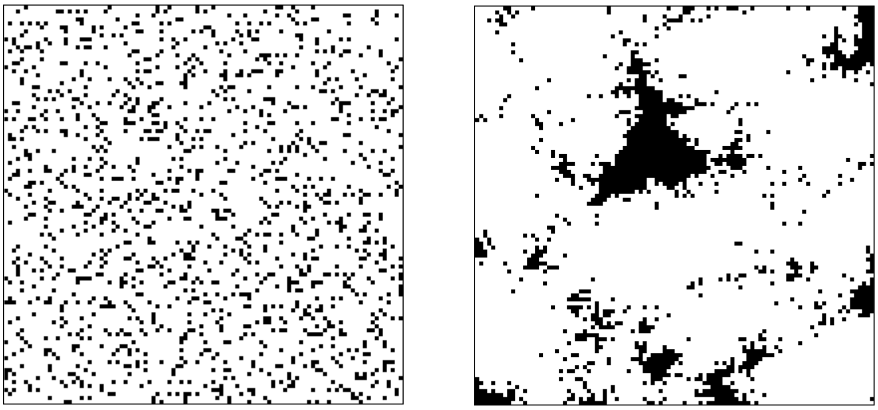

f_c = 1; p_{final}=0.864 f_c = 10,000; p_{final}=0.864

Figure 9. Comparison between an Ising-correlated cluster with high (right) growth-nucleation rate and a random site-percolation cluster (left). “Black” represents the matrix which is “unoccupied”. White pixels represent the pores in a base lattice size of 100x100 sites.

The examination of Ising-correlated percolation clusters was done for more than $12\,000$ possible configurations varying a set of parameters like the dimension of the square base lattice $(L = 50,\ 100,\ 200,\ 500)$ or the growth-nucleation quotient $(3.2 \geq f_c \geq 32\,000)$. The results were summarized in section 2.1 from Ref. [II]. As a result we can identify in Figure 10 that a minimum is reached for the percolation threshold in the interval $3.2 < f_c < 320$.

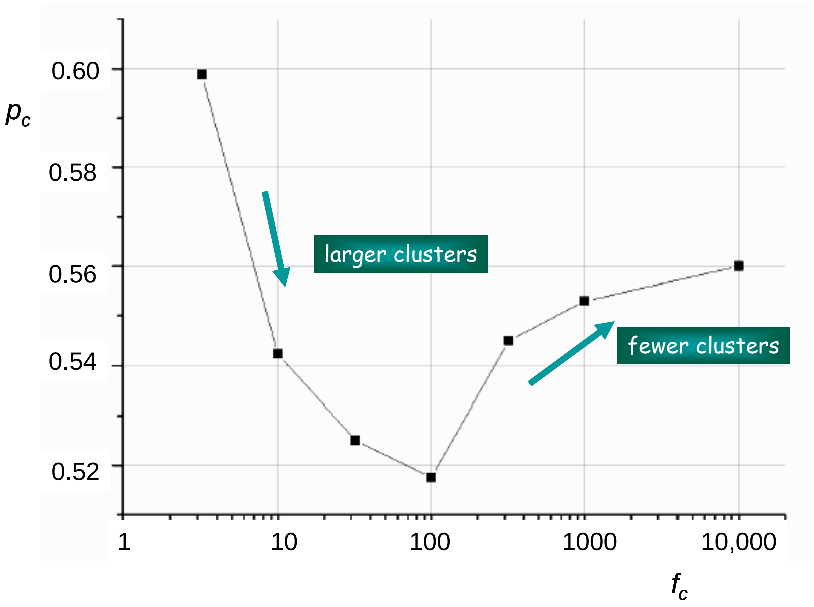

Figure 10. Percolation threshold p_c for the Ising-correlated site percolation model as a function of the growth-nucleation ratio f_c. The base lattice was $L \times L = 200 \times 200$ sites. A minimum is reached in the interval $30 < f_c < 320$

The minimum arises at the percolation threshold between 0.51 and 0.52 independent of the base matrix size.

This is in accordance with the fact that natural materials even at very low porosities, sustain transport features as depicted in Ref. [34].

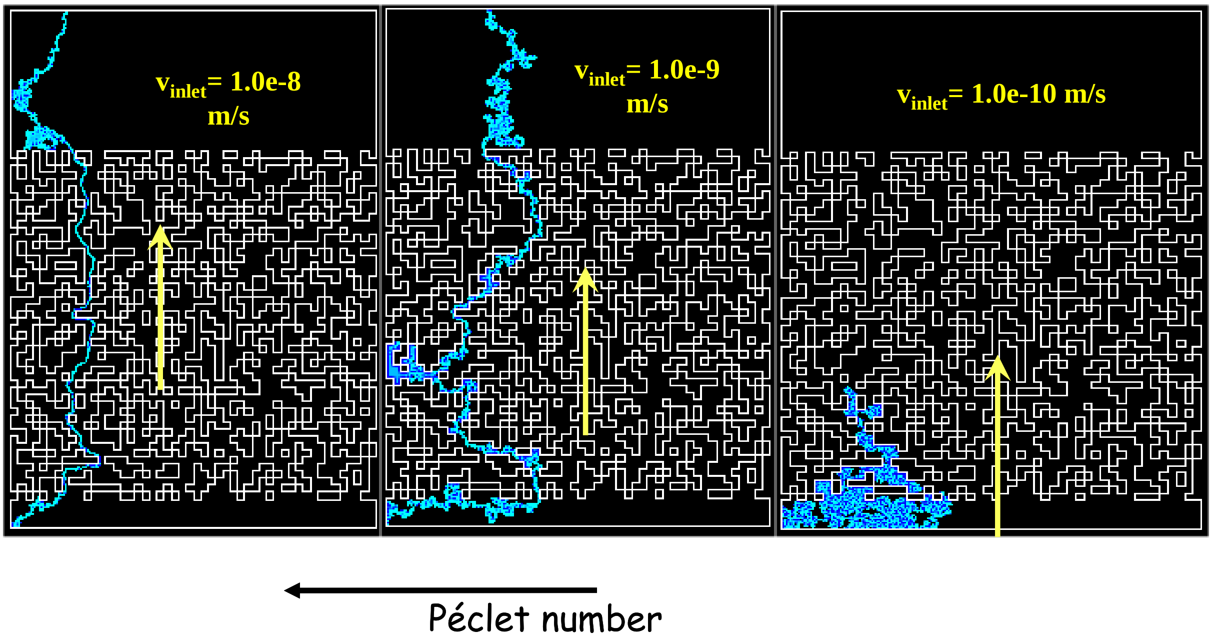

Figure 11. Hydrodynamic dispersion of a neutral tracer in a flow field percolating in an Ising-correlated site-percolation cluster.

Other characteristic parameters of the percolation, like the correlation length ξ or the fractal dimension d_f were investigated based on earlier established protocols (see Refs. [8], [33], [35]) and the results can be seen in greater detail in section 2.2 of Ref. [II].

Figure 11 shows typical trajectories of the hydrodynamic dispersion of a neutral tracer particle diffusing in a streaming fluid in three different Ising-correlated clusters. The dispersion of the tracer is influenced by the macroscopic Péclet number [34] defined by

$$Pe = \frac{vl}{D} \tag{20}$$

where v is the fluid velocity, D is the molecular diffusivity and l is the characteristic length of the flow field. l was identified in the case of the site-percolation with the correlation length ξ and Eq. (20) becomes $Pe = v\xi/D$.

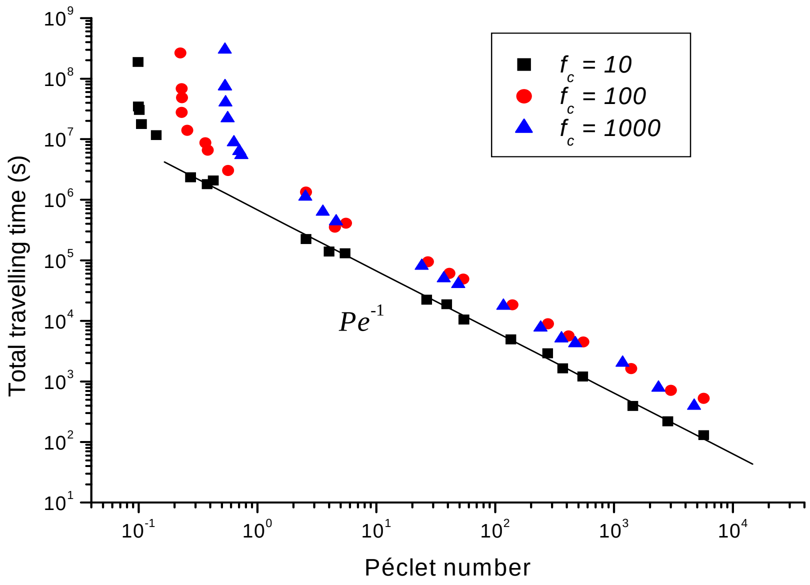

Figure 12. Total traveling time across the sample experienced by a neutral tracer as a function of the Péclet number for three different growth-nucleation factors. The data were evaluated from CFD simulations.

The quantitative evaluation of the simulated data can be seen in Figure 12 where the mean traveling time of the neutral tracer across the percolation cluster was plotted as a function of the Péclet number for various correlation factors $(f_c = 10,\ 100,\ 1000)$. The data can be easily described separately in two regions. In region I, above $Pe = 1$, the data can be approximated by the following relation:

$$\tau_t \propto (Pe)^{-1} \text{ for } 10^0 < Pe < 10^4 \tag{21}$$

where τ_t is the mean traveling time. This corresponds to the purely mechanical dispersion regime where coherent flow dominates the dispersion almost completely. Region II, below $Pe = 1$, corresponds to the isotropic dispersion case where the incoherent Brownian motion dominates the trajectory. More discussions about this matter can be found in Ref. [34].

The complete evaluation of all experimental and simulated results in the form of velocity, acceleration and neutral tracer maps are presented in section 6 of Ref. [II] as volume averaged porosity quantities, velocity histograms, mean tracer traveling time or spatial velocity autocorrelation functions.

4.3 Dissimilar behaviour of electro-osmotic flow and ionic current

Experimental maps of different transport quantities in a percolation cluster (see Figure 1 for details) are rendered in Figure 13.

For the electro-osmotic flow (Figure 13A1), the mean velocity $v_{EOF}\left(\vec{r}\right)$, can be related with the electrical field $\vec{E}_{ext}$ through the Helmholtz-Smoluchowski equation given in Eq. (9). The electro-osmotic flow map here refers to the case where the inflow and outflow electrodes were used in a closed configuration (no mass transport by in- and outflow was allowed). The counterpart, pressure driven flow maps $v_{PIF}\left(\vec{r}\right)$ are shown in Figure 13(D). For comparison with the third transport phenomenon, ionic current density $j\left(\vec{r}\right)$, we have to refer to two possible configurations: in the presence of a polar matrix (for example, MACOR), that is the electro-osmosis is present and the corresponding experimental map can be seen in Figure 13(B1) for $j_{EOF}\left(\vec{r}\right)$, or in the absence of electro-osmosis (non-polar matrix, e.g. polystyrene) as can be seen experimentally in Figure 13(C1) for $j\left(\vec{r}\right)$. Already, strong deviations between the hydrodynamic flow and current density maps can be identified. A detailed area enlarged for all the recorded maps shows surprising results as can be seen in Figure 13 (column B) as velocity vector field representation or in Figure 13 (column C) and Figure 14 in a streamline field representation.

In the presence of electro-osmosis, both the velocity and the current density maps show recirculation patterns (see Figure 14b and c) but remarkably at different positions in the cluster. At the position marked with 1 in Figure 1 (left), no flow vortex appears whereas the ionic current density clearly shows a recirculation pattern. Position 2, on the other side, gives contrary results: no ionic current density vortex but a clear electro-osmotic recirculation pattern. The absence of electro-osmosis phenomena tends to support the idea of no vortex occurrence in both cases: flow and ionic current density (see Figure 13C3 and D3).

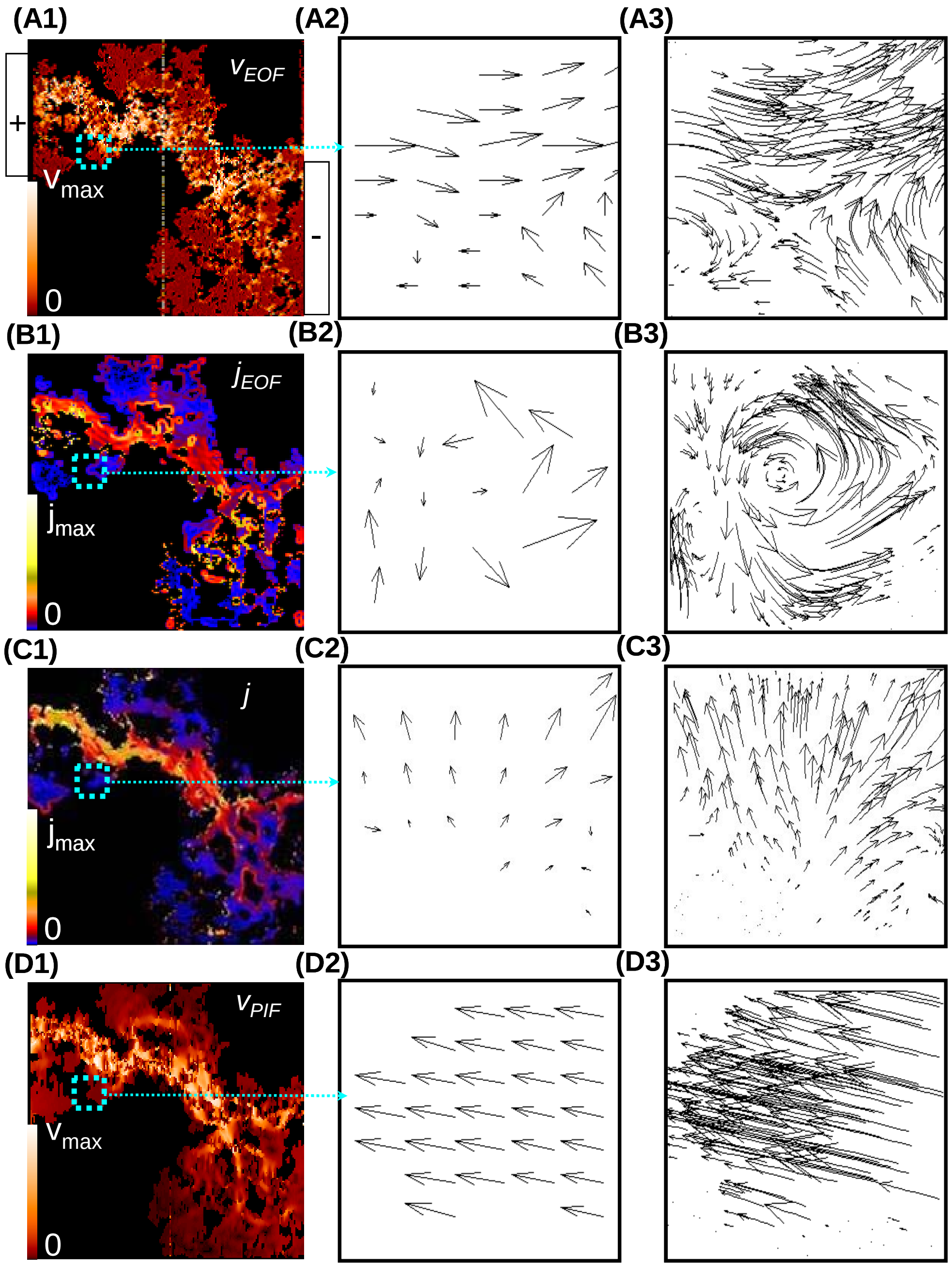

Figure 13. Left-hand column: Experimental maps of the magnitudes of different transport quantities measured in percolation objects in a 4x4 cm field of view (see Fig.1 left side). The matrix is rendered in black. (a) EOF velocity, v_{EOF} , at a mean electric field strength of 83 V/cm (polar matrix). The position of the (closed) electrodes is indicated. (b) Electric current density in the presence of EOF, j_{EOF} (polar matrix). (c) ECD in the absence of EOF, j (non-polar matrix). (d) Flow velocity caused by an external pressure gradient in the open system, v_{PIF} . Middle column: Enlarged area at position 1 marked in Fig. 1 in vector plot form. The size is 1.2 mm x 1.2 mm. Right hand-column: Same as before, but now in streamline representation. That is, the arrow vectors are curved along the local streamlines, and the length of the curvilinear vectors is proportional to the mean magnitude along the arrow. Typical maximum values for the velocity and electric current density are v_{max} = 4.5 mm/s and j_{max} = 5 mA/mm^2, respectively.

These detailed vector representations suggest a strong interference between flow and ionic current, never seen before in such systems. The differences between the hydrodynamic flow and ionic electric currents have been discussed in Ref. [36].

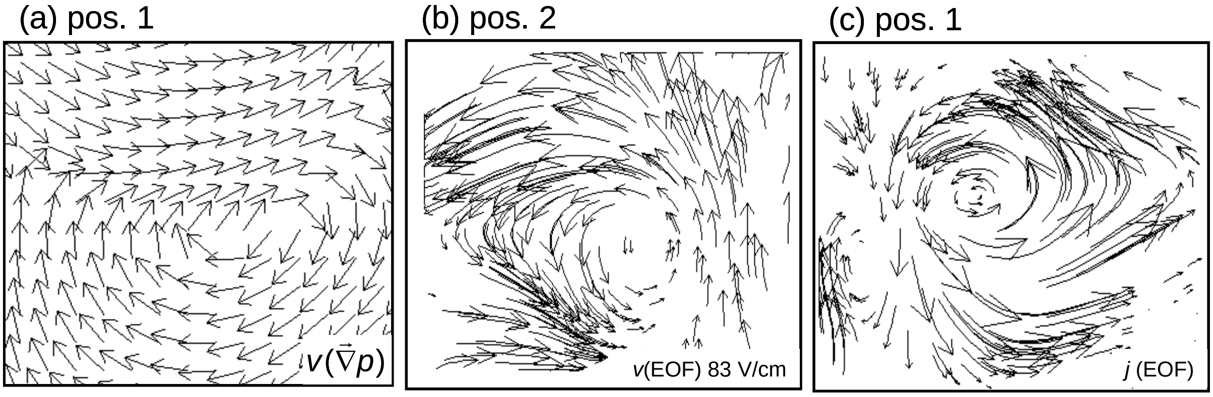

Figure 14. Vortices of different transport quantities at positions 1 or 2 (see Fig.1 left side). (a) Two-dimensional CFD simulation of the flow velocity driven by an external pressure gradient at position 1 (area 0.8 mm x 0.8 mm). (b) Experimental EOF velocity at position 2 (area 1.2 mm x 1.2 mm) in streamline representation. (c) Experimental ECD in the presence of EOF at position 1 (area 1.2 mm x 1.2 mm) in streamline representation.

The resistivity plays a stronger role in the pressure induced flow than in the case of ionic currents and was explained based on existing inertial effects. On the other hand, the electro-osmotic flow is a result of available charged surface area and the applied voltage. That is the electro-osmotic flow is expected to have a more homogeneous distribution inside such channel networks like percolation clusters than pressure induced flow. The fact that electric current density shows recirculation patterns is remarkable in the sense that it should obey the equation $\vec{\nabla} \times \vec{E} = 0$ for electrostatic fields. This behaviour contradicts the CFD simulations. This raises the question of similitude between the fluid velocity and electric field in the electro-osmotic flow as discussed in Ref. [6]. The Helmholtz-Smoluchowski equation is then not satisfied at the electrodes and therefore there is no longer a linear dependence between the flow velocity $v_{EOF}\left(\vec{r}\right)$ and the electrical field $\vec{E}$.

Recirculation patterns were also investigated in direct relation with the porosity p of the percolation cluster and details can be found in section 4.3 of Ref. [IV]. Practically, a sharp crossover from localized to sample spanning loops at the percolation threshold, p_c was verified. Recirculation patterns in closed systems (no permeable electrodes) could be used for designing cyclic systems like micro electro-osmotic pumps. Such results are shown in detail in section 4.1, Ref. [IV].

5 Discussion and Conclusions

NMR mapping together with CFD simulations is a unique combination of methods for the investigation of transport phenomena of different origins inside simple and complex geometries. In this work, this modus operandi provided us in non-invasive manner information about hydrodynamic flow inside percolation clusters in the form of velocity and acceleration maps. Information about electro-osmotic flow in ceramic-built samples of simple and complex nature and information about ionic current density distribution in the presence or absence of electro-osmosis can also be acquired. The main strength of the technique is that all the above mentioned parameters (velocity, acceleration, electro-osmotic velocity and current density) can be recorded independently of each other but in the same experimental object. For this reason a comparison between them is feasible and can be supplemented by CFD simulated data.

It was demonstrated that acceleration in flow through complex porous media can directly be mapped by an NMR technique in addition to conventional flow velocity mapping. Since all transport quantities recorded by NMR microscopy techniques refer to voxel averages, the *direct* measurement of spatial acceleration distributions is considered to be more reliable than the reconstruction based on the derivation of mean velocity maps. Acceleration maps specifically highlight bottlenecks and strongly curved pathways of flow. They are therefore considered to be indicative for corresponding topology elements of the pore space.

Combined experimental and computational studies of the structure and transport properties of Ising-correlated quasi two-dimensional percolation model objects were performed. Parameters such as the percolation threshold, the correlation length and the fractal dimension were found to deviate from the values corresponding to the uncorrelated case, the random site-percolation model [7], [8], [33]. Dependences on the Ising-correlation quotient and on the porosity were also examined.

The percolation threshold value is lower than in random site percolation networks and interestingly shows a minimum at a correlation factor $f_c \approx 100$ (see Figure 10). This is in accordance with findings reported in Refs [37] and [38] for other correlated percolation models. The explanation of the minimum of the percolation threshold is that with increasing correlation factor, the cluster size increases which favors transport across the network. However, there is an opposite tendency indicated by the fact that the number of clusters is reduced at the same time. At correlation factors below 100, the first tendency dominates whereas above that value the second trend starts to govern the dependence on the correlation factor.

As transport quantities, the magnitudes of the flow velocity and of the flow acceleration were examined both with magnetic resonance imaging experiments and with a computational fluid dynamics method. Furthermore, the hydrodynamic dispersion of a neutral tracer in the flow field was studied as a function of the Péclet number using again computer simulation tools. The two identified regimes correspond to an isotropic dispersion range, $Pe < 1$, where diffusion dominates, and to a mechanical dispersion interval, $1 < Pe < 10^4$, where flow controls dispersion almost completely [5], [34].

Ising-correlated percolation clusters are expected to mimic the structure of natural porous materials that were formed by growth processes of a similar nature. The main pore space feature that matters here is the larger pore connectivity resulting from the correlation assumed in the growth algorithm which generates the models. This is in contrast to random site-percolation networks which are known to be too “random” for the description of typical porous media. The correlations significantly diminish the percolation threshold as a result of the clustering of low and, on the other hand, high permeability regions. This is consistent with experimental observations that indicate a high permeability of many natural porous media even at very low porosities [34]. The Ising-correlated quasi two-dimensional percolation networks considered here were associated in the past with the growth dynamics of urban clusters. Corresponding analyses have been published in Refs. [5], [39].

The combined action of electro-osmosis and ionic current density in percolation clusters yielded interesting and unexpected results. It was shown that electro-osmotic flows as well as the electric current density include vortices and recirculation patterns. All transport pathways turned out to be dissimilar, and the occurrence and positions of vortices did not coincide in different maps. On this basis, conclusions with respect to the similitude of transport patterns are feasible. The differences between the experimental ionic current density maps of the percolation cluster recorded with and without EOF, i.e. in ceramic and polystyrene model objects, respectively, of the same geometry are remarkable. A clear interference between hydrodynamic flow and electric current can be observed. Eddies of the electric current density were observed in the presence of electro-osmosis, but not in the hydrodynamically static case. This may be considered as a combined hydro- and electrodynamic phenomenon. A particle driven by hydrodynamic flow through an inhomogeneous electrostatic field effectively experiences a time-dependent electric field strength, $\vec{E} = \vec{E}(t)$, despite stationary flow and electrostatic conditions. There is a certain analogy to the “material” acceleration $\vec{a} = (\vec{v} \cdot \vec{\nabla})\vec{v}$ known from the Navier/Stokes equation given in Eq. (2). That is, electrostatic laws are not applicable in the presence of electro-osmotic flow. Taking the electro-osmotic flow, ionic current density, and pressure induced flow experiments and simulations together, one can say that recirculation patterns occur with all transport quantities considered here, but at different positions of the percolation cluster.

This type of combined studies could be of interest for microsystem technology as presented in Refs. [40], [41]. Microsystem devices often consist of complex channel networks implying features of the model objects of the present study. Based on a structure producing closed-loop flow, cyclic electro-osmotic pumps without moving elements can be designed. The intentional production of recirculation in such systems is essential for the function of microsystem mixers as discussed in Ref. [42].

The combined application of NMR microscopy techniques for the quantitative, non-invasive visualization of the total variety of hydro- and electrodynamics in the same system can thus be considered as a promising design tool for microsystems superior to conventional fluid dynamics techniques such as particle image, ultrasound Doppler or laser Doppler velocimetry [11].

6 Literature

[1] Eijkel Jan C. T., Berg van den A., Manz A.: Electrophoresis **25**, 243 (2004)

[2] Chen H., Zhang Y. T., Mezic I., Meinhart C. D., Petzold L.: Proc. Microfluidics 2003, ASME IMECE (2003)

[3] Yao S., Huber D., Mikkelsen J. C., Santiago J. G.: Proc. of IMECE, Proc. of International Mechanical Engineering Congress 2001, ASME IMECE (2001)

[4] Lab on a chip, RSC Journals

[5] Makse H. A., Havlin S., Stanley H. E.: Nature **377**, 608 (1996).

[6] Cummings E. B., Griffiths S. K., Nilson R. H., Paul P. H.: Anal. Chem. **72**, 2526 (2000).

[7] Stauffer D., Aharony A.: Introduction to Percolation Theory, London: Taylor and Francis, 1992.

[8] Klemm A., Müller H. P., Kimmich R.: Phys. Rev. E **55**, 4413 (1997).

[9] Kossel E., Buhai B., Kimmich R. in Stapf S., Han S.-I.(Edts): NMR Imaging in Chemical Engineering, Chap. **2.9**, Weinheim: Wiley-VCH, 2005.

[10] Trittton D. J.: Physical Fluid Dynamics, New York: Oxford University Press, 1988.

[11] Guyon E., Hulin J.-P., Petit L., Mitescu C. D.: Physical hydrodynamics, New York : Oxford University Press, 2001.

[12] Probstein R. F.: Physicochemical Hydrodynamics, New York: Wiley, 1994.

[13] Li D.: Electrokinetics in Microfluidics, London: Elsevier, 2004.

[14] Zhu W., Singer S.J., Zheng Z., Conlisk A.T.: Phys. Rev. E **71**, 041501 (2005).

[15] Yao S., Santiago J.G.: J. Colloid & Interface Sci. **268**, 133 (2003).

[16] Wu D, Chen A., Johnson C. S. Jr.: J. Magn. Reson. A **115**, 123 (1995).

[17] Manz B., Stilbs P., Jönsson B., Södermann O., Calaghan P.T.: J. Phys. Chem. **99**, 11297 (1995).

[18] https://www.plasticsportal.net/wa/EU/Catalog/ePlastics/doc/BASF/prodline/polystyrol/

[19] http://www.schroederglas.com/download/MacorProduktbeschreibung

[20] Cuvelier C., Segal A., Steenhoven A. A.: Finite Element Methods and Navier-Stokes Equations, Dordrecht: D. Reidel Publishing Company, 1986.

[21] Griebel M, Dornseifer T., Nuenhoffer T.: Numerische Simulation in der Strömungslehre: eine praxisorientierte Einführung, Wiesbaden: Vieweg, 1995

[22] Patankar N. A., Hu H. H.: Anal. Chem. **70**, 1870 (1998).

[23] Alam J., Bowman J.C.: Theoret. Comput. Fluid Dynamics **16**, 133 (2002).

[24] FEMLAB: User’s Guide, Stockholm: Comsol AB, 2004.

[25] Morre J. H., Spencer D. N., Encyclopedia of Chemical Physics and Physical Chemistry, Volume I : Fundamentals, Bristol: IoP, 2001

[26] FLUENT: User’s Guide, Lebanon: Fluent Inc., 2000.

[27] IDL: User’s Guide, Boulder, Research System Inc., 1999.

[28] Kimmich R.: NMR Tomography, Diffusometry, Relaxometry, Berlin: Springer, 1997.

[29] Kimmich R.: Chem. Phys. **284,** 253 (2002).

[30] Scott G. C., Joy M. L. G., Armstrong R. L., Henkelman R. M.: J. Magn. Reson. **97**, 235 (1992).

[31] Sersa I., Jarh O., Demsar F.: J. Magn. Reson. Series A **111**, 93 (1994).

[32] Ghiglia D. C., Pritt M. D.: Two dimensional phase unwrapping, New York: Wiley, 1998.

[33] Bunde A., Havlin S.: Fractals in Science, Berlin: Springer, 1994.

[34] Sahimi M.: Flow and Transport in Porous Media and Fractured Rock, Weinheim: VCH, 1995.

[35] Müller H. P., Weis J., Kimmich R.: Phys. Rev. E **52**, 5195 (1995).

[36] Weber M., Kimmich R.: Phys. Rev. E **66**, 026306 (2002).

[37] Prakash S., Havlin S., Schwarz M., Stanley H. E.: Phys. Rev. A**46**, 1724 (1992).

[38] Blumberg R. L., Shilfer G., Stanley H. E.: J. Phys. A: Math. Gen. **13**, 147 (1980).

[39] Makse H. A., Andrade Jr. J. S., Batty M., Havlin S., Stanley H. E.: Phys. Rev. E**58**, 7054 (1998).

[40] Sinton D.: Microfluid Nanofluid **1**, 2 (2004)

[41] Takamura Y., Onoda H., Inokuchi H., Adachi S., Oki A., Horiike Y.: Electrophoresis **24**, 185 (2003).

[42] Chen H., Zhang Y.T., Mezic I., Meinhart C.D., Petzold L.: Proc. Microfluidics 2003 (ASME IMECE, 2003).

7 Zusammenfassung

Die Techniken der Kernmagnetischen Resonanz (NMR) liefern wertvolle Informationen über Transportphänomene in komplexen Systemen wie beispielsweise poröse Medien. Die vorliegende kumulative Doktorarbeit stellt zahlreiche NMR-Kartierungstechniken vor, mit deren Hilfe nützliche Informationen über Transportgrößen in einfachen und auch komplizierten Geometrien erfasst werden konnten. Es wurden dazu NMR-Methoden für „velocity mapping“, „acceleration mapping“, „ionic current density mapping“ und „electro-hydrodynamic mapping“ entwickelt. Ergänzende Informationen über die Probe können in den meisten Fällen mittels „Computational Fluid Dynamics“ (CFD)-Simulationen gewonnen werden. Dieses Verfahren gestattet einen direkten Vergleich zwischen gemessenen und simulierten Daten. Relativ einfache Kanalsysteme dienten dabei als Testobjekte für Mikrofluidik, komplexere Perkolationsobjekte hingegen als Modelle für reale poröse Medien.

Die in dieser Arbeit entwickelte „acceleration mapping“ Technik gestattet direktes Messen der räumlichen Beschleunigungsverteilung. Mit experimentell aufgenommenen Beschleunigungskarten wurden die gewundenen Bahnen der Flüssigkeitsströmung in ortskorrelierten Perkolationsobjekten aufgezeigt.

Mit den ortskorrelierten Perkolationsobjekten wurde versucht, die hohe Konnektivität der Porenräume realer poröser Materialien, wie sie in der Natur vorkommen, nachzuahmen.
Mit Hilfe von NMR-Bildgebungs-Methoden und CFD-Simulationen konnten die Testobjekte nach geometrischen (Perkolationsschwelle, Korrelationslänge, Fraktale Dimension) und dynamischen Gesichtspunkten charakterisiert werden.

Transportphänomene als Folge von Gradienten des äußeren Drucks oder der elektrischen Feldstärke sind für viele Mikrofluidik-Anwendungen von besonderem Interesse. In dieser Arbeit werden die Flussverteilungen bei Elektroosmose und hydrodynamischen Druckgradienten sowie die ionische Stromdichteverteilung im Porensystem verglichen. Das Auftreten geschlossener Schleifen und starker Wirbel wurde experimentell nachgewiesen. Elektro-osmotischer Fluss und Stromdichte-Kartierung lassen Abweichungen von der Helmholtz/Smoluchovski Gleichung für komplizierte Systeme erkennen. Alle zuvor erwähnten NMR-Techniken (Geschwindigkeits-, Beschleunigungs-, Elektroosmose- und Stromdichte-Kartierung) können unabhängig voneinander am gleichen Modellobjekt angewandt werden, um so einen möglichst weiten Bereich an Informationen über den vorliegenden Transportprozess zu erhalten

8 Original papers for cumulative thesis

[I] B.Buhai, A. Hakimov, I. Ardelean and R. Kimmich, **NMR acceleration mapping in percolation model objects**, J. Magn. Reson. 168 (2004)

[II] B.Buhai, A. Kühnle, and R. Kimmich, **NMR flow mapping and computational fluid dynamics in Ising-correlated percolation model objects**, New Journal of Physics 7 (2005)

[III] B.Buhai, and R. Kimmich, **Dissimilar Electro-Osmotic Flow and Ionic Current Recirculation Patterns in Porous Media Detected by NMR Mapping Experiments**, Phys. Rev. Lett. 96, 174501 (2006)

[IV] B.Buhai, T. Binser and R. Kimmich, **Electro-osmotic flow, ionic currents, and pressure induced flow in microsystem channel networks: NMR mapping and computational fluid dynamics simulations**, Appl. Magn. Reson., in press (2006)

I

B.Buhai, A. Hakimov, I. Ardelean and R. Kimmich,

NMR Acceleration Mapping in Percolation Model Objects

Journal of Magnetic Resonance **168,** p175-185 (2004).

Available online at www.sciencedirect.com
SCIENCE @ DIRECT®
Journal of Magnetic Resonance 168 (2004) 175–185
JMR Journal of Magnetic Resonance
www.elsevier.com/locate/jmr

NMR acceleration mapping in percolation model objects

Bogdan Buhai,[a] Aidar Hakimov,[a] Ioan Ardelean,[b] and Rainer Kimmich[a,*]

[a] *Sektion Kernresonanzspektroskopie, Universität Ulm, 89069 Ulm, Germany*
[b] *Department of Physics, Technical University, 3400 Cluj-Napoca, Romania*

Received 19 December 2003; revised 18 February 2004

Abstract

An NMR microscopy technique is described that permits direct mapping of local accelerations. The method is tested with water flow through a random site percolation model object and compared with computational fluid dynamics simulations. A general formalism, the "polygon rule," is reported for the design of gradient pulse sequences for phase encoding of higher order motions, or, in other words, for compensation of phase shifts by lower motional orders.
© 2004 Elsevier Inc. All rights reserved.

Keywords: Acceleration; NMR mapping; Percolation; Porous media

1. Introduction

In recent papers [1–5] we have reported on microscopic NMR mapping experiments and simulations of transport in fluid filled percolation model objects of porous media. The objective was to study and learn the laws governing coherent or incoherent propagation of measurands specifying transport under complex pore space constraints. Phenomena of interest so far were coherent flow characterized by velocity maps, incoherent flow, and diffusion leading to hydrodynamic dispersion, thermal conduction, and convection causing temperature distributions and hydrodynamic flow patterns, and electric currents in electrolyte solutions. A comprehensive description of such methods can be found in recent reviews [6,7].

The advantage of percolation model objects first simulated as templates on a computer and then fabricated with the aid of milling [8] or lithography [9] techniques is in the first place that pore space topologies based on well-defined generation algorithms can be realized. Another advantage is that the boundary conditions of the pore space are known and can directly be used for numerical simulations of the transport quantities. Such simulations help to plan and design experiments properly so that time and effort consuming failures are avoided. Comparisons of experimental data and their simulated counterparts permit one moreover to judge the reliability both of the numerical simulation method and of the measuring technique. The meaningfulness of such combined study is thus particularly well founded.

In the present paper we report on an NMR method for direct mapping of locally stationary accelerations of liquids flowing through porous systems. Of course, having a velocity map in principle implies the information on local accelerations as well. However, flow measurements with the standard phase encoding technique anticipates [10–12] *constant* velocities so that the existence of any acceleration leads to additional phase shifts causing experimental velocity artefacts. Even if a velocity map were available with the required accuracy, it always refers to *average* values in the voxels resolved in the experiment. Reconstructing particle trajectories based on such voxel-average velocities and from these local accelerations unavoidably entails strong errors as test experiments demonstrated. The error of such evaluations depends on the spatial variation of the velocity field and the spatial resolution of the mapping experiment. In other words, the correlation length of the velocity field must be much larger than the spatial resolution in order to obtain reliable acceleration vectors from a velocity vector field.

---

[*] Corresponding author. Fax: +49-731-5023150.
E-mail address: rainer.kimmich@physik.uni-ulm.de (R. Kimmich).

1090-7807/$ - see front matter © 2004 Elsevier Inc. All rights reserved.
doi:10.1016/j.jmr.2004.02.013

In order to avoid this difficulty it appears to be worthwhile to directly phase encode accelerations while phase shifts by velocities stationary with respect to magnitude and direction are suppressed. Such direct mapping experiments are expected to result in more reliable voxel-average accelerations. The condition is that the local acceleration is stationary in order to avoid any higher-order phase encoding errors. This, however, is not a problem, since the relatively low time resolution of NMR microscopy always stipulates stationarity on an imaging time scale of several minutes if not hours. Rapidly time variable flow patterns as they occur in turbulent flow [13–15] can be studied by NMR only in the frame of particularly favourable time resolutions. Here we focus on laminar flow where the local velocity vector is a function of position but not of time.

2. The acceleration mapping technique

The basic element of phase encoding of accelerations is a sequence of bipolar field gradients as illustrated in Fig. 1. The effect of such gradient pulses is a phase shift of the spin coherences proportional to the local acceleration whereas phase shifts by stationary velocities and for static nuclei are compensated [11,12,16].

Consider the trajectory of a nucleus as a function of time. The position component along the field gradient, which is arbitrarily assumed along the x direction of the laboratory frame, evolves according to the following Taylor series:

$$x(t) = x_0 + v_{x0}t + \frac{a_{x0}}{2}t^2 + \cdots, \tag{1}$$

where x_0, v_{x0}, and a_{x0} are the initial position, velocity, and acceleration components, respectively. Higher order terms (referring to locally time-dependent accelerations) must be neglected due to the low time resolution intrinsic to magnetic resonance imaging experiments. The experiments to be described below were furthermore performed under conditions of locally *stationary* accelerations: All higher order terms therefore vanish by definition. Stationary flow patterns and pressure gradients stipulate locally stationary velocities and accelerations. Note that we record accelerations of spins being *at certain positions* (voxels) during the measurements rather than accelerations of a certain tracer particle experiencing varying accelerations when travelling through different voxels.

The phase shift adopted in the presence of a field gradient, $G_x = G_x(t)$, in the period $0 \leqslant t \leqslant T$ is

$$\phi(T) = \int_0^T \Omega[x(t)]\,\mathrm{d}t = \gamma_n \int_0^T G_x(t)x(t)\,\mathrm{d}t, \tag{2}$$

where $\Omega(x) = \gamma_n Gx$ is the angular frequency offset at the position $x = x(t)$ due to the spatially constant field gradient. Inserting Eq. (1) in Eq. (2) gives

$$\begin{aligned}\Phi(T) &= \gamma_n \left[x_0 \underbrace{\int_0^T \zeta(t)G_x(t)\,\mathrm{d}t}_{m_0} + v_{x0} \underbrace{\int_0^T \zeta(t)G_x(t)t\,\mathrm{d}t}_{m_1} \right. \\ &\qquad \left. + \frac{1}{2}a_{x0} \underbrace{\int_0^T \zeta(t)G_x(t)t^2\,\mathrm{d}t}_{m_2} \right] \\ &= \Phi_0(T) + \Phi_1(T) + \Phi_2(T),\end{aligned} \tag{3}$$

where γ_n is the gyromagnetic ratio and m_n $(n = 0, 1, 2)$ is the nth moment of the gradient pulse sequel during the interval T. The function $\zeta(t)$ accounts for the phase reversal by the 180° RF pulse in the middle of the spin echo pulse sequence (see Fig. 1):

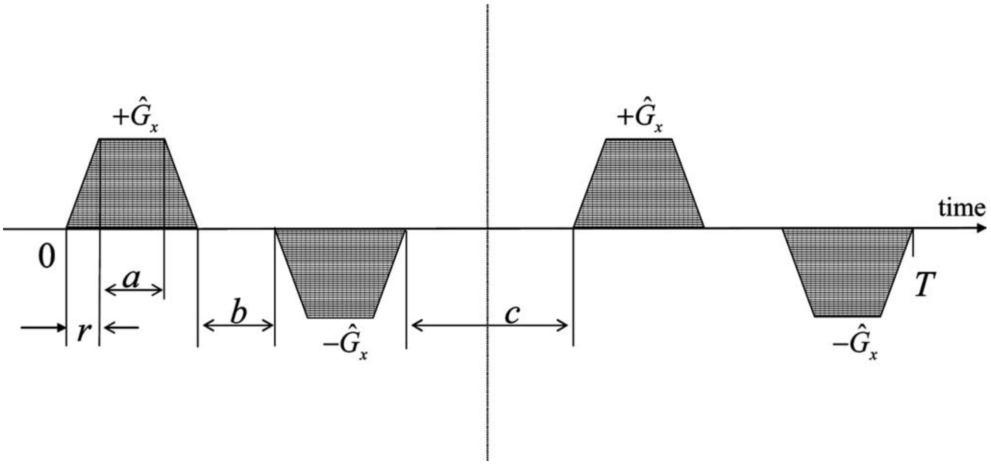

Fig. 1. Bipolar field gradient pulses symmetric to the 180° radio frequency (RF) pulse (dotted line) of a spin-echo sequence. Phase shifts of spin coherences proportional to the second moment, and, hence, to the local acceleration are generated, whereas the zeroth and first moment vanish. That is, field gradient pulses of this sort suppress any phase shifts due to position and constant velocity.

$$\zeta(t) = \begin{cases} +1 & \text{before the } 180^\circ \text{ pulse,} \\ -1 & \text{after the } 180^\circ \text{ pulse.} \end{cases} \tag{4}$$

The problem is now to make the zeroth and first moments vanish while the second moment remains finite. The simplest solution is the sequence shown in Fig. 1. The zeroth and first moments obviously vanish, i.e.,

$$\begin{aligned} \Phi_0(T) &= \gamma_n x_0 \int_0^T \zeta(t) G_x(t)\,\mathrm{d}t \\ &= \gamma_n x_0 \int_0^{4a+2b+c+8r} \zeta(t) G_x(t)\,\mathrm{d}t = 0 \end{aligned} \tag{5}$$

and

$$\begin{aligned} \Phi_1(T) &= \gamma_n v_{x0} \int_0^T \zeta(t) G_x(t) t\,\mathrm{d}t \\ &= \gamma_n v_{x0} \int_0^{4a+2b+c+8r} \zeta(t) G_x(t) t\,\mathrm{d}t = 0. \end{aligned} \tag{6}$$

The coherence phase shift due to the second moment reads

$$\begin{aligned} \Phi_2(T) &= \frac{1}{2}\gamma_n a_{x0} \int_0^T \zeta(t) G_x(t) t^2\,\mathrm{d}t \\ &= \frac{1}{2}\gamma_n a_{x0} \int_0^{4a+2b+c+8r} \zeta(t) G_x(t) t^2\,\mathrm{d}t \\ &= \frac{1}{2}\gamma_n a_{x0} \hat{G}_x \big(16r^3 + 4a^3 + 20a^2 r + 32ar^2 + 2ab^2 \\ &\quad + 6a^2 b + 2b^2 r + 12br^2 + 4a^2 c + 8cr^2 \\ &\quad + 4acb + 4cbr + 12acr + 18abr\big) \propto a_{x0}. \end{aligned} \tag{7}$$

This phase shift is proportional to the local acceleration and will be taken as the quantity to be mapped in the experiments.

The complete pulse sequence for the acceleration maps is schematically shown in Fig. 2 (leaving the gradient pulse ramps away for simplicity). In this pulse sequence, phase encoding of the acceleration components and spatial encoding for the mapping are

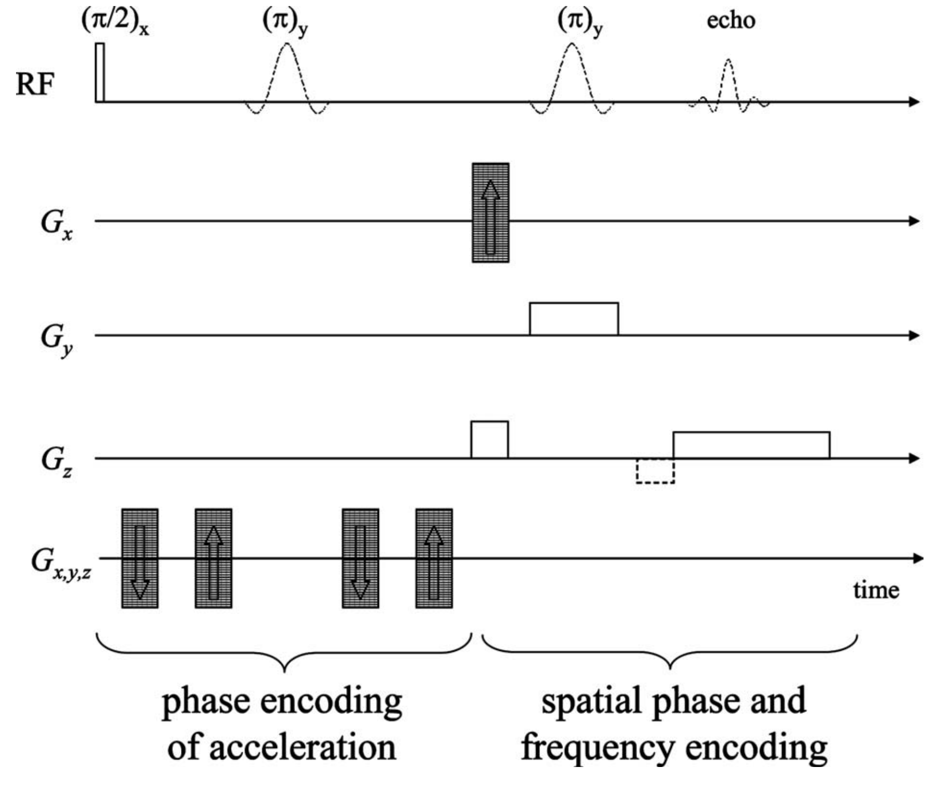
$(\pi/2)_x$
$(\pi)_y$
$(\pi)_y$
echo
RF
G_x
G_y
G_z
$G_{x,y,z}$
time
phase encoding of acceleration
spatial phase and frequency encoding

Fig. 2. Typical RF and field gradient pulse sequence used for NMR acceleration mapping experiments. A standard (secondary) Hahn spin echo imaging sequence is used in combination with two pairs of bipolar gradient pulses. The ramps of the gradient pulses are not shown for simplicity. The (second) π pulse is applied in the presence of a gradient G_y and serves the selection of the desired slice. The other two spatial dimensions are probed by gradient pulses G_z (frequency encoding) and G_x (phase encoding). The phase encoding gradient, G_x is incremented in a series of successive transients. To acquire the acceleration vector field, all three components must be probed one by one. These components are phase encoded by the first two pairs of bipolar gradient pulses which are also incremented in a series of (in our case nine) transients. For quasi two-dimensional objects as they are studied in the present investigation, the data set acquired in this way consists of two four-dimensional matrices. Fourier transforms in all four dimensions lead to conjugated data sets describing the two in-plane acceleration vector components for each voxel. The imaging part of the pulse sequence is kept particularly short in order to avoid flow phase encoding by gradient pulse pairs. In critical situations it is more favourable to place the refocusing pulse of the read gradient in the form of a negative lobe directly before the read gradient pulse in order to reduce the undesired phase encoding further (lobe drawn with broken lines).

performed in two separate free-evolution intervals of the spin coherences by using a secondary Hahn echo RF pulse sequence. In principle, all phase encoding could be done simultaneously in one free-evolution interval of an ordinary spin echo sequence, since the gradient pulses are incremented independently from each other. However, from the practical standpoint it turned out that the sequential employment of the acceleration and position phase-encoding pulses leads to more stable and reliable results.

A certain source of experimental artefacts is that the gradient pulses used in the second (imaging) half of the pulse sequence are not compensated for phase shifts by velocities. That is, the spatial phase-encoding dimension of the imaging process may be affected by such spurious phase shifts. In principle this could be avoided by the use of "velocity (and acceleration) compensated" gradient pulses [11,12]. However, the pulse would then become too complicated. We therefore preferred to keep the imaging part so short that such artefacts practically did not matter. A generalized design rule for gradient pulses compensating motion induced phase shifts of any order [17] will be presented in the Appendix.

3. Model objects and instruments

The proposed technique was tested with liquid flow through two different pore space model objects shown in Figs. 3A and B. Computational fluid dynamics simulations were moreover performed for the same pore space topologies and under the same flow conditions. The test object represented by Fig. 3A was designed on a computer using the software package Gambit 2.1. The more complex percolation cluster in Fig. 3B was produced with the aid of a random number generator. Both computer-generated pore space structures were fed to a digital circuit board plotter (LPKF, "Leiterplatten–Konturfräsen") for milling the pore space into 3 mm thick polystyrene plates [1]. The milling depth was 2 mm and the position resolution of the milling machine was 6.35 μm.

The samples were composed of stacks of 10 identical quasi two-dimensional model objects in order to improve the signal-to-noise ratio. The pore space was filled with water. It was taken care that no gas bubbles occurred. Constant flow during the experiment was ensured by the hydrostatic pressure resulting from a reservoir 1.5 m above the sample level. The reservoir was permanently refilled with the aid of a peristaltic pump. The total flow rate was in the range 0.1–0.3 ml/s. The water was doped with $CuSO_4$ in order to reduce the spin–lattice relaxation time T_1 to about 500 ms. The Reynolds number is estimated to be $Re = 0.2$, which is far below the critical value where turbulence starts to become effective.

Acceleration maps were recorded using the pulse sequence shown in Fig. 2. The imaging parameters were: repetition time $T_R = 2$ s, number of scans $N_s = 16$, echo time $T_E = 22$ ms. The tomograph consisted of a home made RF console and a 4.7 T magnet with a horizontal 40 cm room temperature bore. The resonator was of the birdcage type. The maximum gradient was 50 mT/m in each direction (x, y, and z). All measurements were performed at room temperature.

4. Computational fluid dynamics simulation method

The computational fluid dynamics simulations were performed on a PC using the software package FLUENT 5.5.14 based on the finite volume method (FVM). For rendering maps the package IDL 5.3 was employed.

In the case of the circle arc test object the mesh used was of QUAD type (see [19] for more details). The channels were subdivided into a minimum of six smaller subchannels. The resulting extension of the "finite" elements was 60 μm × 60 μm. The mesh net was finer in the interior of the channels in order to achieve a better convergence of the solution.

In the case of the random percolation model each matrix point was represented by 5 × 5 "knots" or "elements." The convergence criteria was set to a residuum of 10^{-5}. Obstacles in the pore space are defined by vanishing flow velocity at the corresponding knots. In this way periodic meshing was possible so that the same resolution, 60μm × 60μm, applies to all flow paths. In the simulation the same parameters (fluid viscosity, pressure difference exerted to the object, and object size) were assumed as in the NMR experiments.

The simulation of acceleration maps requires a consideration different from the experimental procedure. The FVM method used in the software package FLUENT 5.5 does not allow direct rendering of acceleration maps. Rather, processing of velocity maps was necessary based on the software package IDL 5.3. For these derivations an Eulerian approach was employed anticipating the two-dimensional velocity vector field corresponding to our quasi two-dimensional model objects:

$$\vec{v} = (v_x(x,y,t), v_y(x,y,t)). \tag{8}$$

The local acceleration components in the object plane are then given by

$$\begin{aligned} a_x = a_x(x,y) &= \frac{\mathrm{d}v_x}{\mathrm{d}t} = \frac{\partial v_x}{\partial t} + \frac{\partial v_x}{\partial x}\frac{\partial x}{\partial t} + \frac{\partial v_x}{\partial y}\frac{\partial y}{\partial t} \\ &= \frac{\partial v_x}{\partial t} + \frac{\partial v_x}{\partial x}v_x + \frac{\partial v_x}{\partial y}v_y, \end{aligned} \tag{9}$$

$$\begin{aligned} a_y = a_y(x,y) &= \frac{\mathrm{d}v_y}{\mathrm{d}t} = \frac{\partial v_y}{\partial t} + \frac{\partial v_y}{\partial x}\frac{\partial x}{\partial t} + \frac{\partial v_y}{\partial y}\frac{\partial y}{\partial t} \\ &= \frac{\partial v_y}{\partial t} + \frac{\partial v_y}{\partial x}v_x + \frac{\partial v_y}{\partial y}v_y. \end{aligned} \tag{10}$$

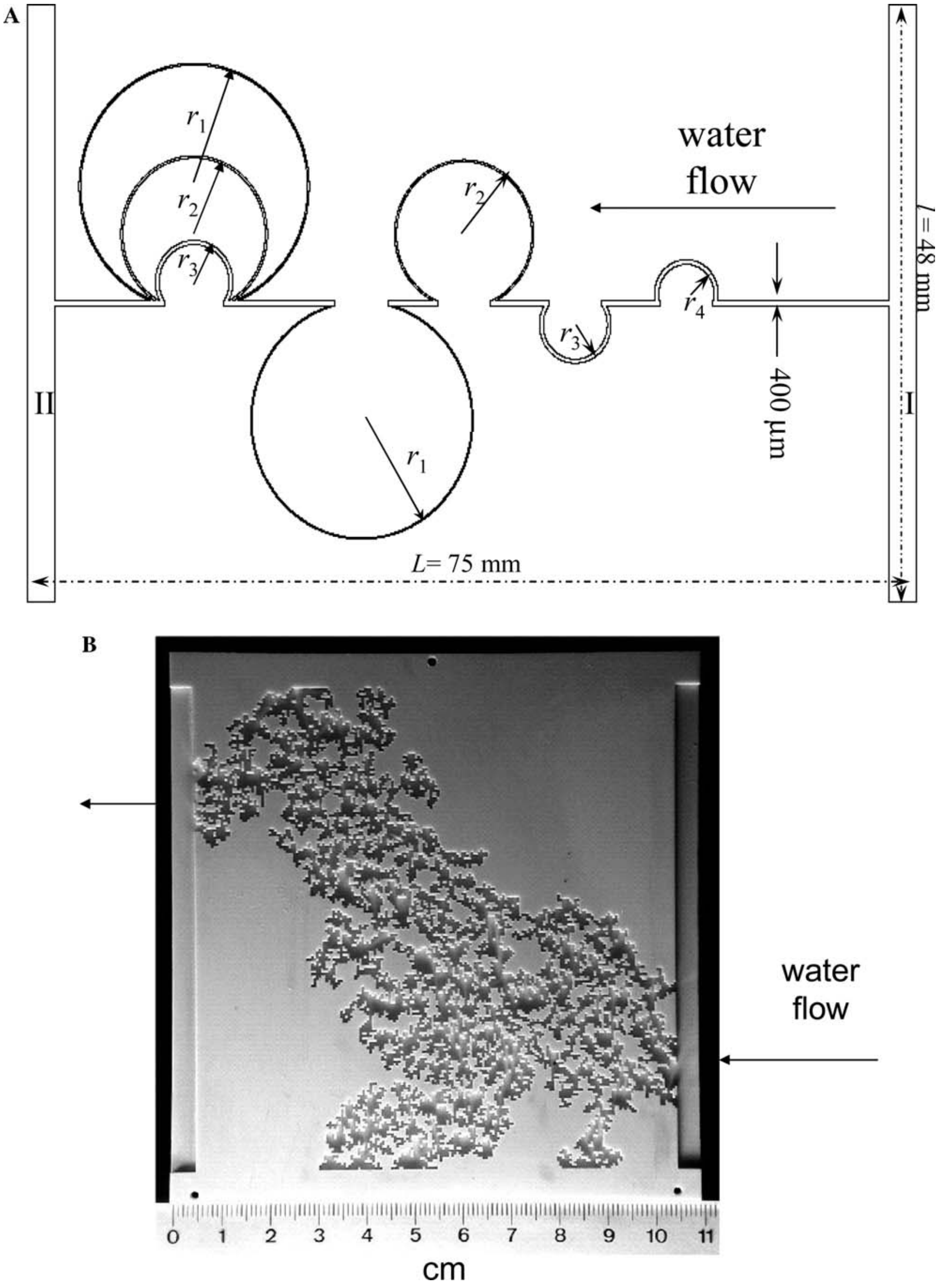

Fig. 3. Quasi two-dimensional test objects for acceleration mapping experiments and simulations. (A) Topology consisting of a series of sequential or parallel circle arc channels of various radii ($r_1 = 10.5$ mm, $r_2 = 7.5$ mm, $r_3 = 3.5$ mm, and $r_4 = 3$ mm). The depth of the channels was 2 mm and the width was 400 µm. The sections marked with ***I*** and ***II*** represent the inflow and outflow compartments, respectively. (B) Quasi two-dimensional random site percolation cluster object (photograph) based on a square base lattice of 200×200 sites occupied with a probability $p = 0.6$ which is above the percolation threshold [8,18]. The fractal dimension is $d_f = 1.9$, and the correlation length is $\xi = 1.95$ mm.

Under steady-state conditions, all explicit time dependences vanish, i.e., $\partial v_x/\partial t = \partial v_y/\partial t = 0$. The derivatives $\frac{\partial v_x}{\partial x}, \frac{\partial v_x}{\partial y}, \frac{\partial v_y}{\partial y}, \frac{\partial v_y}{\partial x}$ in relations (9) and (10) are provided by the FLUENT package. For further processing, the IDL 5.3 software was employed resulting in the desired acceleration component fields. The magnitude is then obtained from

$$a = \sqrt{a_x^2 + a_y^2}. \tag{11}$$

Note that the acceleration components given at Eqs. 9 and 10 depend on the (voxel) position but not on time since all velocity components are assumed to be locally stationary and merely change from position to position.

5. Results

Fig. 4 shows a comparison of experimental and simulated acceleration maps for the circle arc test object

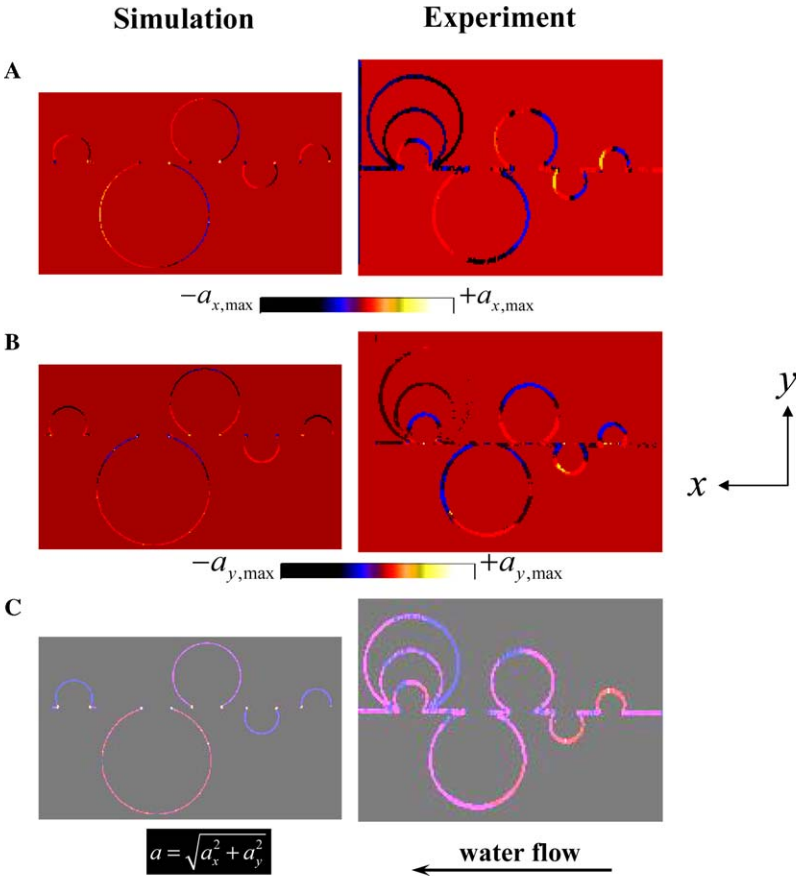

Fig. 4. Maps of the x component (A), y component (B), and the magnitude (C) of the mean acceleration for the test structure represented by Fig. 3A. The experimental data (right column) have been recorded with the aid of the pulse sequence shown in Fig. 2. The left column shows simulated data for comparison.

represented by Fig. 3A. The mean acceleration by flow in the circle arc channels is due to changes of the velocity vector direction (see components a_x and a_y in Fig. 4A and B), whereas the mean magnitude remains constant for given circle radius (see Fig. 4C).

The echo time was $T_E = 26\,\text{ms}$. For a spatial resolution $\Delta x = 386\ \mu\text{m}$ the maximum velocity that can reliably be detected in the experiments is limited by $\Delta x/T_E = 14.8\,\text{mm/s}$, which is within the velocity field-of-view, $-90\ \text{mm/s} < v < +90\ \text{mm/s}$.

The flow distribution among the three circle arc channels connected in parallel depends on the flow resistance. For a circular cross section of the channels and if Hagen/Poiseuille's law for the flow rate is valid, the flow resistance is

$$Q = \frac{\pi a^4 \Delta P}{8L\eta}, \tag{12}$$

where L is the length of the channel section (i.e., of a circle arc with a certain radius) across which the pressure difference ΔP is exerted, η is the viscosity of the fluid, and a is the radius of the channel cross section. The channel length of the ith circle arc is

$$L_i = (2\pi - \theta_i)r_i \quad i = 1..3 \text{ and } L_1 > L_2 > L_3, \tag{13}$$

where θ_i and r_i are the angle and the radius defining the extension of the ith circle arc, respectively. The mean flow velocity is related to the flow rate according to

$$v = Q/4\pi a^2. \tag{14}$$

Combining Eqs. (12)–(14) leads to a mean flow velocity in the ith circle arc given by

$$v_i = \frac{a^2 \Delta P}{32\eta L_i} \quad i = 1..3. \tag{15}$$

The pressure difference ΔP is the same for all three channels connected in parallel. The mean flow velocity and the channel length are consequently inversely proportional to each other, so that

$$L_1 > L_2 > L_3 \Rightarrow v_1 < v_2 < v_3. \tag{16}$$

The mean velocities v_1 and v_2 turned out to be too small to be detectable in the experiments. The same consequently applies to the acceleration. On the other hand, if the flow rate would be increased in order to make all mean velocities detectable, the problem would be that the velocity in other sections of the object would become too large.

The mean radial acceleration depends on the circle arc radius according to

$$a = \frac{v^2}{r}. \tag{17}$$

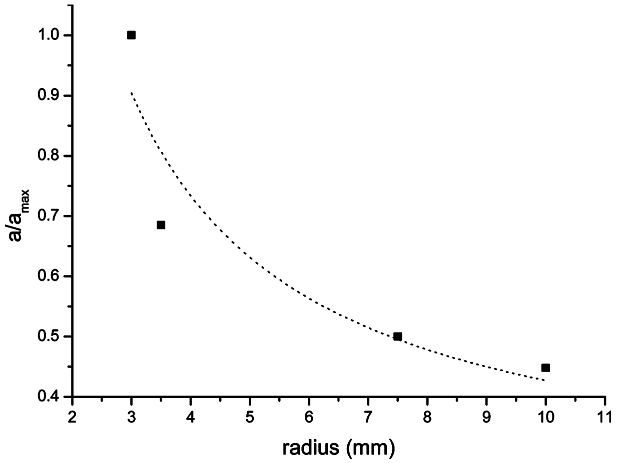

Fig. 5. Mean radial acceleration as a function of the circle arc radius in the test object represented by Fig. 3A. The black rectangles represent experimental data, and the dotted line was fitted according to Eq. (17).

Since the mean velocity in the sequential circle arcs is constant, we expect the proportionality

$$a \sim \frac{1}{r}, \tag{18}$$

which is verified in the experiments with reasonable accuracy (see Fig. 5).

Fig. 6 shows maps of the mean acceleration and mean velocity in the random site percolation cluster shown in Fig. 3B both for experimental and simulated data. All matrix voxels were blackened using a matrix mask deduced from a black-and-white converted spin density map. In this way, noise in matrix voxels whose phase would be misinterpreted by the Fourier processing analysis as a distribution of accelerations or velocities, is avoided. The flow patterns both with respect to flow velocity and acceleration are well reproduced in all cases.

The percolation cluster consist of two main components: the dead-ends that carry no flow, and the so-called backbone which is the multiply-connected part of the cluster through which the fluid flows [18,20]. The suppression of stagnant zones reveals transport pathways more clearly in the form of the cluster backbone

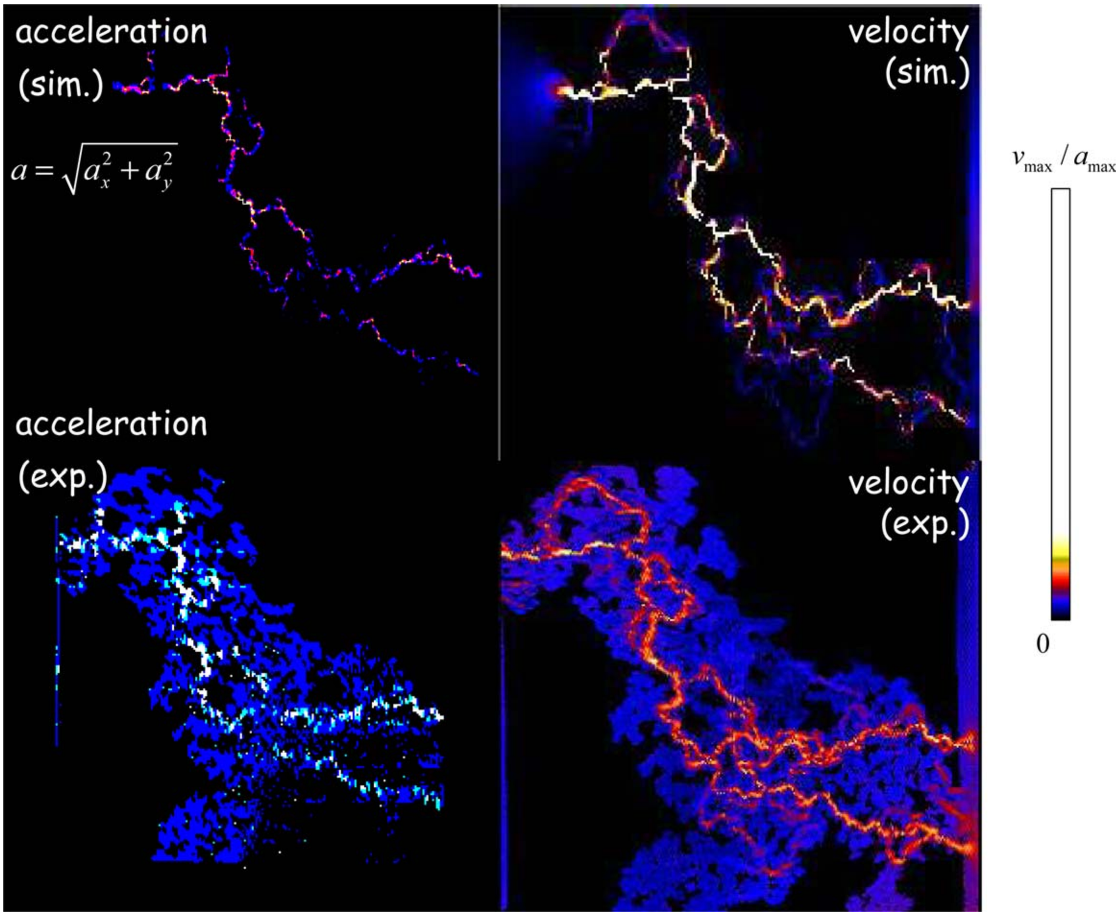

Fig. 6. Experimental and simulated maps of the mean acceleration magnitude (left column) and the mean velocity magnitude (right column) in a random site percolation cluster ($p = 0.6$, $p - p_c = 0.002$). The model object is shown in Fig. 3B.

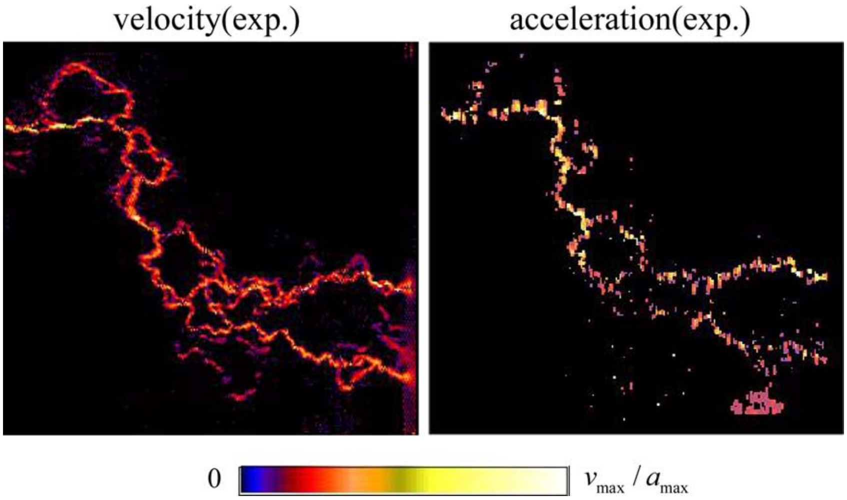

Fig. 7. "Backbones" of the experimental transport patterns shown in Fig. 6. These maps were obtained by blackening all pixels with a velocity or an acceleration below the respective noise level ($v \leqslant v_n$ or $a \leqslant a_n$). That is, all stagnant zones are removed. Only those pixels representing finite velocities or accelerations are shown.

[1]. The method used here was to black all voxels where the acceleration is below the acceleration noise level, $a \leqslant a_n$.

There are significant differences between velocity and acceleration maps (see Fig. 7). The velocity maps show pathways of a more continuous character, whereas the acceleration strongly fluctuates along the flow channels. That is, the acceleration is only in certain voxels large enough to be detectable above the noise level of the experimental set-up. These sections correspond to bottle necks and strongly curved pathways where flow is strongly accelerated or decelerated.

6. Discussion and conclusions

It was demonstrated that accelerations in flow patterns through complex porous media can directly be mapped by an NMR technique in addition to conventional flow velocity mapping. Since all transport quantities recorded by NMR microscopy techniques refer to voxel averages, the *direct* measurement of spatial acceleration distributions is considered to be more reliable than the reconstruction based on maps of the mean velocity.

Acceleration maps specifically highlight bottlenecks and strongly curved pathways of flow. They are therefore considered to be indicative for corresponding topology elements of the pore space.

In our previous papers [1–5] we pursued the strategy to use maps of transport quantities for the assessment of laws relating parameters of the pore space structure and of the transport patterns. This objective is facilitated by well-defined model percolation clusters where the pore space is defined by complete coordinate sets. Boundary conditions on this basis can be used for computational fluid dynamics simulations which then can be compared with experimental data. In all cases good coincidence was found. That is, the simulation method, the fabrication procedure of the model objects, and the NMR mapping technique are shown to be reliable and essentially free of artefacts. Simulations can thus be used to design experimental protocols and to predict the feasibility of investigations prior to the experiments. This sort of examination is expected to be useful in the broad porous media field where experimental techniques and the theoretical background are still in a rather rudimentary state [20–27].

The present study refers to (quasi) two-dimensional pore spaces. The extension to three dimensions is readily possible but time consuming, since then three four-dimensional data sets have to be acquired for the three components of the acceleration vector. In this respect a combination with fast imaging techniques is expected to be favourable [23,24].

Acknowledgments

This work was supported by the Deutsche Forschungsgemeinschaft and the Alexander von Humboldt Foundation.

Appendix A. The "polygon rule"

The gradient pulse train shown in Figs. 1 and 2 produce phase shifts proportional to stationary accelerations. Other, more complicated variants serving the same purpose exist provided that the corresponding moment conditions are fulfilled. The question to be dealt with in this appendix is whether there is a general rule permitting one to design the simplest gradient pulse sequences for the compensation of phase shifts due to any order of motions so that phase shifts due to all higher orders become selectively relevant.

The position of a nucleus can be represented by the expansion

$$\vec{r}(t)=\vec{r}_0+\vec{v}_0t+\frac{\vec{a}_0t^2}{2}+\cdots, \qquad (A.1)$$

where $\vec{r}_0$, $\vec{v}_0$, and $\vec{a}_0$ are the initial position, velocity, and acceleration vectors, respectively. The phase shift in an interval T in the presence of time-varying gradients $\vec{G}(t)$ is given by

$$\phi(T)=\gamma\int_0^T\vec{G}(t)\cdot\vec{r}(t)\,\mathrm{d}t. \qquad (A.2)$$

Inserting Eq. (18) gives the moment series

$$\begin{aligned}\phi(T)&=\gamma\left[\vec{r}_0\cdot\int_0^T\vec{G}(t)\,\mathrm{d}t+\vec{v}_0\cdot\int_0^T\vec{G}(t)t\,\mathrm{d}t+\frac{1}{2}\vec{a}_0\cdot\int_0^T\vec{G}(t)t^2\,\mathrm{d}t+\cdots\right]\\&=\phi_0(T)+\phi_1(T)+\phi_2(T)+\cdots. \qquad (A.3)\end{aligned}$$

Motion-compensated gradient pulse trains making the diverse orders in Eq. (A.3) vanish consist of alternating gradient lobes arranged symmetrically (no 180° RF pulse in between) or inversely symmetrically (with an intermittent 180° RF pulse). The pulse trains shown in Figs. 1 and 2 are examples of the 180° pulse variant, those shown in Figs. 8 and 9 are valid in the absence of 180° pulses.

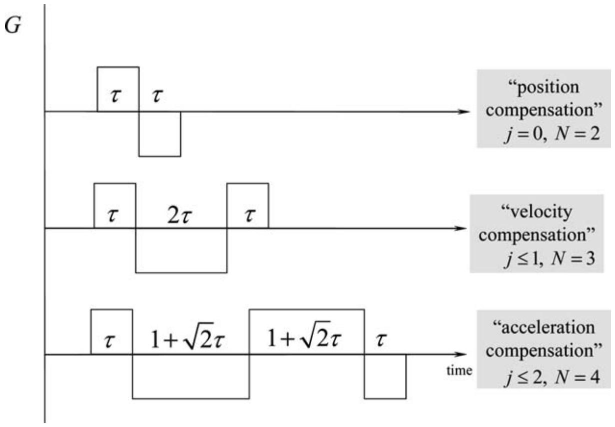
G
τ τ
"position compensation" $j=0$, $N=2$
τ 2τ τ
"velocity compensation" $j\le 1$, $N=3$
τ 1+√2τ 1+√2τ τ
time
"acceleration compensation" $j\le 2$, $N=4$

Fig. 8. Typical gradient lobe trains for the compensation of phase shifts due to positions ($j=0$), stationary velocities ($j=1$) and stationary accelerations ($j=2$) in the absence of any 180° RF pulses.

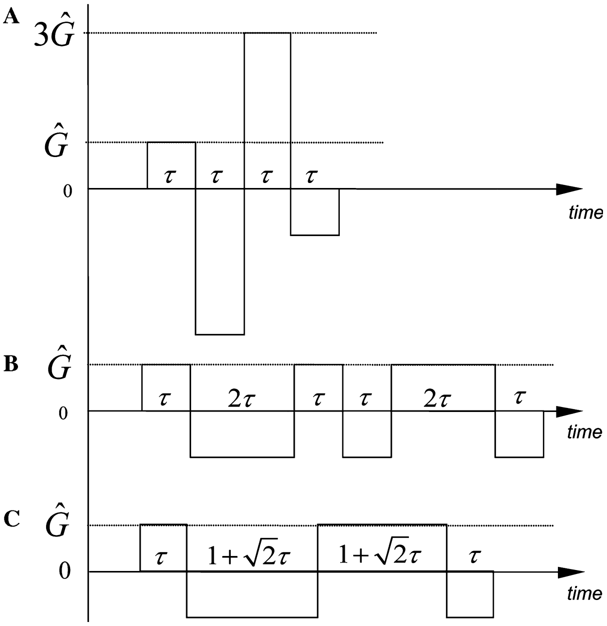

Fig. 9. Field-gradient pulse sequences for the compensation of phase shifts due to stationary accelerations: (A) Gradient pulse train based on different gradient amplitudes proposed in [25]. (B) Gradient pulse train based on alternating gradients proposed in [16]. (C) Gradient pulse train designed according to the polygon rule ($j=2$; $N=j+2=4$).

Consider now a gradient pulse train including N alternating lobes of durations $\tau_1\ldots\tau_N$ and equal amplitudes of integer multiples of $\hat{G}$, where no RF pulses are involved. That is, rectangular gradient pulse shapes are assumed neglecting any switching ramps (see Fig. 8). The scalar vector products in Eq. (A.3) mean that only collinear components for the gradient vector and the dynamic motion vectors are relevant. We will denote these components by $\hat{G}$ and J, where J stands for r_{x0}, v_{x0}, a_{x0}, etc. The jth order phase shift thus reads

$$\begin{aligned}\phi_j(T)=\frac{1}{(j+1)!}\gamma J\hat{G}\Big[&2\tau_1^{j+1}+\cdots+2(-1)^{N-1}\\&\times(\tau_1+\cdots+\tau_{N-1})^{j+1}+(-1)^N(\tau_1+\cdots+\tau_N)^{j+1}\Big].\end{aligned} \qquad (A.4)$$

For example, the second-order term representing phase shifts due to stationary accelerations is

$$\begin{aligned}\phi_2(T)=\frac{1}{6}\gamma a_0\hat{G}\Big[&2\tau_1^3-2(\tau_1+\tau_2)^3+\cdots+2(-1)^{N-1}\\&\times(\tau_1+\cdots+\tau_{N-1})^3+(-1)^N(\tau_1+\cdots+\tau_N)^3\Big].\end{aligned} \qquad (A.5)$$

There is a mathematically simple method for the calculation of the gradient lobe widths leading to vanishing jth and lower order phase shifts. The number of the lobes must be $N=j+2$. The duration of the lobes can be expressed by

$$\tau_i=\tau\frac{\sin\left(\pi\frac{i-1}{j+2}\right)+\sin\left(\pi\frac{i}{j+2}\right)}{\sin\left(\frac{\pi}{j+2}\right)}, \qquad (A.6)$$

where $\tau\equiv\tau_1$. For example, if $j=2$ and $N=4$ we have $\tau_1=\tau$, $\tau_2=(1+\sqrt{2})\tau$, $\tau_3=(1+\sqrt{2})\tau$, $\tau_4=\tau$ for an acceleration compensated gradient pulse train. The

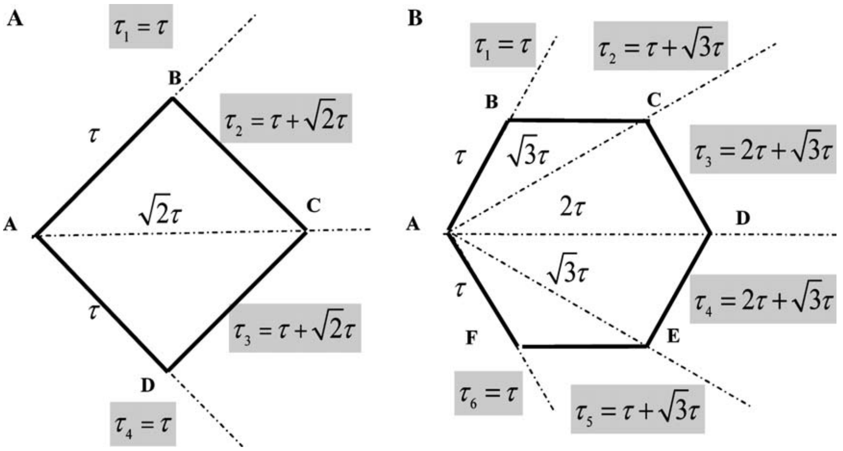
A
$\tau_1 = \tau$
B
$\tau_2 = \tau + \sqrt{2}\tau$
τ
$\sqrt{2}\tau$
A
C
τ
$\tau_3 = \tau + \sqrt{2}\tau$
D
$\tau_4 = \tau$
B
$\tau_1 = \tau$
$\tau_2 = \tau + \sqrt{3}\tau$
B
C
τ
$\sqrt{3}\tau$
$\tau_3 = 2\tau + \sqrt{3}\tau$
2τ
A
D
$\sqrt{3}\tau$
τ
$\tau_4 = 2\tau + \sqrt{3}\tau$
F
E
$\tau_6 = \tau$
$\tau_5 = \tau + \sqrt{3}\tau$

Fig. 10. The *polygon rule* for the determination of the pulse lengths implied in motion compensating gradient pulse sequences. For the compensation of phase shifts due to the jth and lower motion orders one needs $N = j + 2$ gradient lobes. The sign of the gradient lobes is alternating in the sequence of their appearance (if no phase inverting 180° RF pulse is applied in between). An N-fold polygon (solid lines) is formed with the "origin" in point A. Auxiliary rays (dotted lines) are drawn from A to the other polygon corners. The durations of the gradient lobes are then proportional to the lengths (of the first and last lobe) or double sums of adjacent line-segments (see the shadowed expressions). (A) Compensation of phase shifts due to stationary accelerations, velocities, and positions; phase encoding due to higher order motions: The maximum order to be compensates is $j = 2$. The number of gradient lobes consequently is $N = j + 2 = 4$, the polygon order 4, i.e., a square. (B) Compensation of phase shifts due to fourth and lower order motions ($j = 4$). The number of alternating gradient lobes consequently is $N = j + 2 = 6$, and the polygon order is 6.

zeroth, first and second moments vanish if the gradient pulse train takes the form (see Figs. 8 and 9C):

$$G(t) = \begin{cases} \hat{G} & \text{for } 0 \leqslant t < \tau, \\ -\hat{G} & \text{for } \tau \leqslant t < \tau(2+\sqrt{2}), \\ \hat{G} & \text{for } \tau(2+\sqrt{2}) \leqslant t < \tau(3+2\sqrt{2}), \\ -\hat{G} & \text{for } \tau(3+2\sqrt{2}) \leqslant t < \tau(4+2\sqrt{2}), \\ 0 & \text{otherwise.} \end{cases} \tag{A.7}$$

Note that this "acceleration-compensated" gradient pulse train (Fig. 9C) deviates from other sequences known from literature and represented by Figs. 8A and B [17,25–27]. The advantage of the pulse train represented by Eq. (A.7) and Fig. 9C is obvious: It is simpler than those given at Figs. 9A and B with respect to the number of lobes and the variation of the gradient strength.

There is a geometrical rule (the "polygon rule") permitting the design of motion compensating gradient pulse trains of any order. Compare Fig. 10A with Fig. 9C (or Eq. (A.7)) producing velocity compensated phase shifts proportional to accelerations. The durations of the gradient lobes are proportional to the lengths (in the case of the first and the last lobe) and double sums of adjacent line-segments forming a mesh in a rectilinear N-sided polygon, where N is the number of gradient lobes needed. Auxiliary rays originating in point A of the polygon are considered, and adjacent line sections on these rays are added to give the gradient lobe lengths.

Fig. 10B represents the polygon needed for the design of gradient pulse sequence compensating up to the sixth motion order. Six alternating lobes of duration $\tau_1 = |AB| = \tau$, $\tau_2 = |AB| + |AC| = \tau + \sqrt{3}\tau$, $\tau_3 = |AC| + |AD| = \sqrt{3}\tau + 2\tau$, $\tau_4 = |AD| + |AE| = 2\tau + \sqrt{3}\tau$, $\tau_5 = |AE| + |AF| = \sqrt{3}\tau + \tau$, and $\tau_6 = |AF| = \tau$ are suggested in this case.

References

[1] A. Klemm, H.-P. Müller, R. Kimmich, Phys. Rev. E 55 (1997) 4413.
[2] A. Klemm, R. Kimmich, M. Weber, Phys. Rev. E 63 (2001) 041514.
[3] A. Klemm, R. Metzler, R. Kimmich, Phys. Rev. E 62 (2002) 021112.
[4] M. Weber, A. Klemm, R. Kimmich, Phys. Rev. E 66 (2002) 056301.
[5] M. Weber, R. Kimmich, Phys. Rev. E 66 (2002) 026306.
[6] R. Kimmich, Chem. Phys. 284 (2002) 253–285.
[7] M.D. Mantle, A.J. Sederman, Progr. NMR Spectr. 43 (2003) 2.
[8] H.-P. Müller, J. Weis, R. Kimmich, Phys. Rev. E 52 (1995) 5195.
[9] E. Kossel, M. Weber, R. Kimmich, Solid State NMR 25 (2004) 28.
[10] C.L. Dumoulin, R.D. Darrow, D.R. Eisner, M. Tarnawski, K.T. Scott, C.G. Caro, J. Comput. Assist. Tomogr. 18 (1994) 652.
[11] P.T. Callaghan, Principles of Nuclear Magnetic Resonance Microscopy, Clarendon Press, Oxford, NY, 1991.
[12] R. Kimmich, NMR Tomography, Diffusometry, Relaxometry, Springer-Verlag, Berlin, 1997.
[13] D.O. Kuethe, Phys. Rev. A 40 (1989) 4542.
[14] D.O. Kuehte, Phys. Rev. A 44 (1991) 2495.
[15] A.J. Sederman, M.D. Mantle, C. Buckley, L.F. Gladden, J. Magn. Reson. 166 (2004) 182.
[16] B. Blümich, NMR Imaging of Materials, Clarendon Press, Oxford, 2000.
[17] Q.S. Xiang, O. Nalcioglu, IEEE Trans. Med. Imaging MI-6 (1987) 14.
[18] D. Stauffer, A. Aharony, Introduction to Percolation Theory, Taylor & Francis, London, 1992.
[19] Fluent and Gambit User's Guide Manual, Fluent Inc., July 26, 1998.

[20] M. Sahimi, Flow and transport in porous media and fractured rock, VCH, Weinheim, 1995.

[21] A. Bunde, S. Havlin (Eds.), Fractals and Disordered Systems, Springer-Verlag, Berlin, 1996.

[22] H.A. Makse, J.S. Andrade, H.E. Stanley, Phys. Rev. E 61 (2000) 583.

[23] J.L. Duerk, O.L. Simonetti, J. Magn. Reson. Imaging 1 (6) (1991) 643–650.

[24] F. Schmitt, M.K. Stehling, R. Turner, Echo-Planar Imaging, Springer, Berlin, 1998.

[25] M.S. Cohen, Motion Compensation in MR Imaging. Available from http:brainmapping.loni.ucla.edu/BMD_HTML/SharedCode/Motion/motion.html.

[26] E.M. Haacke, Am. J. Roentgenol. 148 (1987) 1251.

[27] D. Nishimura, A. Macovski, J. Pauly, IEEE Trans. Med. Imaging MI-5 (1986) 140–151.

II

B.Buhai, A. Kühnle, and R. Kimmich

NMR Flow Mapping and Computational Fluid Dynamics in Ising-Correlated Percolation Model Objects

New Journal of Physics **7**, p1-21 (2005)

New Journal of Physics
The open-access journal for physics

NMR flow mapping and computational fluid dynamics in Ising-correlated percolation model objects

Bogdan Buhai, Arnold Kühnle and Rainer Kimmich
Sektion Kernresonanzspektroskopie, Universität Ulm, 89069 Ulm, Germany
E-mail: rainer.kimmich@uni-ulm.de

New Journal of Physics **7** (2005) 157
Received 7 April 2005
Published 13 July 2005
Online at http://www.njp.org/
doi:10.1088/1367-2630/7/1/157

Abstract. Water flow through quasi two-dimensional percolation model objects was studied with the aid of NMR velocity and acceleration mapping techniques. The model objects were fabricated based on computer generated templates of Ising-correlated percolation clusters of different growth/nucleation ratios for the occupation of the base lattice sites. The same pore networks were used for computational fluid dynamics simulations of hydrodynamic transport properties including hydrodynamic dispersion of tracer particles. The percolation threshold turned out to be lower than that in the uncorrelated case and adopts a minimum if cluster growth is about 100 times more likely than nucleation of the new clusters. The experimental and simulated flow velocity and acceleration maps coincide in great detail. The data have been analysed in terms of histograms and spatial autocorrelation functions. Furthermore, the travelling time of a tracer particle across percolation clusters was evaluated as a function of the Péclet number.

New Journal of Physics **7** (2005) 157
1367-2630/05/010157+21$30.00
PII: S1367-2630(05)97923-8
© IOP Publishing Ltd and Deutsche Physikalische Gesellschaft

Contents

1. Introduction **2**
2. The Ising-correlated site-percolation model **3**
2.1. Percolation threshold 5
2.2. Characteristic structure parameters of the percolating clusters 6
3. Model objects, instruments and techniques **9**
3.1. Fabrication of model objects 9
3.2. NMR imaging system 10
3.3. CFD software 12
4. Nuclear magnetic resonance imaging experiments **14**
5. Simulations **14**
6. Evaluations of the experimental and simulated maps **15**
6.1. Volume-averaged porosity 15
6.2. Transport backbone 16
6.3. Velocity histograms 16
6.4. Mean tracer travelling time 17
6.5. The spatial velocity autocorrelation function 18
7. Discussion and conclusions **19**
Acknowledgments **20**
References **20**

1. Introduction

The objective of this study is to model the pore network of porous media by ‘Ising-correlated percolation clusters’ in contrast to purely ‘random percolation clusters’. This is an attempt to account for the growth history on which natural porous media are often based. Hydrodynamic transport of fluids through pore networks is of general interest. Apart from the model aspect, we therefore focus on experimental and computational techniques for the elucidation of characteristic transport features.

Modelling of interconnected pore spaces of porous media with respect to fluid transport properties raises many intriguing problems. Discussions can be found in [1]–[6]. Studies published in the literature focus mainly on random percolation clusters [5] and are often based on computer simulations [7]–[13]. Relatively little experimental work has been done so far in this respect. Before this background, the objective of the present study was (i) to examine Ising-correlated percolation clusters generated with the aid of a Monte Carlo method, (ii) to elucidate fluid transport properties with the aid of a computational fluid dynamics (CFD) program and (iii) to compare the numerical results with experimental magnetic resonance imaging (MRI) techniques [14] applied to percolation model objects [15]–[21].

The problems encountered in comparisons of numerical simulations and experimental data in the context of percolation problems pertain (i) to finding appropriate evaluation protocols and characteristic parameters of maps of transport quantities and (ii) in having correlation lengths large enough so that the so-called scaling window applies where fractal power laws can be expected [7]. The latter point means that the porosity should be very close to the percolation threshold which in turn makes experiments difficult to perform.

Nuclear magnetic resonance (NMR) offers a number of imaging variants permitting one to map transport quantities of interest quantitatively. Spin density maps can be used to display interdiffusion of isotopically labelled fluids selectively filled into adjacent compartments of porous model objects [19] (apart from rendering images of fluid-filled pore spaces in general). Velocity (vector) mapping and acceleration (vector) mapping visualize hydrodynamic flow arising from pressure gradients [15]–[18], [22]. Thermal convection flow can be examined likewise with the same sort of experimental protocol [21]. Temperature distributions due to thermal convection and conduction in porous materials can indirectly be probed by calibrating temperature-sensitive quantities such as the spin–lattice relaxation time accordingly [21]. Hydrodynamic dispersion coefficients characterizing the interplay between (incoherent) self-diffusion and (coherent) flow can be studied using pulsed field gradient spin echo techniques [23]. A further method of interest is electric current density mapping of ionic currents in electrolyte solutions filled into a pore space in the presence of an electrostatic potential gradient [20]. Recent reviews on the perspectives of the magnetic resonance methodology for studies of porous media can be found in [24]–[26]. The next problem refers to the evaluation of experimental or simulated maps of transport quantities. Evaluated relations permitting the quantitative determination of characteristic parameters for the percolation properties are volume-averaged measurands (pore space density, velocity, acceleration, current density etc.) as a function of the porosity, histograms and spatial correlation functions. In particular, if the data reveal scaling law properties, a number of well-defined parameters can be evaluated from such secondary plots. Examples are the fractal dimension d_f, the correlation length ξ and the percolation probability P_∞ characterizing the dependence of volume-averaged quantities on the porosity [5]. Correlation lengths can be evaluated from spatial correlation functions. Histograms permit one to identify different processes occurring on different scales of the measurand. If a description based on scaling laws applies, the determination of power law exponents can be of particular interest for theoretical considerations [4, 5].

The strategy we pursue in the present study of fluid flow through correlated percolation clusters resembles the modus operandi of our previous investigations of random percolation clusters which were of ‘random site’, ‘swiss cheese’ and ‘inverse swiss cheese’ type [15]–[23]. The fabrication of well-defined model objects based on computer-generated templates provides not only the samples for informative NMR imaging experiments but also the complete datasets describing the pore spaces of these samples in all details. On the basis of these datasets, reliable CFD simulations using finite element method (FEM) or finite volume method (FVM) software packages can be carried out for comparison with experimental findings.

The advantages of this sort of system are obvious: in principle, the pore space is of sufficient complexity to represent natural or technical pore networks of interest. Since the model objects are based on computer-generated clusters, the pore spaces are well defined so that point by point datasets describing the pore space are available. Since these datasets are known, they can directly be fed into finite-element or finite-volume CFD programs in order to simulate transport properties. The percolation model objects are thus taken as a transport paradigm for any pore network of major complexity.

2. The Ising-correlated site-percolation model

The correlated site-percolation model considered in the present study is based on the Ising model in two dimensions [27]. A quadratic base lattice is assumed. Neighbouring sites form a pore if

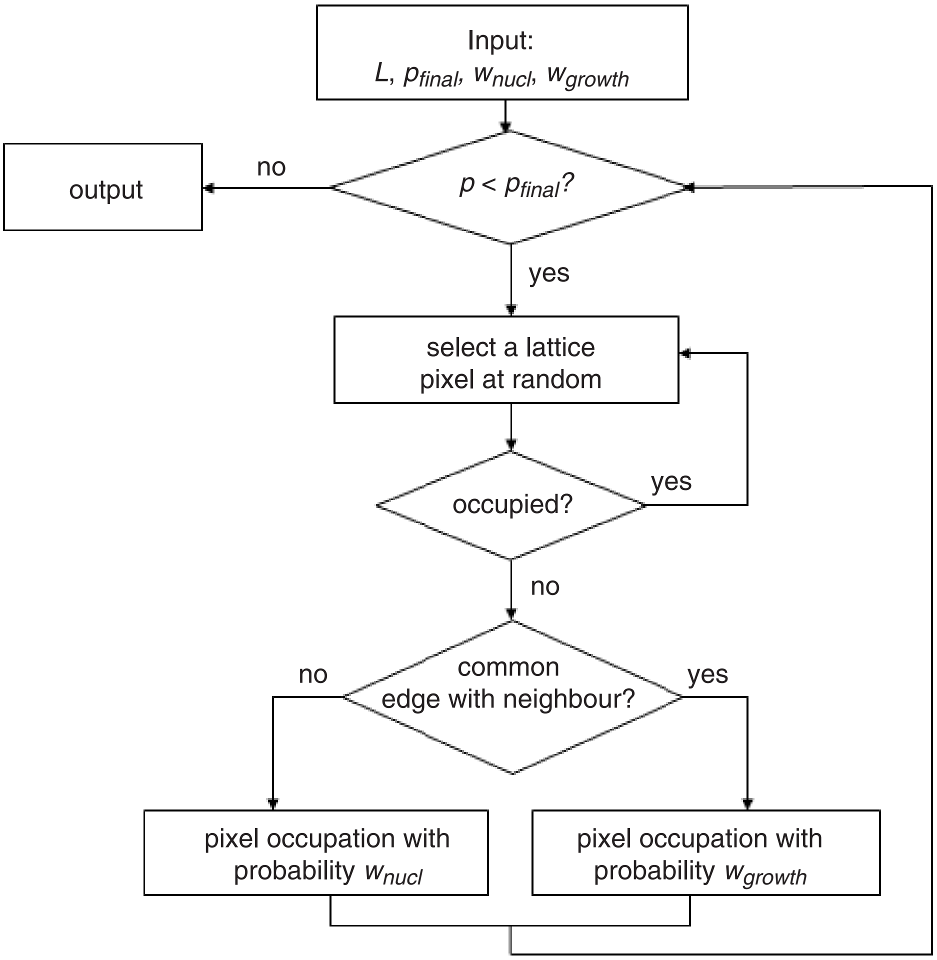
Input:
L, pfinal, wnucl, wgrowth
p < pfinal?
no
output
yes
select a lattice pixel at random
occupied?
yes
no
common edge with neighbour?
no
yes
pixel occupation with probability wnucl
pixel occupation with probability wgrowth

Figure 1. Flow chart of the algorithm used for the generation of Ising-correlated percolation clusters on square matrices with $L \times L$ sites.

the quadratic pixels attributed to them share a common edge. The lattice sites are occupied with a random-number algorithm until the desired porosity is reached. The occupation probability of an unoccupied site depends on whether any of the neighbour sites is occupied or not. That is, nucleation (i.e. there are no occupied neighbour sites) is distinguished from growth (i.e. there is at least one occupied neighbour site) occupation probability. If both occupation probabilities are equal, the result will be a random site-percolation cluster. If the growth occupation probability is larger than the nucleation occupation probability, an 'Ising-correlated percolation cluster' results.

The cluster-generating algorithm is specified in figure 1. The program is initiated by defining a square matrix of $L \times L$ lattice sites, the porosity to be finally reached, p_{final}, the nucleation probability w_{nucl} and the growth probability w_{growth}. The pixel matrix is then occupied in an iterative way until the desired porosity is reached. In each iteration step, a pixel is selected randomly. If it is still unoccupied, the program continues to check for any occupied neighbour pixels. Depending on whether there is an occupied neighbour or not, the pixel is occupied with the growth or nucleation probability respectively. The ratio between the two occupation probabilities will be termed the 'growth–nucleation quotient',

$$f_c = \frac{w_{growth}}{w_{nucl}} \geqslant 1.$$

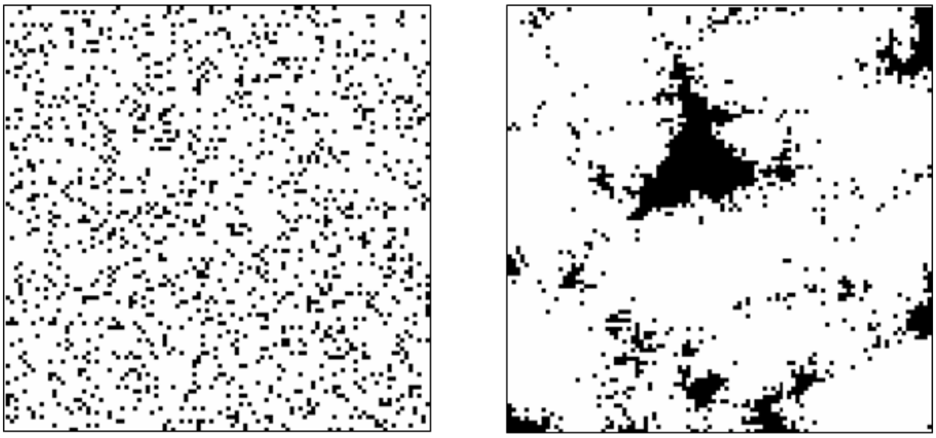

$f_c = 1$; $p_{final} = 0.864$ $f_c = 10{,}000$; $p_{final} = 0.864$

Figure 2. Typical example of an Ising-correlated cluster with high (right) growth–nucleation quotient in comparison to a random site-percolation cluster (left). 'Black' means 'unoccupied', that is the matrix. White pixels represent the pore space. The base lattice size was 100 × 100 sites.

A growth–nucleation quotient $f_c = 1$ means complete randomness of the pixel occupation. In the opposite limit, $f_c \to \infty$, the correlation of occupied pixels is complete so that just one cluster comprising all occupied pixels exists.

In figure 2, a typical example of an Ising-correlated percolation cluster is juxtaposed to a random site-percolation network generated for the same porosity with the aid of the algorithm given in figure 1. The concentration of the occupied pixels in compact clusters is characteristic for large growth–nucleation quotients.

The examination of Ising-correlated percolation clusters discussed in the following refers to four different square base lattices ($L \times L = 50 \times 50$; 100×100; 200×200; 500×500) in order to identify size-dependent effects. For each of these base lattices 100 independent clusters were generated. The parameters evaluated from these clusters were averaged accordingly. Different final porosities were investigated and the growth–nucleation quotient was varied in 10 steps in the range $3.2 \geqslant f_c \geqslant 100\,000$. The total number of clusters considered in this study was 12 000 in various combinations of the cluster-defining parameters. Three of the clusters were examined in more details with the aid of CFD simulations and, after the fabrication of the corresponding model objects [15]–[21], with MRI experiments [14]. It is needless to say that these samples are based on 'infinite' clusters connecting two opposite sides of a square matrix. Figure 3 shows an example.

2.1. Percolation threshold

The percolation threshold [5] was determined as a function of the growth–nucleation quotient on the basis of 100 independent networks generated in each case for a given parameter triple L, p_{final}, f_c. The number of percolation networks containing an 'infinite' cluster, $n_{\text{'infinite'}}$, the so-called 'percolating' or 'sample spanning' cluster, was counted and related to the number of networks without percolating cluster, n_{finite}. The ratio $n_{\text{finite}}/n_{\text{'infinite'}}$ was then plotted versus

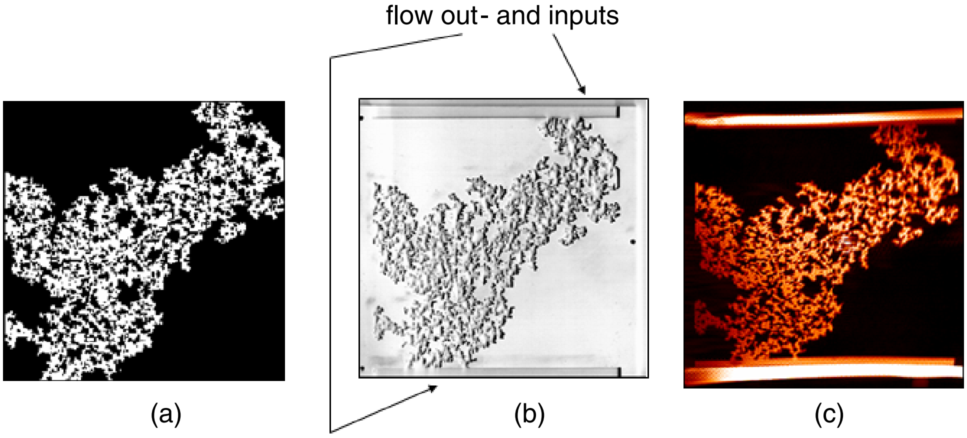

Figure 3. Typical example of an Ising-correlated percolation cluster examined in this study with the aid of CFD and MRI techniques. The parameters are $L \times L = 200 \times 200$ for the base lattice size, $f_c = 10$ for the growth–nucleation quotient and $p_{final} = 0.59$ for the porosity. The clusters shown are ‘sample spanning’. (a) Computer generated percolating cluster (white = pore space) with all isolated clusters eliminated. (b) Photograph of an element of the quasi-two-dimensional model object milled into a polystyrene matrix using the cluster shown in (a) as a template. The size is $10 \times 10\,\mathrm{cm}^2$. The final sample consisted of a stack of nine identical elements into which copper sulphate doped water was filled (see figure 7 and the description in section 3.1). (c) Experimental spin density map of water filled into the pore space. The pore space is rendered in light colours. The matrix does not contribute to the spin echo signals recorded in our experiments.

the porosity p_{final}. An example is shown in figure 4. The percolation threshold is defined as the position where the ratio $n_{\text{finite}}/n_{\text{‘infinite’}}$ takes the value 0.5.

Figure 5 shows the threshold values as a function of the growth–nucleation quotient. The values tend to be lower than in the uncorrelated case ($p_c^{\text{uncorr}} = 0.592746$ for random site percolation on a square base lattice; compare also [5, 28, 29]). Interestingly, a minimum appears in the range $30 < f_c < 320$. The minimum value is between 0.51 and 0.52 independent of the base matrix size as far as the investigation of this study is concerned. The literature value for the random site-percolation threshold in two dimensions, i.e. in the limit when f_c approaches the value 1, is reproduced by the analysis used in the present study with an accuracy reasonable in the light of the small base lattice sizes to which our study was restricted. Note that finite percolation networks theoretically have thresholds somewhat larger than infinite ones [5].

2.2. *Characteristic structure parameters of the percolating clusters*

The correlation length has been evaluated from the volume-averaged porosity as a function of the probe volume radius [18]. For the determination of the volume-averaged porosity we have employed the so-called sandbox method [4, 15]. The volume-averaged porosity is defined by

$$\rho_V(r) = \frac{1}{N_p(r)} \sum_{k=1}^{N_p(r)} \frac{1}{N_V} \sum_{j=1}^{N_v} \rho(\vec{r}_j), \qquad (2)$$

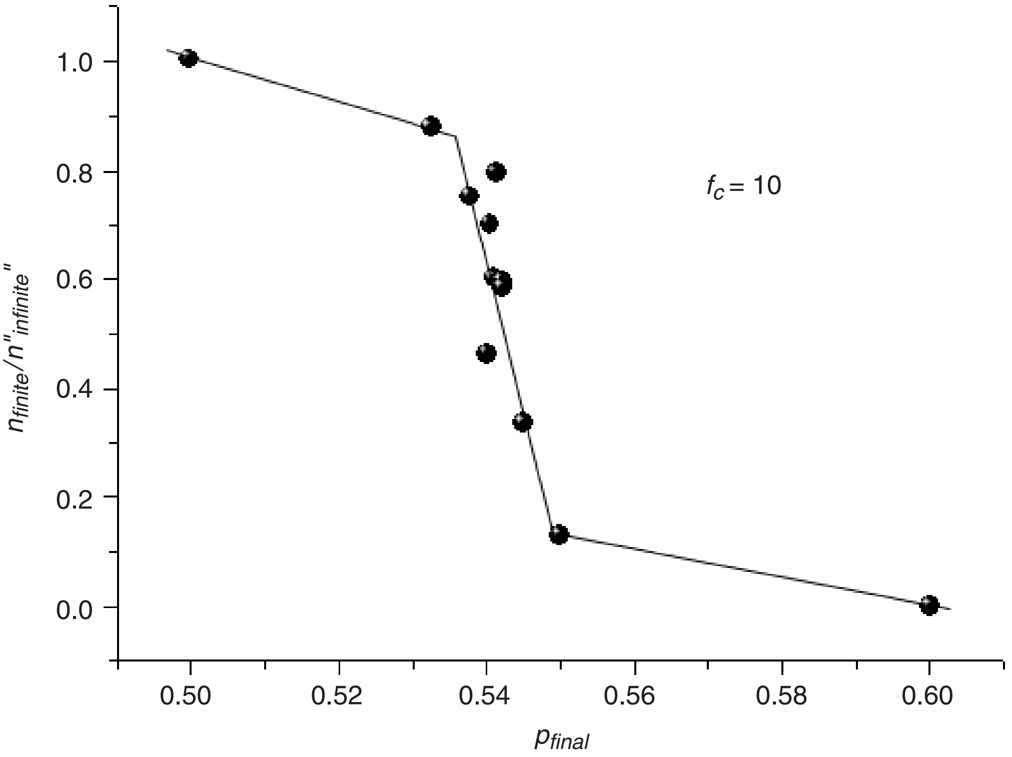

Figure 4. Ratio of the numbers of networks without and with percolating (= sample-spanning) clusters, $n_{\mathrm{finite}}/n_{\text{‘infinite’}}$, versus the porosity p_{final} for a growth–nucleation quotient $f_c = 10$ and a square base lattice size $L \times L = 200 \times 200$. Each of the data points refers to a set of 100 independently generated networks according to the algorithm shown in figure 1. The lines indicate the crossover at the percolation threshold which is defined for $n_{\mathrm{finite}}/n_{\text{‘infinite’}} = 0.5$.

where $r \leqslant |\vec{r}_k - \vec{r}_j|$. The ‘pore space density’ ρ can take two values according to

$$\rho(r_j) = \begin{cases} 0 & \text{(pixel not occupied} \Rightarrow \text{matrix pixel),} \\ 1 & \text{(pixel occupied} \Rightarrow \text{pore).} \end{cases} \tag{3}$$

Equation (2) means that disk-shaped probe areas (‘probe volumes’) of radius r are centred in positions $\vec{r}_k$ within the pore space. That is, $\vec{r}_k$ must be the position of an ‘occupied’ pixel (‘voxels’). $N_p(r)$ is the number of probe areas of a given radius r that can be placed with centres at pixels in the pore space. The probe areas must not exceed the sample under consideration, of course. N_V is the number of pore space pixels within a given probe area. So, we first average the ‘pore space density’ ρ over the ‘volume’ of a given probe area of radius r (sum index j) and then take the arithmetic mean of the results for all possible probe areas of the same radius (sum index k). The volume-averaged porosity as a function of the probe area radius decays from the value 1 at a radius corresponding to a single lattice constant to a terminal value P_∞, the ‘percolation probability’ at radii much larger than the correlation length, $r \gg \xi$. For ‘fractals’, the initial decay

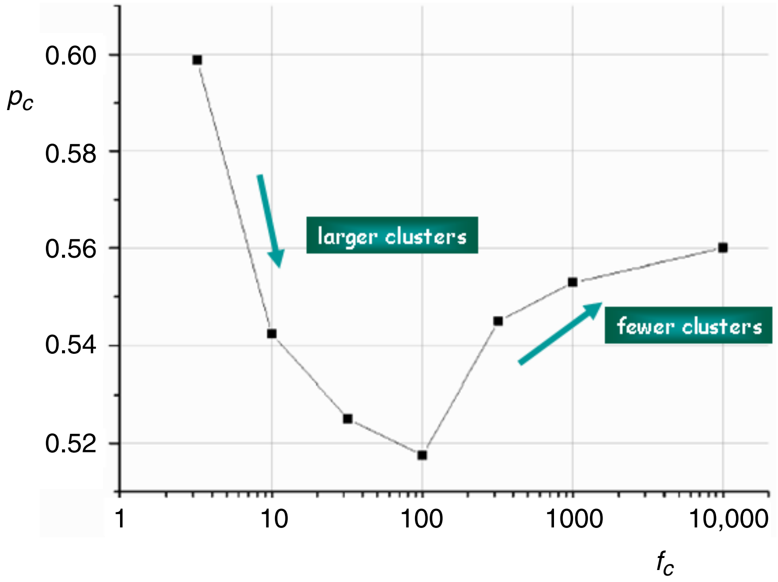

Figure 5. Percolation threshold p_c for the Ising-correlated site percolation model versus the growth–nucleation quotient f_c for a base lattice size $L \times L = 200 \times 200$ sites. A minimum is reached in the interval $30 < f_c < 320$.

can be described by a power law according to

$$\rho_V(r) \approx \begin{cases} r^{d_f - d_E}, & b < r \ll \xi, \\ P_\infty, & r \gg \xi, \end{cases} \tag{4}$$

where d_f is the fractal dimension, P_∞ is the percolation probability defined as the probability that a site belongs to the percolating cluster traversing the whole sample, ξ is the correlation length, b is the base lattice constant ($\approx$0.4 mm for the present objects) and d_E is the Euclidean dimension ($=$2 in the present case). Double logarithmic plots of $\rho_V(r)$ can thus be evaluated with respect to the three characteristic parameters d_f, P_∞ and ξ.

Figure 6 shows the correlation length as a function of the growth–nucleation quotient for a relatively large system based on an 500×500 site lattice. Within the range of the examined growth–nucleation quotient, the data for a $L \times L$ site system can be described by the power law

$$\xi = \gamma b f_c^\beta \tag{5}$$

provided that $b \ll \xi \ll L$. The parameters $\beta \approx 0.32 \pm 0.04$ and $\gamma \approx 7.75 \pm 0.06$ are constants. The correlation length 'increases' with the growth–nucleation quotient. There is no or only a negligible dependence of the correlation length on the porosity in the investigated range. The reason is that the number of clusters realized in the generation process depends on the nucleation probability but not on the porosity. If the nucleation probability is low, clusters once nucleated will preferably grow at the expense of the nucleation of new clusters, so that the correlation length becomes larger with lower nucleation probabilities.

On the other hand, the power law given in equation (5) is only valid as long as the correlation length is much shorter than the system size. Otherwise a 'cut-off' of the correlation length versus growth–nucleation quotient curve is observed. For clusters on a base lattice of size

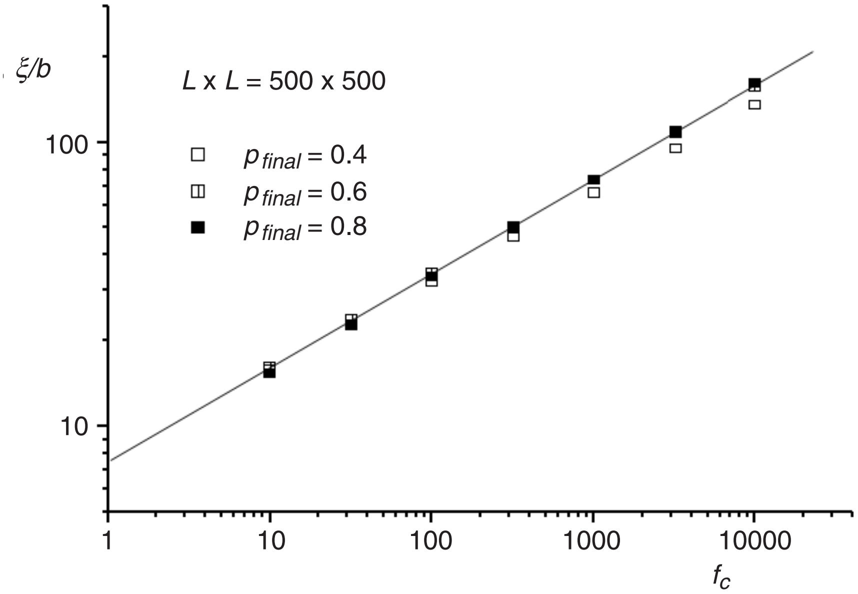

Figure 6. Correlation length ξ (in units of the base lattice constant b), as a function of the growth–nucleation quotient, f_c, for percolating clusters of different porosity, p_{final}, on a square base lattice of size $L \times L = 500 \times 500$ pixels. The data have been evaluated from the total simulated percolation networks including isolated clusters. The straight line represents the power law given in equation (5).

$L \times L = 50 \times 50$, for instance, we found a maximum correlation length of about $25b$ reached at a growth–nucleation quotient of about 3000. Beyond this growth–nucleation quotient value, the condition $b \ll \xi \ll L$ is violated and the evaluated correlation length does not increase any further.

3. Model objects, instruments and techniques

3.1. Fabrication of model objects

The templates for the model objects used for the MRI experiments were generated with the algorithm given in figure 1 using the IDL5.3 software package (Interactive Data Language based on a C++ platform). Since only the percolating (sample spanning) cluster is relevant for transport, all isolated clusters were removed (compare figure 3(a)). The porosity is nevertheless specified by the value p_{final} anticipated in the computer generation process (see figure 1). A comparison of the porosities p_{final} of the whole percolation networks with the porosities effective for the sample-spanning cluster alone, $p_{cluster}$ is given in table 1.

The datasets resulting from the cluster-generation program, figure 1, were fed into a digital circuit board plotter (LPKF, 'Leiterplatten-Konturfräsen') used for milling the pore space into 3 mm thick polystyrene plates. The milling depth was 2 mm and the location resolution of the milling tool was 6 μm (see figure (3b)). Porous model objects have been fabricated for growth–nucleation quotients 10, 100 and 500. The base lattice size is $L \times L = 200 \times 200$ sites in all cases. The resulting porosities are $p_{final} = 0.59, 0.57$ and 0.60 respectively.

Table 1. Comparison of the porosities of the whole percolation networks, p_{final}, as anticipated in the algorithm shown in figure 1, and the porosities effective for the sample spanning cluster alone, $p_{cluster}$. The data refer to a base lattice size of 200 × 200 sites.

	$f_c = 10$	$f_c = 100$	$f_c = 500$	$f_c = 1000$
p_{final}	0.590	0.570	0.599	0.600
p_{cluster}	0.280	0.436	0.558	0.561

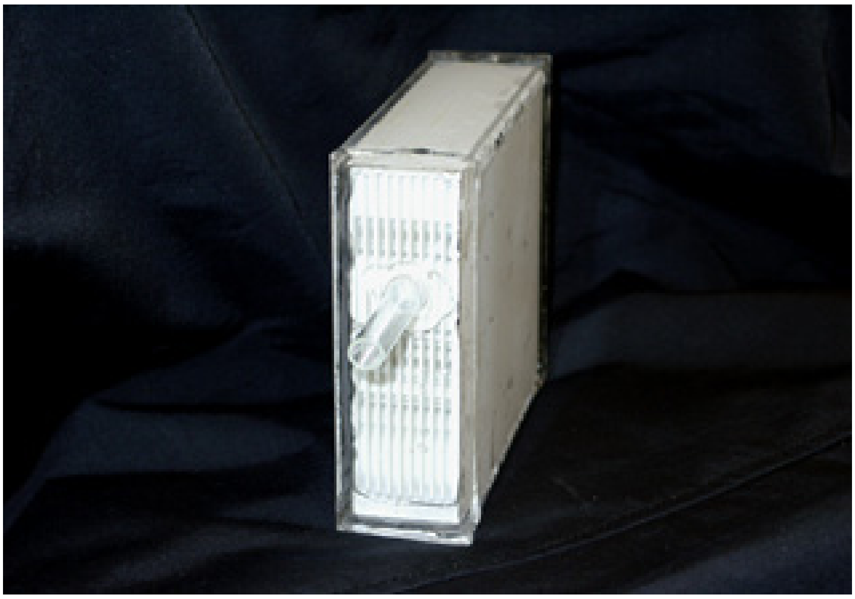

Figure 7. Photograph of a model object consisting of a stack of nine identical quasi-two-dimensional percolation cluster plates of the sort shown in figure 3(b). A flow input or output spout is visible.

The final, quasi-two-dimensional model objects are composed of stacks of nine identical plates structured in this way in order to improve the signal-to-noise ratio of the NMR experiments. The stacks have been incorporated in plexiglass containers with liquid inputs and outputs (see figure 7). The pore space was filled with demineralized water doped with $CuSO_4$ in order to reduce the spin–lattice relaxation time T_1 to about 500 ms. A typical spin density map recorded with one of the samples is shown in figure 3(c). Note that the matrix material and the container do not provide liquid-state NMR signals and can therefore easily be discriminated from the liquid.

3.2. NMR imaging system

Spin density, velocity and acceleration mapping experiments were performed with a home made NMR imaging system using a Bruker 4.7 T magnet with a 40 cm horizontal room temperature bore. All NMR signals refer to proton resonance at 200 MHz. The probe head was a Bruker birdcage resonator with an inner diameter of 195 mm. The maximum field gradient

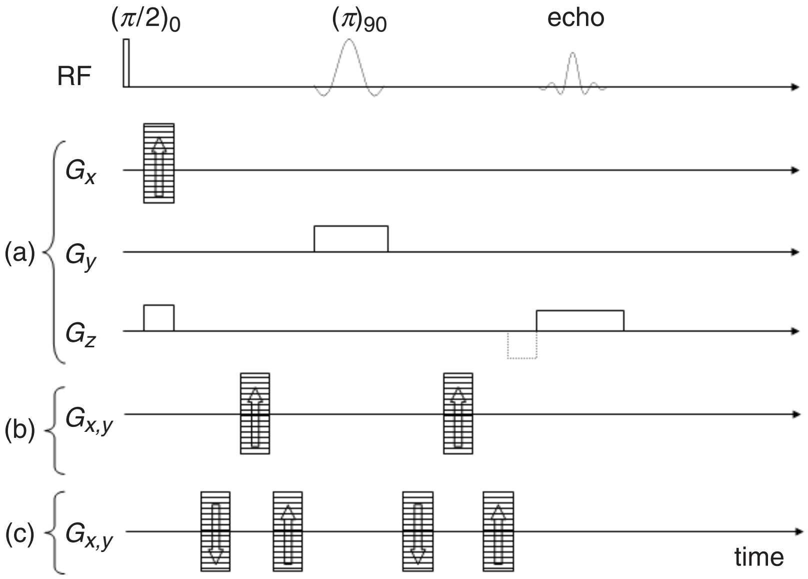

Figure 8. RF and field gradient pulse sequence used for NMR spin density (trains a), velocity (trains a plus b) and acceleration (trains a plus c) mapping experiments with quasi-two-dimensional objects in the x–y plane. A standard Hahn spin echo imaging sequence is used in combination with one (b) or two (c) pairs of gradient pulses (see [14, 21]). The arrows indicate the mutual polarity of the gradients which are incremented in nine steps in a corresponding series of transients. The ramps of the gradient pulses are not shown for simplicity. The slice-selective π pulse ensures that no signals from the fringe areas above and below the objects are recorded. Instead of the positive compensation gradient pulse for frequency encoding along the z-direction, a negative gradient lobe (dotted line) just before the read-out gradient may be preferable in order to avoid motion artifacts in the imaging part of the pulse sequences. To acquire the velocity or acceleration vector field, all components must be probed one by one. For quasi-two-dimensional objects of the present investigation, the dataset acquired in this way consists of two four-dimensional matrices. Fourier transforms in all four dimensions lead to conjugated datasets providing the two in-plane velocity or acceleration vector components. In the velocity or acceleration maps, the magnitudes $v = \sqrt{v_x^2 + v_y^2}$ or $a = \sqrt{a_x^2 + a_y^2}$ are plotted where the flow directions are perpendicular to the z-direction.

was 50 mT m^{-1} in all three space directions. The experimental spin density maps reproduce the computer-generated template structure reliably (see figure 3) although the quasi-two-dimensional model objects are subject to friction at the bottom and top surfaces whereas the simulations refer to two dimensions in the proper sense. This coincidence demonstrates the quality of both the fabrication and NMR imaging processes.

Spin density maps of the water-filled pore spaces were recorded with the aid of the radio frequency (RF) and field-gradient pulse sequence shown in figure 8(a) [14]. The maps were rendered by processing the raw data by two-dimensional Fourier transformation. Due to

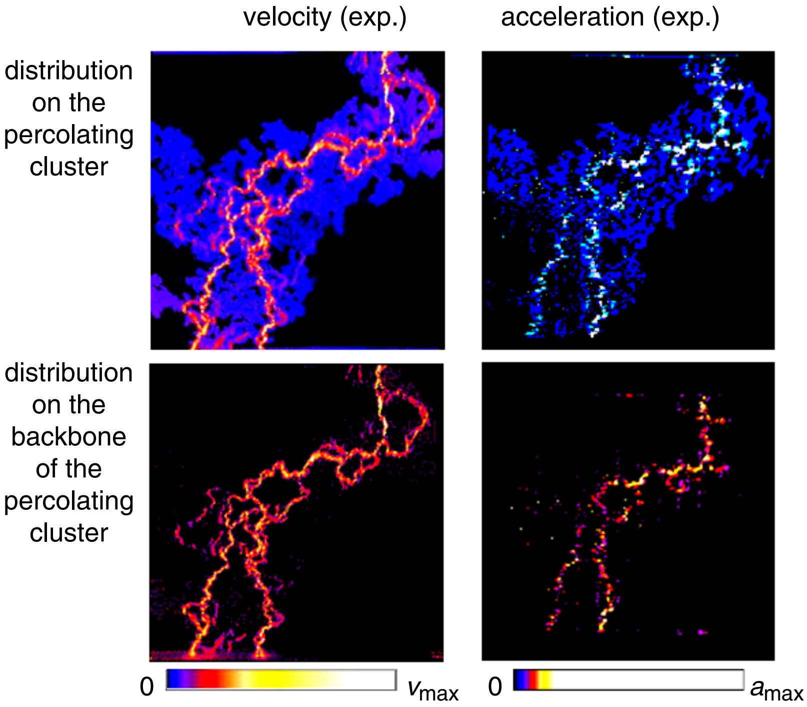
velocity (exp.)
acceleration (exp.)
distribution on the percolating cluster
distribution on the backbone of the percolating cluster
0
v_{max}
0
a_{max}

Figure 9. Typical maps of the velocity (top left) and acceleration (top right) magnitudes recorded in the percolation cluster model object shown in figure 3(b) ($f_c = 10$). The maps were recorded with the aid of the pulse sequences given in figure 8 ((a) + (b)) for the velocity and ((a) + (c)) for the acceleration. The maximum velocity and acceleration magnitudes were $v_{\mathrm{max}} = 3.6\,\mathrm{mm\,s^{-1}}$ and $\alpha_{\mathrm{max}} = 0.5\mathrm{mm^2\,s^{-1}}$, respectively. The bottom row shows the distributions on the corresponding 'percolation backbones' where all pixels with velocities or accelerations below the noise level have been blackened [18]. Flow input and output are on the top and on the bottom of the clusters.

field-of-view limitations, the largest objects that can be mapped with our system are restricted to a base lattice size of 200 × 200 or an object size of $10 \times 10\,\mathrm{cm}^2$.

For the flow experiments, a stationary pressure gradient was exerted on the fluid-filled pore spaces of the model objects by connecting a reservoir 1.5 m above the sample level. The reservoir was permanently refilled with the aid of a peristaltic pump. The total flow rate was in the range 0.1–$0.3\,\mathrm{ml\,s^{-1}}$.

Phase encoding of flow velocity or acceleration components was achieved by applying additionally the field gradient pulse sequences shown in parts (b) and (c) of figure 8, respectively. Detailed descriptions of velocity and acceleration NMR measuring techniques can be found in [14, 21, 30]. The digital space resolution was better than 300 μm in all three space directions. All experiments were carried out at room temperature. Typical velocity and acceleration maps recorded with the object shown in figures 3(b) or 7 are rendered in figures 9 and 10(c).

3.3. CFD software

All flow experiments were accompanied by CFD simulations based on the same pore space structures as in the experiments. The simulations were performed on a PC using the software

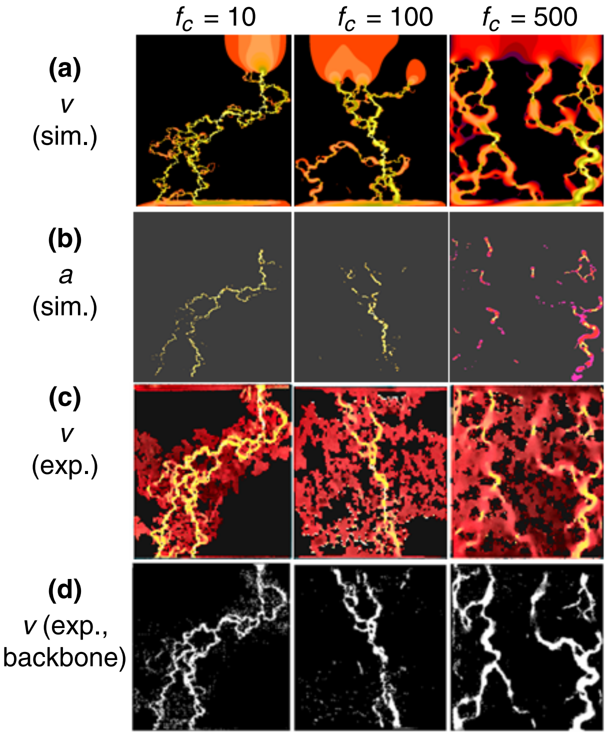

Figure 10. Simulated and measured maps of the velocity and acceleration magnitudes in three Ising-correlated percolation clusters of different growth–nucleation quotient. The transport pathways are highlighted in light colours or white. With the exception of the background of the experimental maps in (c), the matrix structure is not shown for clarity. (a) CFD simulations of the spatial velocity distribution. The inflow and outflow patterns at the top and bottom respectively, are partly visible. (b) CFD simulations of the spatial acceleration distribution. (c) Experimental velocity maps measured in quasi-two-dimensional model objects of the three percolation clusters. The NMR pulse sequence shown in figure 8 ((a) + (b)) was employed. The maximum velocity was about 10 mm s^{-1}. The pore space structures are shown as reddish brown background contrast whereas the matrix is rendered in black.(d) Velocity distributions on the backbones of the 'infinite' (sample spanning) clusters derived from the experimental velocity maps by blackening all pixels where the velocity is below the noise level [18].

package FLUENT 5.5.14 which employs the FVM. Each matrix point was represented by 5 × 5 'knots' or 'quad elements'. The convergence criterion was set to a residuum of 10^{-5}. Obstacles in the pore space are defined by vanishing flow velocity at the corresponding knots. In this way, periodic meshing was possible so that the same resolution, 80 × 80 μm, applies to all flow paths. The same parameters (fluid viscosity, pressure difference exerted on the object, object size etc.) were assumed as in the NMR experiments. The velocity or acceleration maps were rendered with the aid of the software package IDL 5.3. Typical velocity and acceleration maps are shown in figure 10.

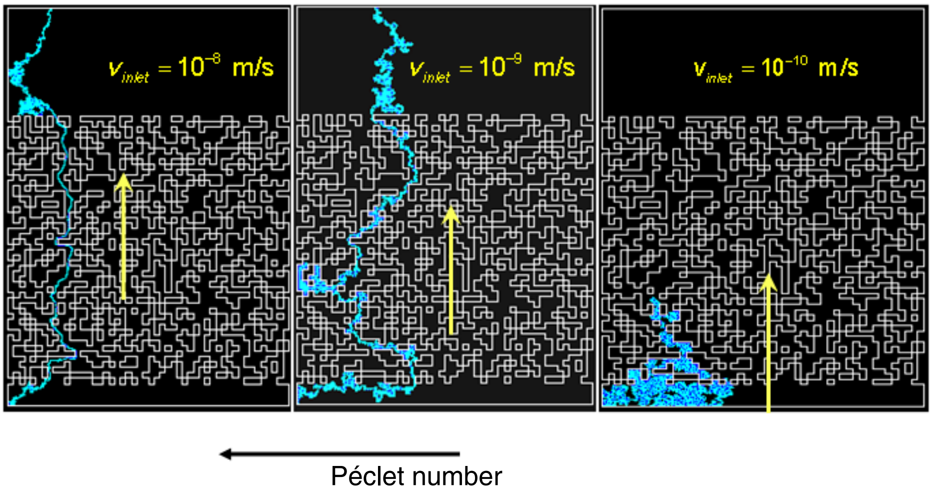
$v_{inlet} = 10^{-8}$ m/s
$v_{inlet} = 10^{-9}$ m/s
$v_{inlet} = 10^{-10}$ m/s
Péclet number

Figure 11. Hydrodynamic dispersion of a neutral tracer in a flow field percolating in an Ising-correlated site-percolation cluster ($f_c = 10$; the porosities are given in table 1) as a function of the Péclet number $Pe = v\xi/D$, that is the inlet velocity. The particle trajectories are indicated in light blue. The arrows indicate the main flow direction. At the lowest Péclet number, $Pe = 0.09$, diffusion strongly determines the tracer trajectory in contrast to the highest value, $Pe = 40.35$.

4. Nuclear magnetic resonance imaging experiments

The experiments were performed under conditions of locally stationary velocities and accelerations. Velocity and acceleration vectors of the spin bearing particles were recorded at certain positions (voxels) rather than for a certain tracer particle experiencing varying velocities and accelerations when travelling through different voxels. Stationary flow patterns and pressure gradients stipulate locally stationary velocities and accelerations.

Figures 9 and 10 show examples of experimental maps of the velocity or acceleration magnitudes. The flow patterns are reasonably well reproduced by the CFD simulations displayed in figure 10. Note the discontinuous distributions of the acceleration along the flow pathways (figure 9, right column), whereas the velocity is represented by continuous patterns (figure 9, left column).

5. Simulations

Maps of the velocity magnitude, $v = \sqrt{v_x^2 + v_y^2}$, in the two-dimensional percolation clusters were obtained as described previously [18] by solving the conservation equations for mass and momentum (see [31]) on a discrete domain. Examples are shown in figure 10(a).

Hydrodynamic dispersion of a neutral tracer particle diffusing in the streaming fluid was simulated by taking the equation of energy into account. Typical trajectories are shown in figure 11. The transport of the tracer depends on the macroscopic Péclet number [2] defined by

$$Pe = v\,l/D, \tag{6}$$

where v is the fluid velocity, D is the molecular diffusivity of the tracer and l is a characteristic length of the flow field. In site-percolation models, l can be identified with the correlation length ξ.

That is

$$Pe = v\xi/D. \tag{7}$$

Here we anticipate that the flow velocity is constant over the correlation length for simplicity.

In the absence of flow, the tracer executes a random walk of step size $s = b/10$, where b represents the minimum dimension of the pore size which is 400 μm in our case. The tracer trajectory also depends on where it is launched into the flowing fluid. An example based on different Péclet numbers is shown in figure 11. For the lowest Péclet number, that is $Pe = 0.09$, diffusion strongly determines the tracer trajectory. On the other hand, if the Péclet number takes a high value such as $Pe = 40.35$, flow convection dominates the dispersion almost completely.

Maps of the acceleration magnitude, $a = \sqrt{a_x^2 + a_y^2}$, cannot be simulated directly with the FLUENT 5.5.14 software package. However, velocity maps obtained in the usual way can be processed correspondingly using the IDL 5.3 software mentioned above. Anticipating an Eulerian approach, the two-dimensional velocity vector field $\vec{v} = (v_x(x, y, t), v_y(x, y, t))$ can be differentiated according to

$$a_x = a_x(x, y) = \frac{\mathrm{d}v_x}{\mathrm{d}t} = \frac{\partial v_x}{\partial x}\frac{\partial x}{\partial t} + \frac{\partial v_x}{\partial y}\frac{\partial y}{\partial t} = \frac{\partial v_x}{\partial x}v_x + \frac{\partial v_x}{\partial y}v_y, \tag{8}$$

$$a_y = a_y(x, y) = \frac{\mathrm{d}v_y}{\mathrm{d}t} = \frac{\partial v_y}{\partial x}\frac{\partial x}{\partial t} + \frac{\partial v_y}{\partial y}\frac{\partial y}{\partial t} = \frac{\partial v_y}{\partial x}v_x + \frac{\partial v_y}{\partial y}v_y. \tag{9}$$

Note that the acceleration components given in the equations (8) and (9) depend on the (voxel) position but not on time since all velocity components are assumed to be locally stationary and merely change from position to position. Examples are shown in figure 10(b).

6. Evaluations of the experimental and simulated maps

Maps of the (water) spin density, velocity magnitude and acceleration magnitude were rendered for the three examples of Ising-correlated percolation clusters as described above both with NMR experiments and computer simulations. In each case, the experimental and simulated patterns reproduce each other reliably. Figures 9 and 10 show typical velocity and acceleration maps obtained from NMR experiments and CFD simulations respectively. The velocity maps indicate pathways of a more continuous character, whereas the acceleration strongly fluctuates along the flow channels. That is, the acceleration is only in certain voxels large enough to be detected above the noise level of the experimental set-up. These sections correspond to bottlenecks and strongly curved pathways where flow is strongly accelerated or decelerated.

6.1. Volume-averaged porosity

The volume-averaged porosity defined by equation (2) was evaluated from water spin density maps. An example is shown in figure 3(c). Evaluations of the fractal dimension according to equation (4) lead to values of $d_f \approx 1.75$ without significant variation for growth–nucleation quotients in the range $10 < f_c < 1000$. This value differs from the fractal dimension of uncorrelated clusters of the same porosity $d_f \approx 1.86$ evaluated from simulations or $d_f \approx 1.83$ evaluated from experiments by less than 6%, that is, within the error limits.

Similar evaluations for volume-averaged velocity and volume-averaged acceleration defined analogous to equation (2) were suggested in [18]. A power-law decay to a long-distance plateau similar to equation (4) can however be stated only for low correlations corresponding to $f_c < 10$.

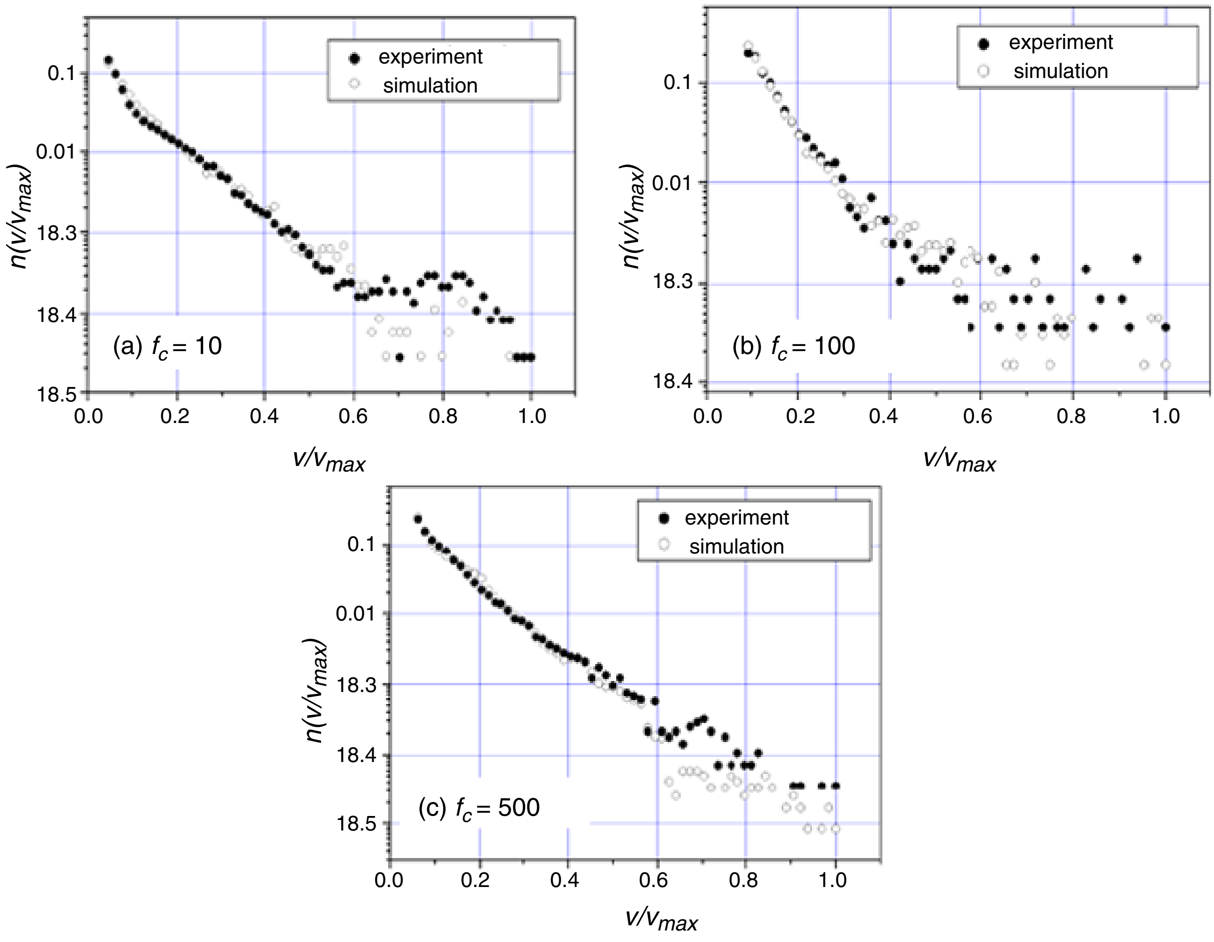

Figure 12. Comparison between histograms of simulated and experimental velocity magnitude maps for (a) $f_c = 10$, (b) $f_c = 100$ and (c) $f_c = 500$. The maps are shown in Figure 10. The porosities are given in table 1.

That is, this sort of behaviour appears to be valid only for clusters approaching the entirely random limit.

6.2. Transport backbone

Transport backbones can be evaluated from the maps by blackening all voxels with velocities below the noise level. The latter was determined in stagnant zones where there is no flow at all. The procedure is described in [15]. Typical maps of backbones are shown in figures 9 and 10. Taking the corresponding pixel subset of the spin-density maps, one can evaluate the fractal dimension of the backbone. The value, $d_f^{bb} \approx 1.25$, is much smaller than that of the whole percolation cluster [18] as it must be since the pore space contributing to transport is only a small fraction of the total percolation cluster.

6.3. Velocity histograms

Figure 12 shows typical histograms evaluated from simulated and experimental velocity maps. The data points obtained from experimental and simulated maps practically coincide within the

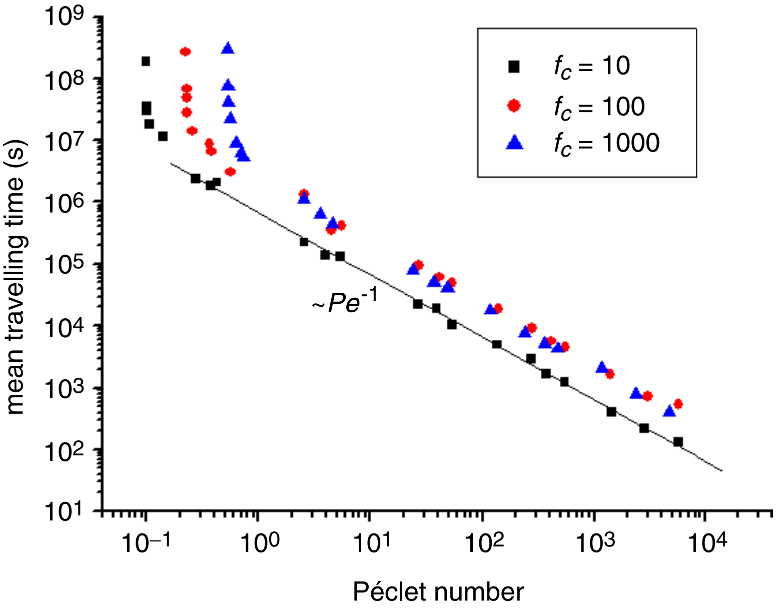

Figure 13. Total travelling time across the sample experienced by a neutral tracer as a function of the Péclet number for three different growth–nucleation quotients (squares represent $f_c = 10$, circles $f_c = 100$ and triangles $f_c = 1000$). The data were evaluated from CFD simulations for the porosities given in table 1.

evaluation error. The characteristic features reported previously for convection in uncorrelated percolation clusters [21] show closely up again and appear to be scarcely influenced by the growth–nucleation quotient. Similar to the cases described in [21], an exponential variation of the velocity distribution can be stated. However, unlike the thermal convection case in uncorrelated clusters, there is now some weak tendency towards bi- or multi-exponential decays (see figure 12(a), for instance) which is assumed to reflect the wide range in the size of the flow obstacles caused by the Ising-correlation.

6.4. Mean tracer travelling time

Figure 13 shows a plot of the mean travelling time of a neutral tracer across the percolation cluster (compare figure 11) versus the Péclet number for various growth–nucleation quotients. The data above $Pe = 1$ are compatible with

$$\tau_t \propto (Pe)^{-1} \quad \text{for } 10^0 < Pe < 10^4, \tag{10}$$

as expected for the limit where displacements by hydrodynamic flow dominate and where an effectively constant displacement rate along the net transport direction occurs on a length scale beyond the correlation length of the system. Below $Pe \approx 1$, the steep decay of the mean travelling time with the Péclet number indicates the decreasing dominance of Brownian motions and the increasing influence of coherent flow.

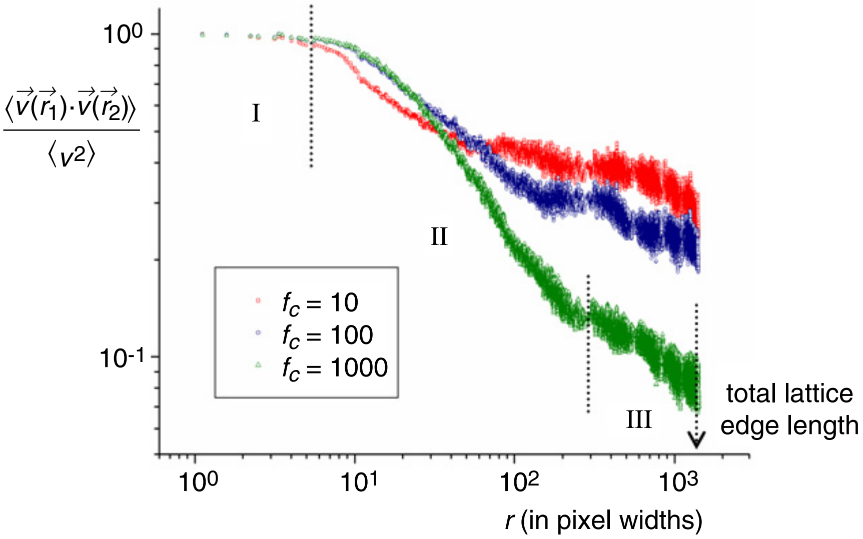

Figure 14. Typical spatial velocity autocorrelation functions (equation (11)) evaluated from simulated velocity maps for percolation networks ($p_{final} = 0.6$) with three different growth–nucleation quotients. The data refer to the total network including isolated clusters. The distance $r = |\vec{r}_1 - \vec{r}_2|$ is given in units of 'pixel width'. The smallest pores have a diameter of 5 pixel widths. With respect to the model objects with which the experiments were carried out, a pixel width corresponds to 80 μm. The base lattice size was 200×200. The porosities are given in table 1. The curve parameter is the growth–nucleation quotient f_c. The porosity was kept constant in all cases. The correlation function decay can be subdivided into three sections as indicated for $f_c = 1000$. The cut-off at large distances is due to the finite size of the cluster.

6.5. *The spatial velocity autocorrelation function*

Spatial velocity autocorrelation functions were evaluated from CFD simulated velocity maps of percolating clusters on a square base lattice of size 200×200 according to

$$G(r) = \frac{\langle \vec{v}(\vec{r}_1) \cdot \vec{v}(\vec{r}_2)\rangle}{\langle v^2 \rangle}, \tag{11}$$

where $r = |\vec{r}_1 - \vec{r}_2|$ is the distance between two pore space sites located inside the cluster. Typical results are shown in figure 14 where the total percolation networks with a given porosity $p_{final} = 0.6$ were considered. Evaluations based on the percolating clusters alone with a given porosity $p_{cluster} = 0.5616 \pm 0.0002$ do not alter the dependence on the growth–nucleation quotient f_c. Three distinct regions can be identified.

Region I refers to the pixel width which is one-fifth of the smallest pore diameter b. The correlation function is therefore constant in this region. The decay starts in region II with a crossover range of a few pixel widths corresponding to the smallest pores.

Region II ranges up to the correlation length ξ. The dependence of ξ on the growth–nucleation quotient is shown in figure 6. The width of region II therefore varies correspondingly.

The spatial velocity autocorrelation function can be described in a wide section of this regime by a power law

$$G(r) \propto r^{-\alpha}, \quad \text{where } b < r < \xi, \tag{12}$$

which is the more pronounced the larger the correlation length, that is, for larger growth–nucleation quotients. The exponent α increases with the growth–nucleation quotient f_c. A reliable evaluation of the exponent is however difficult for small f_c values because region II then becomes rather narrow.

The decay in region II gets steeper with increasing f_c. This is considered to be a consequence of the size of the obstacles around which the liquid needs to flow. The obstacle size increases with f_c (for an illustration see figure 2). The flow tortuosity caused by obstacles grows with the obstacle size at constant porosity. The velocity direction consequently varies in a wider range for larger f_c whereas flow streamlines in entirely random clusters of high porosity tend to be straight with little directional fluctuations.

The 'plateau region' III arises for $\xi \ll r \geqslant l_{cluster}$. Actually, the plateau character becomes more pronounced the larger the width of this region, that is for low f_c. Otherwise finite-size cut-off effects and the influence of inflow and outflow at the edges of the cluster become perceptible and affect the plateau character of this region.

7. Discussion and conclusions

The above results refer to a combined experimental and computational study of the structure and transport properties of Ising-correlated quasi-two-dimensional percolation model objects. It is shown that characteristic parameters such as the percolation threshold, correlation length and fractal dimension deviate from the values found for uncorrelated, that is random site-percolation model objects reported in previous papers. Dependences on the growth–nucleation quotient and on the porosity have been examined.

Taking into account the finite size of the systems under examination here, the percolation threshold value is found to be lower than in random site-percolation networks and interestingly shows a minimum in a range $30 < f_c < 320$ of the growth–nucleation quotient. This is in accordance with findings reported in [9, 28] for other correlated percolation models. Correlations significantly diminish the percolation threshold as a result of the clustering of, on the one hand, low and, on the other hand, high permeability regions. This is consistent with experimental observations that indicate a high permeability of many natural porous media even at very low porosities [2].

The explanation of the minimum of the percolation threshold is that, with increasing growth–nucleation quotient, the cluster size increases which favours transport across the network. However, there is an opposite tendency by the fact that the number of clusters is reduced at the same time. At growth–nucleation quotients far below 100, the first tendency dominates whereas above that value the second trend starts to govern the dependence on the growth–nucleation quotient.

The correlation length obeys a power law, equation (5), in a wide range leading to strongly increasing values for larger growth–nucleation quotients. This tendency is also visible in region II of the spatial velocity correlation function: This 'scaling region' is getting wider with increasing growth–nucleation quotient and is terminated by a crossover to a weakly indicated 'plateau region' at the correlation length (see figure 14).

The hydrodynamic dispersion of a neutral tracer in the flow field was studied as a function of the Péclet number using again computer simulation tools. Two regimes of the mean travelling time could be identified corresponding to an isotropic dispersion range, $Pe < 1$, where incoherent Brownian motions dominate, and a mechanical dispersion interval, $1 < Pe < 10^4$, where coherent flow controls dispersion almost completely [2, 10].

While random site-percolation clusters show some universality with respect to the choice of the elementary pore shape (‘random site’, ‘swiss cheese’ and ‘inverse swiss cheese’) [18], the Ising-correlated structures considered here appear to form another category with different parameter features. Ising-correlated percolation clusters are expected to mimic the structure of natural porous materials that were formed by growth processes of a similar nature. The main pore space feature that matters here is the larger pore connectivity resulting from the correlation assumed in the growth algorithm generating the models. This is in contrast to random site-percolation networks which are known to be too ‘random’ for the description of typical porous media.

As a general remark, it may be noteworthy in this context that the Ising-correlated quasi-two-dimensional percolation networks considered here can be associated to the growth dynamics of urban clusters. Corresponding analyses have been published in [32, 33]. This sort of comparison may be of interest with respect to the dependence of the cluster parameters on the growth–nucleation quotient.

Acknowledgments

We thank M Weber and I Ardelean for helpful discussions. This work was supported by the Deutsche Forschungsgemeinschaft.

References

[1] Hughes B D 1996 *Random Walks and Random Environments* (Oxford: Clarendon)
[2] Sahimi M 1995 *Flow and Transport in Porous Media and Fractured Rock* (Weinheim: VCH)
[3] Dullien F A L 1992 *Porous Media* (San Diego, CA: Academic)
[4] Bunde A and Havlin S 1996 *Fractals and Disordered Systems* (Berlin: Springer)
[5] Stauffer D and Aharony A 1992 *Introduction to Percolation Theory* (London: Taylor and Francis)
[6] Hermann H 1991 *Stochastic Models of Heterogeneous Materials* (Zürich: Trans Tech)
[7] Orbach R 1986 *Science* **231** 814
[8] Poole O J and Salt D W 1996 *J. Phys. A: Math. Gen.* **29** 7959
[9] Blumberg R L, Shlifer G and Stanley H E 1980 *J. Phys. A: Math. Gen.* **13** L147–L152
[10] Makse H A, Andrade Jr, J S and Stanley H E 2000 *Phys. Rev.* E **61** 583
[11] Chaves C M and Koiller B 1995 *Physica* A **218** 271
[12] Argyrakis P and Kopelman R 1986 *J. Chem. Phys.* **84** 1047
[13] Isichenko M B 1992 *Rev. Mod. Phys.* **64** 961
[14] Kimmich R 1997 *NMR Tomography, Diffusometry, Relaxometry* (Berlin: Springer)
[15] Müller H P, Weis J and Kimmich R 1995 *Phys. Rev.* E **52** 5195
[16] Müller H P, Kimmich R and Weis J 1996 *Phys. Rev.* E **54** 5278
[17] Klemm A, Müller H P and Kimmich R 1997 *Phys. Rev.* E **55** 4413
[18] Klemm A, Kimmich R and Weber M 2001 *Phys. Rev.* E **63** 041514
[19] Klemm A, Metzler R and Kimmich R 2002 *Phys. Rev.* E **62** 021112
[20] Weber M and Kimmich R 2002 *Phys. Rev.* E **66** 026306

[21] Weber M and Kimmich R 2002 *Phys. Rev.* E **66** 056301
[22] Buhai B, Hakimov A, Ardelean I and Kimmich R 2004 *J. Magn. Reson.* **168** 175
[23] Kimmich R, Klemm A, Weber M and Seymour J D 2001 *Mater. Res. Soc. Symp. Proc.* **651** T2.7.1
[24] Mantle M D and Sederman A J 2003 *Progr. NMR Spectrosc.* **43** 2
[25] Kimmich R 2002 *Chem. Phys.* **284** 253–85
[26] Stapf S and Han S-I (eds) 2005 *NMR Imaging in Chemical Engineering* (Weinheim: VCH)
[27] Coniglio A, Nappi C, Russo L and Peruggi F 1977 *J. Phys. A Math. Gen.* **10** 205
[28] Prakash S, Havlin S, Schwartz M and Stanley H E 1992 *Phys. Rev.* A **46** 1724
[29] Ziff R M 1992 *Phys. Rev. Lett.* **69** 2670
[30] Sederman A J, Mantle M D, Buckley C and Gladden L F 2004 *J. Magn. Reson.* **166** 182
[31] Fluent Inc. 1998 *Fluent and Gambit User's Guide Manual* July 26
[32] Makse H A, Havlin S and Stanley H E 1996 *Nature* **377** 608–12
[33] Makse H A, Andrade Jr, J S, Batty M, Havlin S and Stanley H E 1998 *Phys. Rev.* E **58** 7054
[34] Knackstedt M A, Sahimi M and Sheppard A P 2000 *Phys. Rev.* E **61** 4920

III

B.Buhai, and R. Kimmich

Dissimilar Electro-Osmotic Flow and Ionic Current Recirculation Patterns in Porous Media Detected by NMR Mapping Experiments

Physical Review Letter **96**, 174501, p1-4 (2006)

PRL 96, 174501 (2006) PHYSICAL REVIEW LETTERS week ending 5 MAY 2006

Dissimilar Electro-Osmotic Flow and Ionic Current Recirculation Patterns in Porous Media Detected by NMR Mapping Experiments

Bogdan Buhai and Rainer Kimmich

Sektion Kernresonanzspektroskopie, Universität Ulm, 89069 Ulm, Germany

(Received 1 August 2005; revised manuscript received 31 January 2006; published 2 May 2006)

Random-site percolation clusters were milled into ceramic (polar) and polystyrene (nonpolar) plates as a paradigm for porous media or complex microsystem channel networks. The pore space was filled with electrolyte solutions. Using NMR microscopy techniques, maps of the following quantities were recorded: (i) flow velocity driven by external pressure gradient, (ii) electro-osmotic flow (EOF) velocity, (iii) ionic current density in the presence of EOF, (iv) ionic current density in the absence of EOF. As far as possible, the experiments were supplemented by computational fluid dynamics simulations. It is shown that electro-osmotic flow as well as the electric current density include vortices and recirculation patterns. Remarkably, all transport patterns turned out to be dissimilar, and the occurrence and positions of vortices do not coincide in the different maps.

DOI: 10.1103/PhysRevLett.96.174501 PACS numbers: 47.56.+r, 76.60.Pc, 83.85.Fg

Electro-osmotic flow (EOF) arises when an electric field is applied to an electrolyte solution in channels with polar walls [1,2]. The wall surfaces become charged due to dissociation of polar groups of the wall material. The surface charges are compensated by surplus counterions in the solution. At thermal equilibrium, this net charge density decays from the highest value in the immobile "compact layer" directly at the surface down to zero across the mobile "diffuse layer." In an electric field, the mobile surplus counterions in the diffuse layer are driven towards the coelectrode. That is, viscous friction between the surplus counterions and the solvent causes shear flow in the diffuse layer whereas the electrically neutral solution in the middle of the channel is characterized by a flat flow velocity profile.

This is the standard scenario one usually has in mind when speaking of EOF [3,4]. Corresponding NMR studies essentially revealing the "plug flow" characteristics of electro-osmotic velocity profiles have been published in Refs. [5,6]. However, when the electrolyte solution is filled into a complex channel network, totally different transport patterns arise particularly if the pore space is closed. In the present study, the unique capability of nuclear magnetic resonance (NMR) techniques to visualize and quantify velocity and electric current density (ECD) vector fields in complex geometries will be demonstrated. Velocity vector fields due to EOF and external pressure gradients are compared with electric current density vector fields in the presence and absence of EOF. Recirculation patterns and vortices are striking features of transport maps. In the comparisons following below, we will therefore focus on these characteristics.

The existence or absence of a similitude between fluid velocity and electric field is of crucial importance for microsystem devices as discussed in Ref. [7]. As a paradigm for complex systems, we have used a random-site percolation network [8] generated on a computer. The percolating cluster shown in Fig. 1 served both as a basis for computational fluid dynamics (CFD) simulations and as a template for the fabrication of real model objects. Identical pore spaces were milled on the one hand in glass ceramic plates (MACOR, Schröder Spezialglastechnik GmbH) as a polar material leading to EOF upon application of an electric potential gradient, and in polystyrene (PS) plates on the other. PS is nonpolar and, hence, does not show EOF. The fabrication technique is described in Refs. [9,10]. The in-plane size of the percolation object Fig. 1 is 100 × 100 pixels corresponding to 4 cm × 4 cm (or 6 cm × 6 cm if the inflow and outflow or electrode compartments are implied). The thickness of the pore space was 400 μm. Figure 1(b) shows a NMR spin density map [11] of water filled into the object. The computer generated template, Fig. 1(a), is obviously very well reproduced in the experiment. This demonstrates the reliability both of the fabrication and the NMR imaging methods.

For sensitivity reasons and in order to ensure the quasi-2D character required for the ECD experiments [12], 7–10 identical but independently fabricated model objects were stacked and studied at a time. Therefore, any potential imperfections such as surface defects are averaged out

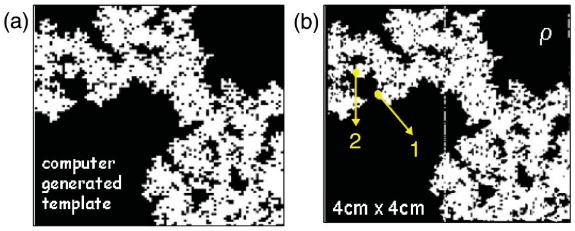

FIG. 1 (color). (a) Computer generated random-site percolation cluster (white). The porosity of the total percolation network (including isolated clusters not shown here) is $p = 0.6$. (b) NMR map of the spin density ρ of the water filled into to the pore space of an object fabricated on the basis of the template shown in (a). The matrix is again rendered in black. The areas marked by the numbers 1 and 2 refer to plots shown in Figs. 2 and 3.

© 2006 The American Physical Society

and cannot be responsible for the observed transport patterns (compare Ref. [13]). The negligible influence of surface heterogeneities was also corroborated by test experiments with straight channels. The EOF eddies considered in Ref. [1], chap. 5, for this sort of device were not found in our experiments. The conclusion is that the pore space surfaces of our objects are homogeneous enough.

All experiments were carried out with a NMR tomograph consisting of a home made radio frequency console and a Bruker 4.7 T magnet with a 40 cm horizontal bore. The principles of flow velocity and electric current density mapping with NMR microscopy techniques are outlined in Refs. [11,12,14–16]. The echo time was 28 ms, the repetition time 4 s. The spatial resolution of the maps was in the range 180–270 μm. Velocities were resolved with an accuracy of 0.03 mm/s. The electric current density could be determined within $\pm 2\ \mu\mathrm{A/mm}^2$ [15]. The liquid state NMR signals on which the experimental maps are based solely originate from the water in the pore space.

For the EOF experiments, the object was filled with 1 mM $\mathrm{CaCl_2}$ in distilled water. The conductivity of the bulk solution was 2.44×10^{-4} S/m. The gold electrodes consisted of two interdigitated combs in order to avoid eddy currents. The voltage applied across the 6 cm distance between the electrodes was in the range 300 to 900 V. The system was closed so that no inflow or outflow of the electrolyte solution was possible. The NMR velocity mapping pulse sequence is the same as described in Refs. [9,16] supplemented by a dc voltage applied during the whole echo time. The echo time was varied between 10 and 50 ms with no perceptible effect on the EOF velocity maps. Theoretically, one estimates a settling time of 28 ms according to Eq. (90) on p. 129 of Ref. [1]. Therefore, the assumption of steady state conditions is justified (compare Ref. [6]). Typical EOF velocity maps are shown in Figs. 2(a) and 3(b). The counterpart, pressure driven flow velocity maps are represented by Fig. 2(d). Detail maps for the area at position 1 [see Fig. 1(b)] are also shown in vector or streamline representation.

ECD mapping experiments were carried out again with an aqueous $\mathrm{CaCl_2}$ solution, but with 10 times larger concentration and conductivity to optimize the ECD encoding efficiency (note that ECD mapping is based on a measuring principle totally different from velocity mapping). The pulse sequence is described in detail in Refs. [12,16]. The electric current pulses during the pulse sequence had a strength of 40 mA and were 4 ms long. The voltage across the objects (6 cm) was 300 V. The mean current density (magnitude) is estimated to be 36 A/m^2. The precession phase maps recorded under the action of the current were ‘‘unwrapped’’ using Goldstein’s two-dimensional unwrapping algorithm [17]. Typical ECD maps are shown in Figs. 2(b) and 3(c) recorded in the MACOR object, i.e., in the presence of EOF. This is to be compared with the ECD map, Fig. 2(c), measured in the PS object where EOF does not arise. Detail maps of the area around position 1 of Fig. 1(b) are again shown.

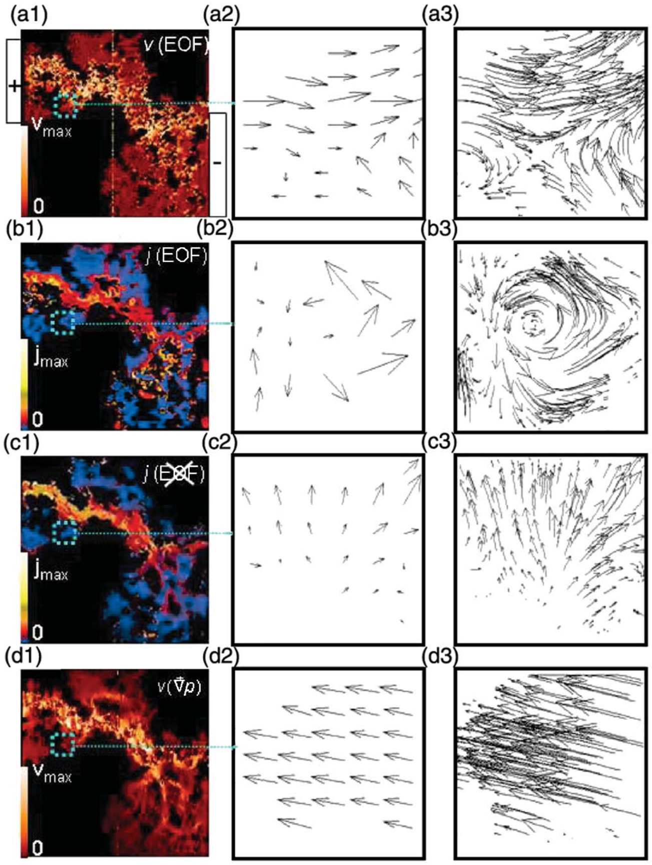

FIG. 2 (color). Left-hand column: Experimental maps of the magnitudes of different transport quantities measured in percolation model objects in a 4 cm × 4 cm field of view (see Fig. 1). The matrix is rendered in black. (a) EOF velocity, v(EOF), at a mean electric field strength of 83 V/cm (polar matrix). The position of the (closed) electrodes is indicated. (b) Electric current density in the presence of EOF, j(EOF) (polar matrix). (c) ECD in the absence of EOF, j (EOF off) (nonpolar matrix). (d) Flow velocity caused by an external pressure gradient in the open system, $v(\vec{\nabla} p)$. Middle column: Enlarged area at position 1 marked in Fig. 1(a) in vector plot form. The size is 1.2 mm × 1.2 mm. Right-hand column: Same as before, but now in streamline representation. That is, the vector arrows are bent along the local streamlines, and the length of the curvilinear vectors is proportional to the mean magnitude along the arrow. Typical maximum values for the velocity and electric current density are $v_{\mathrm{max}} = 4.5$ mm/s and $j_{\mathrm{max}} = 5\ \mathrm{mA/mm}^2$, respectively.

Hydrodynamic transport of an electrolyte solution in a polar porous medium is governed by pressure gradients, viscous friction, and electrostatic interaction between ions and external electric fields [18,19]. The flow velocity field, $\vec{v} = \vec{v}(\vec{r})$, is described by the Navier-Stokes equation assuming incompressible fluids and negligible gravitational forces. Under steady state conditions, this equation reads for external electrostatic forces

$$\rho_m(\vec{v} \cdot \vec{\nabla})\vec{v} + \vec{\nabla} p - \eta \nabla^2 \vec{v} = \rho_q \vec{E}, \tag{1}$$

where ρ_m and ρ_q are the mass and charge densities, respectively, η is the viscosity of the fluid, and $\vec{E}$ is the electric field strength. The "no-slip" boundary conditions usually assumed at the pore walls ($v_{\mathrm{wall}} = 0$) will, however, not be used for the CFD calculations (see below).

The electrostatic potential due to the electric double layer, Φ_{EDL}, obeys the Poisson equation

$$\nabla^2 \Phi_{\mathrm{EDL}} = -\frac{1}{\epsilon_0 \epsilon} \rho_q, \tag{2}$$

where ϵ is the dielectric constant of the electrolyte solution, and ϵ_0 is the electric field constant. The charge density is distributed in the electrostatic potential according to a Boltzmann factor,

$$\rho_q = e \sum_i c_{i0} z_i \exp\left\{-\frac{z_i e \Phi_{\mathrm{EDL}}}{k_B T}\right\}, \tag{3}$$

where e is the positive elementary charge, c_{i0} and z_i are the bulk concentration and the valence of the ith ionic species, respectively, k_B is Boltzmann's constant, and T is the absolute temperature. The boundary condition for the Poisson equation in the Debye-Hückel approximation is given by the ζ potential on the surface and is zero at infinity [1].

A finite element CFD method [20,21] was employed for comparison with the experiments. Since the electric double layer at the pore walls is not resolved in the experiments by far, there is no need to do so in the simulations. That is, instead of a no-slip boundary condition at the surfaces, an effective slip boundary condition is used. The numerical solutions were obtained with the aid of the software package FEMLAB 3 [22]. The model assumed in the calculations is described in Refs. [22,23]. The simulations were performed using a network of triangular meshes with 65 268 elements and 453 443 degrees of freedom for the two-dimensional percolation cluster used as a template for the model object. Any effects of chemical reactions between the walls, electrodes and solution were neglected.

Figure 4 shows a comparison of simulated EOF streamlines and vector plots for open [Fig. 4(a) and 4(b)] and closed electrodes [Fig. 4(c) and 4(d)]. "Open" means that there are infinite electrolyte solution reservoirs at both electrodes permitting unrestricted inflow and outflow. The streamline patterns simulated in two dimensions turned out to be similar to experimental velocity maps although the quasi-2D model objects in reality are 3D, of course. The third dimension, in particular, means that the friction and electroosmosis at the planes covering the pore space at the top and at the bottom should be considered. Corresponding simulations require, however, excessive computer capacity which was not available. Comparisons of experimental maps with two-dimensional simulations in this study or those in Ref. [7] can therefore be only of a qualitative nature. The simulations reveal the same phenomena as the experiments and therefore rule out any eddy current artifacts by field gradient pulses employed during the pulse sequences [12]. The influence of Taylor-Aris dispersion effects on EOF [24] can be excluded on the same basis.

EOF is strongly modified by hydrodynamic pressure gradients built up in the pore system. Flow in pore spaces sealed at the electrodes are characterized by a tendency to form recirculation patterns and vortices. In this case, EOF along the electric field lines is accompanied by flow in opposite directions. The velocity vector representation in the detail plots Figs. 4(b) and 4(d) visualize the different flow patterns and the occurrence of loops in the closed system.

All experimental EOF maps refer to closed systems. Hence, the finding of stationary EOF recirculation patterns [see Fig. 3(b)] is not unexpected. This is in contrast to flow driven by external pressure gradients. The two-dimensional CFD simulation predicts a vortex at position 1 [see Fig. 3(a) and compare Fig. 4(d)], whereas the NMR experiment did not show any such recirculation pattern [Fig. 2(d)].

Remarkably, ECD maps do also reveal vortices. This is demonstrated in Figs. 2(b) and 3(c). A condition for such recirculation phenomena appears to be the presence of EOF, since the vortices disappear if the matrix consists of PS. A comparison of ECD maps with and without EOF is given in Figs. 2(b) and 2(c).

There is a tendency that the electro-osmotic effect favors the occurrence of eddies both of the flow velocity and electric current density (Fig. 3). However, the positions of the areas where vortex phenomena occur do not coincide. In the absence of EOF, no complete vortex pattern was found at any position neither for flow [Fig. 2(d)] nor for electric current [Fig. 2(c)]. The same applies to simulations of the EOF velocity in open systems [Fig. 4(b)].

Flow eddies attached to obstacles are well-known even for extremely low Reynolds numbers. On the other hand, the fact that electric current vortices have been observed appears to be remarkable in view of the known property $\vec{\nabla} \times \vec{E} = 0$ for electrostatic field strengths. Both in the experiments and CFD simulations, no coinciding recirculation patterns could be identified for different transport quantities or different driving forces or different boundary conditions at the electrodes. This raises the question of similitude between the fluid velocity and electric field in

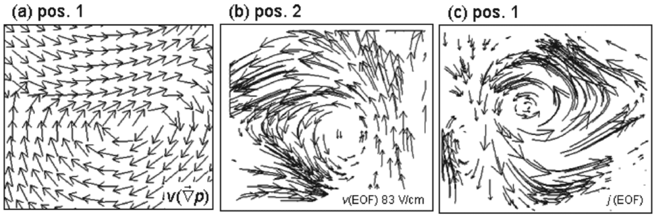

FIG. 3. Vortices of different transport quantities at positions 1 or 2 [see Fig. 1(b)]. (a) Two-dimensional CFD simulation of the flow velocity driven by an external pressure gradient at position 1 (area 0.8 mm × 0.8 mm). (b) Experimental EOF velocity at position 2 (area 1.2 mm × 1.2 mm) in streamline representation. (c) Experimental ECD in the presence of EOF at position 1 (area 1.2 mm × 1.2 mm) in streamline representation.

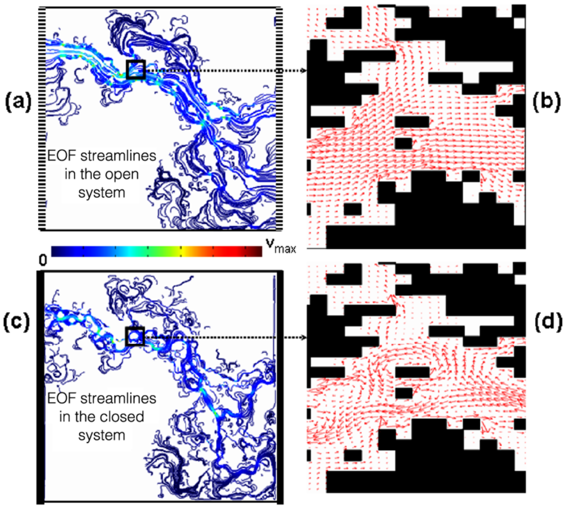

FIG. 4 (color online). Comparison of CFD simulations of EOF in open and closed two-dimensional random-site percolation clusters. The "percolating" cluster is shown in Fig. 1. (a) Streamlines in an open system with permeable electrodes on the left and right. Inflow and outflow from and to reservoirs is assumed to be unrestricted in this case. The matrix is not shown. The color (or gray shade) of the streamlines encodes the local velocity. (b) Enlarged velocity vector representation of the area marked in (a). The matrix is now rendered in black. (c) and (d) Same as (a) and (b), but now for a closed system excluding any inflow or outflow. The different flow patterns are obvious when considering the vector representations in (b) and (d).

EOF as discussed in Ref. [7]. All our EOF experiments refer to closed electrodes. That is, the Helmholtz-Smoluchowski equation which relates the flow velocity linearly with the electric potential gradient is not satisfied at those boundaries. This is considered to be the main reason why the similitude conditions of Ref. [7] do not apply.

The electrodynamic and hydrodynamic transport patterns in the presence and absence of electro-osmosis in complex systems reported here are important for applications in microsystem technology [25]. Microsystem devices often consist of complex channel networks implying features of the model objects of the present study. Based on a structure producing closed-loop flow, cyclic electro-osmotic pumps can be designed, for example. The intentional production of recirculation in such systems is essential for the function of microsystem mixers as discussed in Ref. [26]. Generally, the combined application of NMR microscopy techniques for the quantitative, noninvasive visualization of the total variety of hydrodynamics and electrodynamics in the same channel system is a promising design tool in microsystem technology. In this sense, the NMR methods used here are unique and superior to conventional fluid dynamics techniques such as particle image, ultrasound Doppler, or laser Doppler velocimetry [27,28].

[1] D. Li, *Electrokinetics in Microfluidics* (Elsevier, London, 2004).

[2] R. F. Probstein, *Physicochemical Hydrodynamics* (Wiley, New York, 1994).

[3] W. Zhu, S. J. Singer, Z. Zheng, and A. T. Conlisk, Phys. Rev. E **71**, 041501 (2005).

[4] S. Yao and J. G. Santiago, J. Colloid Interface Sci. **268**, 133 (2003).

[5] D. Wu, A. Chen, and C. S. Johnson, Jr., J. Magn. Reson., Ser. A **115**, 123 (1995).

[6] B. Manz, P. Stilbs, B. Jönsson, O. Söderman, and P. T. Callaghan, J. Phys. Chem. **99**, 11 297 (1995).

[7] E. B. Cummings, S. K. Griffiths, R. H. Nilson, and P. H. Paul, Anal. Chem. **72**, 2526 (2000).

[8] D. Stauffer and A. Aharony, *Introduction to Percolation Theory* (Taylor and Francis, London, 1992).

[9] A. Klemm, R. Kimmich, and M. Weber, Phys. Rev. E **63**, 041514 (2001).

[10] M. Weber and R. Kimmich, Phys. Rev. E **66**, 056301 (2002).

[11] R. Kimmich, *NMR Tomography, Diffusometry, Relaxometry* (Springer, Berlin, 1997).

[12] M. Weber and R. Kimmich, Phys. Rev. E **66**, 026306 (2002).

[13] D. Long, H. A. Stone, and A. Ajdari, J. Colloid Interface Sci. **212**, 338 (1999).

[14] Y. Manassen, E. Shalev, and G. Navon, J. Magn. Reson. **76**, 371 (1988).

[15] G. C. Scott, M. L. G. Joy, R. L. Armstrong, and R. M. Henkelman, J. Magn. Reson. **97**, 235 (1992).

[16] E. Kossel, B. Buhai, R. Kimmich in *NMR Imaging in Chemical Engineering*, edited by S. Stapf and S.-I. Han (Wiley-VCH, Weinheim, 2005), Chap. 2.9.

[17] D. C. Ghiglia and M. D. Pritt, *Two Dimensional Phase Unwrapping* (Wiley, New York, 1998).

[18] C. L. Rice and R. Whitehead, J. Phys. Chem. **69**, 4017 (1965).

[19] R. J. Hunter, *Foundations of Colloidal Science* (Oxford University Press, Oxford, 1987), Vol. 2, p. 786.

[20] J. D. Anderson, *Computational Fluid Dynamics* (McGraw-Hill, New York, 1995).

[21] C. Cuvelier, A. Segal, and A. van Steenhoven, *Finite Element Methods and Navier-Stokes Equations* (Reidel, Dordrecht, 1988).

[22] *FEMLAB User's Guide* (Comsol AB, Stockholm, 2004).

[23] A. Ajdari, Phys. Rev. E **53**, 4996 (1996).

[24] P. Bendel, M. Bernardo, J. H. Dunsmuir, and H. Thomann, Phys. Rev. E **67**, 046307 (2003).

[25] Y. Takamura, H. Onoda, H. Inokuchi, S. Adachi, A. Oki, and Y. Horiike, Electrophoresis **24**, 185 (2003).

[26] H. Chen, Y. T. Zhang, I. Mezic, C. D. Meinhart, and L. Petzold, *Proc. Microfluidics 2003* (ASME IMECE, New York, 2003).

[27] E. Guyon, J.-P. Hulin, L. Petit, and C. D. Mitescu, *Physical Hydrodynamics* (Oxford University Press, New York, 2001).

[28] D. Yan, N. T. Nguyen, C. Yang, and X. Huang, J. Chem. Phys. **124**, 021103 (2006).

IV

B.Buhai, T. Binser and R. Kimmich

Electro-Osmotic Flow, Ionic Currents, and Pressure Induced Flow in Microsystem Channel Networks: NMR Mapping and Computational Fluid Dynamics Simulations

Applied Magnetic Resonance, in press (2006)

Electro-osmotic flow, ionic currents, and pressure induced flow in microsystem channel networks: NMR mapping and computational fluid dynamics simulations

Bogdan Buhai, Tobias Binser, Rainer Kimmich

Sektion Kernresonanzspektroskopie, Universität Ulm, 89069 Ulm, Germany

Abstract

Using NMR velocity mapping and NMR current density mapping as well as finite element computational fluid dynamics methods, transport in microsystem electrolytic cells with increasing complexity has been examined ranging from single straight channels to random site percolation clusters. This sort of system is considered as paradigm for more or less complex devices in microsystem technology. Corresponding model objects were designed on a computer and milled into ceramic (polar) or polystyrene (non-polar) matrices. The pore space was filled with electrolyte solutions. Maps of the following quantities were recorded: (i) velocity of hydrodynamic flow driven by external pressure gradients, (ii) velocity of electro-osmotic flow (EOF), (iii) ionic current density in the presence of EOF, (iv) ionic current density in the absence of EOF. As far as possible, the experiments were supplemented by computational fluid dynamics simulations. It is shown that electro-osmotic flow as well as the electric current leads to recirculation patterns in closed complex structures such as percolation clusters. Remarkably, all transport patterns turned out to be dissimilar, and the occurrence and positions of eddies do not coincide in the different maps. Velocity histograms and the mean velocity as a function of the porosity have been evaluated. An electro-osmotic flow percolation transition is found at the geometrical percolation threshold. The combined application of NMR techniques for the quantitative, non-invasive visualization of the total variety of hydro- and electrodynamics in the same channel system promises to become a powerful tool for design purposes in microsystem technology.

1 Introduction

Ionic currents, electro-osmotic flow (EOF), and pressure induced hydrodynamic flow (PIF) are transport phenomena of interest in microsystem devices. The purpose of this study is to map transport quantities such as the ionic current density (ICD) and the flow velocity due to electro-osmosis and hydrodynamic pressure gradients under the same geometrical conditions, and to compare the patterns of transport pathways. Microsystem model objects were fabricated for different degrees of complexity. This implies simple structures such as straight channels and random site percolation clusters. The latter are considered as a paradigm for branching channel networks as they may occur in complex microsystems. An important feature of this sort of system is the competitive action of thin and thick channels or bottlenecks connected in parallel.

The experimental techniques are based on magnetic resonance imaging. It is shown that nuclear magnetic resonance (NMR) provides a set of methods for quantitatively mapping electric and hydrodynamic quantities [1]. Model calculations were also performed for the same channel systems using finite element and finite volume methods. In this way, a complete picture of peculiarities of electrodynamic, electro-osmotic and hydrodynamic transport could be rendered both for theoretical and experimental data.

Electro-osmotic flow arises when an electric field is applied to a liquid electrolyte solution in channels with polar walls (e.g. ceramics) [2], [3]. That is, no such phenomena arise for non-polar wall materials (e.g. plastic). Comparing identical model objects made of polar and non-polar materials permits one to identify flow features specific for EOF.

The wall surfaces of polar materials become charged due to dissociation of polar groups of the wall material. The surface charges are compensated by surplus counterions in the solution. At thermal equilibrium, this net charge density decays from the highest value in the immobile “compact layer” directly at the surface down to zero across the mobile “diffuse layer”. In an electric field, the mobile surplus counterions in the diffuse layer are driven towards the co-electrode. That is, viscous friction between the surplus counterions and the solvent causes shear flow in the diffuse layer. In this way, the electrically neutral solution in the middle of the channel is moved in the same direction with a characteristic flat flow velocity profile. A schematic representation of electro-osmotic flow is shown in Fig. 1.

This is a typical scenario for EOF [4], [5]. Corresponding NMR studies essentially revealing the “plug flow” characteristics of electro-osmotic velocity profiles have been published in Refs [5], [7]. However, when the electrolyte solution is filled into a complex channel network, totally different transport patterns for electric and hydrodynamic driving forces arise particularly if the pore space is closed. On the one hand, this raises the question of the existence or absence of a similitude between fluid velocity and electric field as discussed in Ref. [8], and the difference between electro-osmotic and pressure induced hydrodynamic flow, on the other. All three phenomena can be mapped separately in the same object by probing the flow velocity and the ionic current density. This capability is a unique strength of nuclear magnetic resonance microscopy that has not been exploited so far.

Electro-osmotic flow in porous materials has been studied several times in the literature. Most of these papers deal with model theories with the objective to predict electro-osmotic flow features in porous media [9], [10]. A system quite often under consideration are glass bead packs [11], [12], [13]. This is in contrast to the present study which focuses on more or less branching channel systems as they may be relevant for microsystem technological applications in general.

Microfluidics is a fast developing field accompanying microsystem technology. One of the key elements is fluid transport as needed for “lab-on-a-chip” devices [14]. In Refs [2], [15], electro-osmosis in micrometer structures was shown to produce larger flow rates at high values of the hydraulic resistivity than pressure induced hydrodynamic flow for circulating a fluid. In this sense, electro-osmosis has been suggested to act as a pump that can be controlled externally by the applied potential gradient. The examination of microscopic transport reported here permitted us to visualize detailed features of such mechanisms with spatial resolution for the first time.

2 Theoretical background of electro-osmotic flow

The electrostatic potential due to the electric double layer, Φ_{EDL}, obeys the Poisson equation,

$$\nabla^2 \Phi_{EDL} = -\frac{1}{\varepsilon_0 \varepsilon} \rho_q , \tag{1}$$

where ε is the dielectric constant of the electrolyte solution, and ε_0 is the electric field constant. The charge density, ρ_q, is distributed in the electrostatic potential according to a Boltzmann factor,

$$\rho_q = e \sum_i c_{i0} z_i \exp\left\{ -\frac{z_i e \Phi_{EDL}}{k_B T} \right\}, \tag{2}$$

where e is the positive elementary charge, c_{i0} and z_i are the bulk concentration and the valence of the *i*-th ionic species, respectively, k_B is Boltzmann’s constant, and T is the absolute temperature.

In the high-temperature approximation, that is $\left| z_i e \Phi_{EDL} \right| << k_B T$, the right-hand side of Eq. (2) can be approximated linearly. This is the Debye/Hückel approximation valid for

$\Phi_{EDL} < 25\ \mathrm{mV}$. The boundary condition for Eq. (1) is given by the ς potential on the surface and zero at infinity [2], [3]. The Debye/Hückel parameter is defined by

$$k^2 = \frac{2z_i^2 e^2 n_{i,\infty}}{\varepsilon\varepsilon_0 k_b T}, \tag{3}$$

where $n_{i,\infty}$ is the bulk concentration of the ion species *i*. The width of the electric double layer is in the order of $1/k$.

The flow velocity field, $\vec{v} = \vec{v}(\vec{r})$, can be described by the Navier/Stokes equation assuming incompressible fluids and negligible gravitational forces. Under steady state conditions, this equation reads for external electrostatic forces

$$\rho_m\left(\vec{v}\cdot\vec{\nabla}\right)\vec{v} + \vec{\nabla}p - \eta\nabla^2\vec{v} = \rho_q\vec{E}_{ext}, \tag{4}$$

where $\vec{\nabla}\cdot\vec{v} = 0$. The pressure in the fluid is designated by p. The quantities ρ_m and ρ_q are the mass and charge densities, respectively, η is the dynamic viscosity of the fluid, and $\vec{E}_{ext}$ is the external electrical field strength. At the walls, the implicit “no-slip” boundary condition should be valid, i.e. $v_{wall} = 0$. According to the Helmholtz/Smoluchowski equation, the mean EOF velocity is predicted to obey

$$\left\langle v_{EOF}\right\rangle \approx \frac{\varepsilon}{\eta}\varsigma E_{ext}. \tag{5}$$

3 Materials and methods

3.1 Materials and test objects

Test objects have been fabricated using a silica based ceramic (MACOR, Schröder Spezialglastechnik GmbH [16]) and polystyrene plates (BASF GmbH [17]) as polar and non-polar materials, respectively. The porosity of the materials is negligible. Objects under consideration are represented in Fig. 2 as computer generated templates, photographs and spin density maps. The fabrication method is described in Ref. [18] in detail.

The in-plane size of the object consisting of the 7 parallel channels shown in Fig. 2, top row, is 6 cm x 6 cm (or 7.5 cm x 6 cm if the in- and outflow and electrode compartments are implied). The random-site percolation cluster [19] shown in Fig. 2, bottom row is based on a matrix of 100 x 100 pixels corresponding to 4 cm x 4 cm (or 6 cm x 6 cm with the in- and outflow and electrode compartments included). The thickness of the ceramic or polystyrene plates was 2 mm and the deepness of the micro-machined structures was 1 mm. 7

to 10 identical but independently micro-machined plates were stacked and studied at a time for sensitivity reasons and to ensure the quasi two-dimensional character of the experiments. In this way, any possible imperfections such as surface defects are averaged out. A photograph of the seven-channel object is shown in Fig. 3, left.

In all cases, the electrodes were gold-plated to ensure a better contact with the electrolyte and longer protection against corrosion. An interdigitated comb structure of the electrodes (see Fig. 3 right) prevents eddy currents during the imaging experiments.

The pore space of the objects was filled with an electrolyte solution. The electric conductivity is given by the empirical Kohlrausch law [20]

$$\sigma(c) = \Lambda_0 c - k_0 c^{3/2}, \tag{6}$$

where σ represents the conductivity, Λ_0 is the molecular conductance characteristic for the salt dissolved, and c is the salt concentration. k_0 is a constant depending on the salt valence. On this basis, the experimental parameters for EOF velocity mapping were estimated prior to the measurements.

For the EOF experiments, the model objects were filled with 1 mM $CaCl_2$ in distilled water. A conductivity of 2.44 x 10^{-4} S/m at room temperature was measured in the bulk solution with a conductivity meter (HANNA Instruments HI 8633). The voltage applied across the 7.5 cm distance between the electrodes was in the range 300 to 900 V and was generated by a KEPCO BOP 1000M power supply. The system was closed so that no in- or outflow of the electrolyte solution was possible. ICD mapping experiments were carried out again with an aqueous $CaCl_2$ solution, but with ten times larger concentration and conductivity to optimize the ICD encoding efficiency.

Other salts like KCl and $LaCl_3$ were also tested. In aqueous 1mM solutions, the conductivities were 1.46 x 10^{-4} S/m and 3.73 x 10^{-4} S/m, respectively. However, $CaCl_2$ turned out to provide the strongest EOF effect. Note that the correct conductivities are needed as parameters for the computer simulations carried out in parallel to the experiments.

3.2 Computational fluid dynamics methods

EOF velocity maps were simulated for the (two-dimensional) geometries of the test objects with the aid of algorithms described in Refs [21], [22]. All simulations are based on two-dimensional computational grid. Three-dimensional treatments failed because of the limited computer capacity available in this study. However, as will be demonstrated in the following, the crucial EOF properties are rendered already in two dimensions.

Two different commercial computational fluid dynamics programs were employed depending on the best adaptation to the problem to be solved. The first one, FEMLAB 3.0 [23], is based on the finite element method (FEM) and is suited for electro-osmotic flow and current density distributions. Simulations using this software were based on a network of triangular meshes with typically 65156 elements implying 452715 degrees of freedom.

The second commercial software, FLUENT 6.1 [24], is based on the finite volume method (FVM). It is appropriate for hydrodynamic flow generated by pressure gradients. Electric current density distributions can also be simulated but in an indirect way [25]. In this case, the number of triangular mesh elements was typically 87080.

The material parameters needed for the simulations were taken from the literature [2], [20]. The value of the dielectric permittivity was set to $\varepsilon_w = 7.127 \times 10^{-10}$. The zeta potential was assumed to be $\zeta = -100 \text{ mV}$.

The EOF calculations are simplified by the fact that the Debye/Hückel approximation is valid and that the electric double layer cannot be resolved in the experiments, and hence need not be resolved in the simulations either. Corresponding “slip” boundary conditions at the walls were assumed to take this simplification into account.

Formally, the Navier/Stokes equations can be written with the external force omitted,

$$\begin{aligned} &\rho_m \left(\vec{v} \cdot \vec{\nabla}\right)\vec{v} + \vec{\nabla} p - \eta \nabla^2 \vec{v} = 0, \\ &\vec{\nabla} \cdot \vec{v} = 0, \end{aligned} \tag{7}$$

by modifying the boundary condition according to

$$v_{wall} = -\frac{\varepsilon_w \varsigma_0}{\eta} E_{ext} \tag{8}$$

instead of the “no-slip” form mentioned above. ε_w is the dielectric permittivity at the walls, and ζ_0 represents the zeta potential. At the surfaces of the electrodes, a “no slip” boundary condition, $v_{electrodes} = 0$, was anticipated for “closed systems” without in- and outflow. This is in contrast to “open systems” where unrestricted flow across the electrode boundaries was assumed.

The electrical potential in an ionic solution without current sources and externally generated currents obeys the continuity equation for the current density, $\vec{j}$,

$$\vec{\nabla} \cdot \vec{j} = \vec{\nabla} \cdot \left(-\sigma \vec{\nabla} \Phi\right) = 0 . \tag{9}$$

The boundary conditions are given by

$$\begin{aligned}\Phi_{wall} &= \infty \quad (\hat{=}\ \text{insulation}),\\ \Phi_{electrodes} &= \Phi_0.\end{aligned} \tag{10}$$

Any effects by chemical reactions at the walls and electrodes were neglected.

Based on computer simulations, scenarios can be examined that are difficult to realize in experiment. In this sense, electro-osmotic velocity maps will be presented for open (permeable) electrodes in addition to maps for closed (impermeable) ones.

3.3 Nuclear Magnetic Resonance mapping techniques

Different NMR techniques [26], [27] were employed for mapping of the electro-osmotic flow velocity, the electric current density, and the pressure driven flow velocity. That is, the spatial distribution of any of those quantities is quantitatively rendered. Figure 4 shows schemes of the diverse pulse sequences. The standard Hahn spin echo radio frequency pulse sequence is combined with various magnetic flux density gradient and electric current pulses.

The pulse scheme represented by the three rows commonly labeled by A is used for acquiring two-dimensional images of an *x/y* slice of the object. Note that the Hahn echo selectively refers to the liquid in the objects, whereas the solid matrices do not contribute to the echo signal even if they contain protons. In case of homogeneous spin density and relaxation times in the fluid, *spin density maps* can be rendered in this way. The spatial resolution achieved in all three directions with the our hardware configuration was around 300 µm so that the pore space of the model objects could be well resolved in all details.

Adding two more Fourier domains in the form of gradient pulse pairs along the *x* and *y* directions to be incremented in subsequent scans leads to maps of the velocity components in *x* and *y* direction, respectively. That is, the gradient pulse sequences in rows A and B of Fig. 4 are employed together providing the phase encoded information on the spatially distributed velocity components so that the local velocity magnitude can be calculated. The known principles of phase encoding of a velocity component are explained in more detail in Refs [26], [27], for example. Incrementing the velocity phase encoding gradient pulses as shown in row B of Fig. 4 permits the determination of the velocity distribution within each voxel via Fourier transformation of the acquired data sets. The maximum phase encoding gradient determines the velocity resolution, the increment gives the maximum range of velocities (so to speak the velocity “field of view”) that can be measured. The values rendered in the maps refer to the maximum of the velocity distribution in the voxels. The intricacies of extremely broad variations of the flow velocity as they are expected in complex channel systems such as percolation clusters are discussed in Ref. [28], where a measuring protocol is given to avoid artifacts on these grounds.

To acquire maps of the electro-osmotic velocity, phase encoding of the velocity must be synchronized with a current pulse as shown in Fig. 4(C). The current pulse must be on long enough to achieve steady-state conditions before the proper phase-encoding experiment begins. A characteristic time to reach the steady state in porous materials can be calculated on the basis of Eq. (90) of Ref. [2], p.129:

$$t^* = \frac{\rho_m a^2}{\eta \lambda_1^2}, \tag{11}$$

where $\lambda_1 = 2.405$ is determined by the first null of the zero-order Bessel function, $J_0(\lambda_1) = 0$. a is the channel radius under consideration. i.e. the mean pore size in the case of porous materials. An estimate leads to $t^* \approx 27\ \text{ms}$. Experimentally, the echo time was varied in the range 10 to 50 ms with no effect on the EOF velocity maps. Therefore the assumption of steady state conditions is justified. The electro-osmotic flow (EOF) velocity is phase-encoded in the same way as the velocity of flow induced by pressure gradients (PIF).

Note that the ionic current producing electro-osmotic flow is on during the whole spin echo pulse sequence. Phase shifts due to the magnetic fields produced by the current will therefore be compensated and will not affect the signal. This is in contrast to the ionic current density (ICD) mapping experiment described below where such phase shifts intentionally are not refocused. It should also be noted that the gradients of the magnetic fields produced by the ionic current do not interfere with the gradients used for flow velocity encoding since they are not incremented as the gradient pulses in row B of Fig. 4 are.

The combination of the pulse sequences A and D in Fig. 4 permits one to map the ionic current density. The principle is based on Maxwell's fourth equation for stationary electromagnetic fields,

$$\vec{j}(\vec{r}) = \frac{1}{\mu_0} \vec{\nabla} \times \vec{B}(\vec{r}), \tag{12}$$

where $\vec{B}(\vec{r})$ is the magnetic flux density produced by the electric current density $\vec{j}(\vec{r})$ at position $\vec{r}$, and μ_0 is the magnetic field constant. The curl operation depends on all three spatial derivatives of the flux density by the spatial Cartesian coordinates. If the sample and the experimental set-up is such that a quasi two-dimensional current distribution invariant along the z direction exists, only two derivatives in the transverse plane remain finite:

$$
\begin{aligned}
j_z(\vec{r}) &= 0, \\
j_x(\vec{r}) &= \frac{1}{\mu_0}\frac{\partial B_z}{\partial y}, \\
j_y(\vec{r}) &= \frac{1}{\mu_0}\frac{\partial B_z}{\partial x}.
\end{aligned}
\tag{13}
$$

These derivatives can experimentally be determined from maps of the phase shifts of the local Larmor precession, that is, by evaluating the numerical derivatives along the x and y directions. Detailed descriptions of the method can be found in Refs [25], [27], [29]. According to Ref. [30], the optimal value for the total current pulse length, T_C, depends on the transverse relaxation time, T_2, the diffusion coefficient of the ions, D, the field-of-view, x_{fov}, and the number of pixels, N:

$$
\frac{1}{T_C} = \frac{1}{T_2} + 4D\left(\frac{4\pi N}{5x_{fov}}\right)^2 . \tag{14}
$$

Primarily, maps of the precession phase shifts by the local current density are recorded. Before deducing the spatial distribution of the current density from these maps, they must be “unwrapped”. Goldstein’s two-dimensional unwrapping algorithm turned out to be a favorable tool for this task [31].

The current pulses in row D of Fig. 4 had a strength of 40 mA and were 4 ms long. The voltage across the model objects (6 cm) was 300 V. The mean magnitude of the current density is estimated to be 36 A/m^2. Artifacts due to eddy currents induced by the field gradient pulses can safely be ruled out since simulations of the current distribution coincide with the experimental data [25].

As a unique feature of NMR imaging, all sorts of maps mentioned so far can be recorded in the same object using the same apparatus. This permits comparisons of entirely different transport quantities. For example, hydrodynamic flow is subject to viscosity and in principle also to inertia. This is in contrast to electric currents where no such effects matter. Also, the resistivities of hydrodynamic flow and electric currents scale with different exponents with the channel width [25].

In the following, we will refer to experiments with model objects made of a polar ceramic and of non-polar polystyrene. That is, electric current measurements were performed in structurally identical objects with and without the electro-osmotic effect.

3.4 Instruments

All experiments were performed with an NMR tomograph equipped with a home made radio frequency console. The magnetic field was provided by a Bruker 4.7 T magnet with a 40 cm horizontal bore at room temperature. The probe head was a Bruker birdcage resonator with an inner diameter of 195 mm. The maximum field gradient was 50 mT/m in all three space directions. The echo time was typically chosen to be 28 ms, the repetition time 4 s. The spatial resolution of the maps was in the range 180..300 $\mu\mathrm{m}$. Velocities were resolved with an accuracy of 0.03 mm/s. The experimental error of the ICD measurements was $\pm 2\ \mu\mathrm{A/mm}^2$.

The current pulses were generated with the aid of a KEPCO BOP 200-1M power supply controlled by a home build electronic device. The available range of the current strength was between 10 mA and 1 A. The maximum current practically used was however only 0.1 A. Any Joule heating during the electro-osmosis experiments can safely be neglected. An estimation based on Eq. 55 in Ref. [2], Section 4-3.7, suggests a temperature increase smaller than 10^{-3} °C under the conditions of our experiments.

A hydrostatic pressure gradient for flow experiments was generated by a reservoir situated 2 meters above the sample. It was permanently kept on a constant level with the aid of a peristaltic pump. The flow rates were in the range $0.1-0.3$ ml/s.

4. Results

In the following, NMR experiments performed with quasi two-dimensional objects as well as simulations of two-dimensional structures of the same pore space geometry of varying complexity will be reported. The phenomena to be considered are EOF in open and closed systems, the distribution of ICD in the presence and absence of EOF, and PIF caused by hydrostatic pressure gradients.

4.1 EOF and hydrodynamic backflow in straight channel systems in a polar matrix

In a system with closed electrodes, the electro-osmotic driving force causes hydrodynamic backflow so that stationary flow patterns with closed streamlines arise. This can be demonstrated by a simulation of a two-dimensional tube in a polar matrix with electrodes at the ends. The result is shown in Fig. 5. Assuming a negative zeta potential, electro-osmosis is expected to drive the electrolyte solution from the anode to the cathode. As a consequence, there must be flow in the opposite direction in the central part of the tube.

If two channels of differing widths are connected in parallel, an interesting situation arises. Since the electro-osmotic effect in the thinner channel is relatively stronger than in the thicker one, a cyclic flow pattern arises as demonstrated in Fig. 6a for a closed system with impermeable electrodes. This is in contrast to the open system with permeable electrodes represented by Fig. 6b.

A closed device of this sort could be employed as a cyclic pump in microsystem technology. The flow direction can readily be reversed by changing the polarity of the electrodes. The appealing feature of such a cyclic pump would be that no mechanical parts are needed and that the pump rate can be controlled electronically.

Adding more channels in parallel distributes the effective flow rates according to the distribution of the channel widths as shown in Fig. 7. This sort of device was also fabricated as a quasi two-dimensional object (see Fig. 2b). An experimental EOF velocity map is shown in Fig. 8. Both the (cyclic) flow directions and the width dependent flow rates predicted by the simulations were verified. The mean flow velocity was evaluated as a function of the channel width and plotted in Fig. 9a for three different voltages. The minimum and maximum flow rates are $Q_{\min} = 0.034 \text{ mm}^3/\text{s}$ and $Q_{\max} = 0.378 \text{ mm}^3/\text{s}$, respectively.

The coincidence of the streamlines in the two-dimensional simulations and in the experiments referring to three-dimensional objects is striking. This is quantitatively illustrated in Fig. 9b. The third dimension in particular means that the friction and electro-osmosis at the planes covering the pore space at the top and at the bottom matter in the experiments and should be considered in the simulations. Corresponding simulations require, however, excessive computer capacity which was not available in our case.

Figure 10 shows velocity maps for a three-electrode device recorded in experiments and reproduced in simulations. EOF follows the steepest gradient of the electrostatic potential. So, when changing the polarity of the electrodes, one can steer the effective flow direction and the flow path as indicated by the bold arrows. On the other hand, this geometry is a first step towards a branching network as it will be considered in the next section.

4.2 Percolation clusters

Percolation clusters are taken as a paradigm for complex channel networks as they are pertinent for microsystem technology. Figure 11 shows simulations of diverse experimentally accessible transport quantities in the percolation cluster shown in Fig. 2. This refers to ICD, the EOF velocity for permeable and impermeable electrodes, and to PIF. According to the vector representations on the right-hand column of Fig. 11, one expects different transport patterns for these quantities. In fact, this was demonstrated by the experimental maps shown in Fig. 12.

Typical experimental EOF velocity maps in the percolation cluster shown in Fig. 2 (bottom) are rendered in Fig. 12A. The mean flow velocity obeys the Helmholtz/Smoluchowski equation given in Eq. (5) as verified in Fig. 13 both in experiment and simulation.

Counterparts of these velocity maps are the experimental PIF velocity maps shown in Fig. 12D. The different flow and current patterns with and without electro-osmotic flow are remarkable. In the presence of EOF, both the velocity and ICD maps show recirculation patterns (see Figs 14B and C). However, the positions where these phenomena were observed are different. At position 1 (see Fig. 2c, bottom), no flow vortex could be identified whereas the electric current density clearly reveals a sort of eddy. At position 2, on the other hand, the findings are just opposite: No ICD vortex, but a clear $\vec{v}_{EOF}$ eddy. In the absence of EOF, no complete vortex pattern was found at any position neither for flow nor for electric current (see Figs 12C and D, for instance). This is in contrast to the simulations where to some degree vortex-like structures appeared (see e.g. Fig. 14A). Likely, this is due to the strict two-dimensionality of these computations.

Fig. 12B shows a typical experimental ICD map derived from an unwrapped phase map recorded in the ceramic object, i.e. in the presence of EOF. This is to be compared with the ICD map, Fig. 12C, recorded in the object made of polystyrene, that is in the absence of EOF. The detail vector representations in the right-hand columns indicate that there must be a strong interference between flow and ionic current, since the ionic currents current distributions measured with and without background EOF are so different.

The different patterns observed for hydrodynamic flow and electric currents were already discussed in Ref. [25]. The respective resistivities as a function of the channel width (at constant thickness) scale with different powers as demonstrated in Fig. 15 for a test object with an arrangement of 10 parallel channels of varying widths similar to the one shown in Fig. 2 (top). That is, pressure induced hydrodynamic flow is more strongly hindered by thin passages than ionic currents. Electro-osmotic flow, on the other hand, is a matter of the available surface area and the applied voltage. Therefore, EOF tends to be less concentrated to the widest channel pathways than pressure induced flow.

Flow eddies attached to obstacles are well known even for extremely low Reynolds numbers. On the other hand, the fact that electric current vortices have been observed appears to be quite remarkable in view of the known property $\vec{\nabla} \times \vec{E} = 0$ for electrostatic field strengths. Moreover, the positions of the areas where vortex phenomena occur for electric and hydrodynamic transport do not coincide. The conclusion is that the combination of hydro- and electrodynamic phenomena leads to new effects not foreseen by the theories of each of these formalisms. It appears that there is no similitude between these two sorts of transport [8] and that the Helmholtz/Smoluchowski equation which relates the flow velocity with the electric potential gradient is not satisfied in the case of closed electrodes.

4.3 Percolation transition

The EOF patterns get more and more distorted with decreasing porosity until all end-to-end pathways are interrupted. No sample spanning loops are possible below the percolation threshold as demonstrated by the simulated streamline patterns in Fig. 16. Figure 17 shows the mean velocity magnitude as a function of the porosity. The sharp crossover from localized to sample spanning flow loops at the percolation threshold is obvious and reminiscent of the Rayleigh/Bénard percolation transition reported in Ref. [32].

The different flow behavior in percolating and isolated clusters reveals itself also in the velocity histograms shown in Fig. 18. The velocity distribution in closed but percolating clusters near the percolation threshold, $0.59 \le p < 0.65$, obeys a power law of the form $n(v) \propto v^{-b}$ (see the straight line in Fig. 18). Flow loops in isolated clusters by contrast tend to be characterized by a velocity distribution restricted to some range with a maximum. Interestingly the same sort of histogram arises far above the percolation threshold when the porosity is in the range $0.65 < p \le 1$. That is, global and local flow loops tend to obey similar velocity distributions although the maximum velocity is quite different. The power law close to the percolation threshold is considered to be a manifestation of the fractal character of random-site percolation networks.

5. Discussion

NMR microimaging provides a unique combination of mapping tools that can non-invasively be applied to the same transport system. In the present study, this permitted comparisons of electro-osmotic flow velocity maps, and hydrostatic-pressure induced flow maps, ionic current density maps in the presence and absence of electro-osmosis. On this basis, conclusions with respect to the similitude of transport patterns are feasible.

Studies of this sort are of interest for microsystem technology [33], [34]. Microsystem devices often consist of complex channel networks implying features of the model objects of the present study. Based on a structure producing closed-loop flow, cyclic electro-osmotic pumps without moving elements can be designed, for example. The intentional production of recirculation in such systems is essential for the function of microsystem mixers as discussed in Ref. [35].

The combined application of NMR microscopy techniques for the quantitative, non-invasive visualization of the total variety of hydro- and electrodynamics in the same channel system thus can be considered as a promising design tool for microsystems superior to conventional fluid dynamics techniques such as particle image, ultrasound Doppler or laser Doppler velocimetry [36], [37].

A remarkable result is the difference between the experimental ICD maps of the percolation cluster recorded with and without EOF, i.e. in ceramic and polystyrene model objects, respectively, of the same geometry (see Fig. 12, B and C). A substantial interference of hydrodynamic flow and electric current must be stated. Eddies of the electric current density were observed in the presence of EOF, but not in the hydrodynamically static case. This may be considered as a combined hydro- and electrodynamic phenomenon. A particle driven by hydrodynamic flow through an inhomogeneous electrostatic field effectively experiences a time-dependent electric field strength, $\vec{E} = \vec{E}(t)$, despite stationary flow and electrostatic conditions. There is a certain analogy to the “material” acceleration $\vec{a}_2 = (\vec{v} \cdot \vec{\nabla})\vec{v}$ known from the Navier/Stokes equation given in Eq. (4). That is, electrostatic laws are not applicable in the presence of EOF. Taking the EOF, ICD, and PIF experiments and simulations together, one can say that recirculation patterns occur with all transport quantities considered here, but at different positions of the percolation cluster.

In Ref. [9], an “electro-osmotic whirlwind” is predicted for highly conductive particles immersed in an electrolyte solution. This phenomenon is of a different nature and not comparable with the recirculation patterns found in our non-conducting systems. Using magnetic resonance imaging [11] and a pulsed field gradient NMR technique [12], electro-osmotic flow was studied experimentally in glass bead packs. Indications of cyclic flow are reported in the sense of ordinary hydrodynamic backflow similar to the findings in Section 4.1. Again, this is not to be confused with the vortex-like flow found in the present study.

Acknowledgments

We thank Hans Wiringer for cooperative assistance in the course of this study. This work was supported by the Deutsche Forschungsgemeinschaft.

References

[1] Buhai B., Kimmich R.: Phys. Rev. Letters **96**, 174501 (2006).

[2] Li D.: Electrokinetics in Microfluidics, London: Elsevier, 2004.

[3] Probstein R. F.: Physicochemical Hydrodynamics, New York: Wiley, 1994.

[4] Zhu W., Singer S.J., Zheng Z., Conlisk A.T.: Phys. Rev. E **71**, 041501 (2005).

[5] Yao S., Santiago J.G.: J. Colloid & Interface Sci. **268**, 133 (2003).

[6] Wu D, Chen A., Johnson C. S. Jr.: J. Magn. Reson. A **115**, 123 (1995).

[7] Manz B., Stilbs P., Jönsson B., Södermann O., Calaghan P.T.: J. Phys. Chem. **99**, 11297 (1995).

[8] Cummings E. B., Griffiths S. K., Nilson R. H., Paul P. H.: Anal. Chem. **72**, 2526 (2000).

[9] Rathore A. S., Horváth C.: J. Chromatogr. A **781**, 185 (1997).

[10] Wu R., Papadopoulos K. D.: Colloids and Surfaces A: Physicochemical and Engineering Aspects **161**, 469 (2000).

[11] Locke B. R., Acton M.: Gibbs, S. J., Langmuir **17**, 6771 (2001).

[12] Tallarek U., Rapp E., Scheenen T., Bayer E., Van As H.: Anal. Chem. **72**, 2292 (2000).

[13] O'Brien R. W.: J. Colloid Interface Sci. **110**, 477 (1986).

[14] Lab on a chip, RSC Journals

[15] Nguyen N. T., Hunag X., Chuan T. K.: Trans. of the ASME **124**, 384 (2002).

[16] http://www.schroederglas.com/download/MacorProduktbeschreibung

[17] https://www.plasticsportal.net/wa/EU/Catalog/ePlastics/doc/BASF/prodline/polystyrol/

[18] Klemm A., Kimmich R., Weber M.: Phys. Rev. E **63**, 041541 (2001).

[19] Stauffer D., Aharony A.: Introduction to Percolation Theory, London: Taylor and Francis, 1992.

[20] Morre J. H., Spencer D. N., Encyclopedia of Chemical Physics and Physical Chemistry, Volume I : Fundamentals, Bristol: IoP, 2001

[21] Patankar N. A., Hu H. H.: Anal. Chem. **70**, 1870 (1998).

[22] Alam J., Bowman J.C.: Theoret. Comput. Fluid Dynamics **16**, 133 (2002).

[23] FEMLAB: User’s Guide, Stockholm: Comsol AB, 2004.

[24] FLUENT: User’s Guide, Lebanon: Fluent Inc., 2000.

[25] Weber M., Kimmich R.: Phys. Rev. E **66**, 026306 (2002).

[26] Kimmich R.: NMR Tomography, Diffusometry, Relaxometry, Berlin: Springer, 1997.

[27] Kossel E., Buhai B., Kimmich R. in Stapf S., Han S.-I.(Edts): NMR Imaging in Chemical Engineering, Chap. **2.9**, Weinheim: Wiley-VCH, 2005.

[28] Kossel E., Kimmich R.: Magn. Reson. Imaging **23**, 397 (2005).

[29] Scott G. C., Joy M. L. G., Armstrong R. L., Henkelman R. M.: J. Magn. Reson. **97**, 235 (1992).

[30] Sersa I., Jarh O., Demsar F.: J. Magn. Reson. Series A **111**, 93 (1994).

[31] Ghiglia D. C., Pritt M. D.: Two dimensional phase unwrapping, New York: Wiley, 1998.

[32] Weber M., Kimmich R.: Phys. Rev. E **66**, 056301 (2002).

[33] Sinton D.: Microfluid Nanofluid **1**, 2 (2004)

[34] Takamura Y., Onoda H., Inokuchi H., Adachi S., Oki A., Horiike Y.: Electrophoresis **24**, 185 (2003).

[35] Chen H., Zhang Y.T., Mezic I., Meinhart C.D., Petzold L.: Proc. Microfluidics 2003 (ASME IMECE, 2003).

[36] Guyon E., Hulin J.-P., Petit L., Mitescu C. D.: Physical hydrodynamics, New York : Oxford University Press, 2001.

[37] Yan D., Nguyen N.T., Yang C., Huang X.: J. Chem. Phys. **124**, 021103 (2006).

Figure captions

Figure 1: Schematic illustration of the principle of electro-osmotic flow. A neutral electrolyte solution in contact with polar walls produces an *electrical double layer* at the surfaces. The wall surfaces become charged by dissociation of polar groups of the wall material. The surface charges are compensated by surplus counterions in the solution. At thermal equilibrium, this net charge density decays from the highest value in the immobile "compact layer" directly at the surface down to zero across the mobile "diffuse layer". In an electric field, the mobile surplus counterions in the diffuse layer are driven towards the co-electrode. That is, viscous friction between the surplus counterions and the solvent causes shear flow in the diffuse layer whereas the electrically neutral solution in the middle of the channel is characterized by a flat flow velocity profile. Note, that the electric double layer cannot be resolved neither in the NMR experiments nor in the computational fluid dynamics simulations.

Figure 2: Typical structures of quasi two-dimensional model objects investigated in this study. The top row shows an object with 7 parallel channels of various widths (0.8 mm, 1.2 mm, 1.6 mm, 2.0 mm, 2.4 mm, 2.8 mm, 3.2 mm). The channel length is 6 cm plus 2 x 0.7 cm for the input and output compartments where the electrodes are placed. The bottom row exhibits a random site percolation cluster as a paradigm for a more complex channel network. Isolated clusters were omitted. The size of the quadratic base lattice was 100 x 100. With a resolution of 400 μm, this corresponds to an object size of 4 cm x 4 cm without input and output compartments (not shown at the left and right-hand side, respectively). Column **(a)** shows computer generated templates used for the fabrication of the model objects. Photographs of these objects are rendered in the middle column **(b)**. After filling of the pore spaces of the objects with water, NMR spin density maps were recorded as shown in the right-hand column **(c)**. The maps correspond to a pixel matrix 256 x 256. The structural coincidence of the templates and the spin density maps demonstrates the quality both of the milling and of the NMR imaging processes. The regions marked by 1 and 2 refer to the detail plots in Fig. 14.

Figure 3: Left: Side view on an in- or output compartment of the seven-channel object shown in Fig. 2 (top row). Six identical quasi two-dimensional plates are stacked and encapsulated in a plastic container. In the case of the EOF and ICD mapping experiments, interdigitated comb

electrodes (right) are inserted in the compartments. The electrodes consist of gold plated copper.

Figure 4: Radio frequency (RF), magnetic field gradient (G_x, G_y, G_z), and ionic current pulse sequences used in the NMR mapping experiments in this study. A standard Hahn echo with the echo time T_E is acquired as the NMR signal of the liquid filled into the objects. **Spin density mapping (A)**: The combination with the gradient pulses in the schemes **(A)**, provides two-dimensional images (see Refs [26],[27], for instance) of a slice normal to the *z* direction, $\rho(x, y)$. The arrows indicate the direction of the increments in subsequent transients. The ramps of the gradient pulses are not shown for simplicity but are taken into account in the evaluations. **Mapping of the PIF velocity (A+B)**: Maps of the flow velocity components in the sensitive slice can be recorded by adding the gradient pulse pairs shown in **(B)** to the imaging part given in **(A)** (see Refs [26],[27], for instance) . That is, two three-dimensional experiments, x,y,v_x and x,y,v_y, are performed resulting in maps of the magnitude $v_{PIF}(x, y)$. **Mapping of the EOF velocity (A+B+C)**: In the absence of hydrostatic pressure gradients, flow can be generated by electro-osmosis arising in polar matrices by ionic currents applied perpendicular to the *z* direction as shown in scheme **(C)** [1]. The results are maps of the magnitude $v_{EOF}(x, y)$. The interval t^* represents the time necessary to achieve the steady state and is given in Eq. (11). $T_{EOF} > T_E$ is the total length of the current pulse. The current acts during the whole echo time, so that no phase shifts directly induced by the current arise. The only phase shifts relevant in EOF velocity mapping are those due to spatial and velocity encoding. In order to reverse electrode reactions, identical current pulses of opposite polarity are applied during the recycle delay as indicated on the right-hand side of row **(C). Mapping of the ICD (A+D)**: In samples invariant along the *z* axis, two-dimensional current density maps of the *x/y* plane, $j(x, y)$, can be recorded based on the phase shifts produced by sequence **(D)** [25]. T_C is the total application time of ionic currents. Note that, in contrast to the EOF pulse scheme **(C)**, the phase shifts induced by the current pulses before and after the 180° RF pulse do not cancel each other owing to the bipolarity. Apart from this, the polarity is alternated in subsequent scans while subtracting the current densities from each other according to $j_{x,y} = \left(j_{x,y\pm} - j_{x,y\mp} \right) / 2$. In this way, undesired offsets are eliminated. Note that all maps mentioned can be recorded in the same object just by choosing the appropriate pulse sequence.

Figure 5: Simulation of EOF streamlines in a two-dimensional tube with closed electrodes at the ends. A negative zeta potential is assumed at the walls. In the enlarged area, flow velocity vectors are shown indicating the flow directions.

Figure 6: Simulation of EOF streamlines in parallel circuits of two-dimensional channels with closed (i.e. impermeable) **(a)** and open (i.e. permeable) electrodes **(b)**. The ratio of the channel widths is assumed to be $d_a / d_b = 4$. The zeta potential of the wall material is assumed to be negative. The directions of the flow velocities are shown in the enlarged areas of Fig. (a). The main flow directions are indicated by the bold arrows. The cyclic character of the main flow direction in the closed system (a) as a consequence of hydrodynamic backflow can be exploited for cyclic micropump applications in microsystem technology. This is in contrast with the open system (b) where the flow direction in both channels is uniform.

Figure 7: Simulation of EOF streamlines in a closed system of seven two-dimensional parallel channels of varying widths (see Fig. 2, top row). The zeta potential of the matrix was assumed to be negative. The vector representation of the enlarged area shows that the main flow direction depends on the width of the channel owing to hydrodynamic backflow.

Figure 8: Experimental EOF velocity map of the seven-channel object shown in Fig. 2 (top row). A simulation of EOF in this geometry can be found in Fig. 7. Flow velocities are represented according to the grey shade bar at the bottom left. The velocities in the central area are rendered in vector representation on the right-hand side. The main flow direction is indicated by bold arrows. It depends on the width of the channels. The velocity could be mapped reliably only in 5 channels owing to the limited resolution. The mean electric field strength was 150 V/cm.

Figure 9: Mean EOF velocity, $< v_{y,EOF} >$, along the channel axes as a function of the channel diameter, d. The parameter is the voltage U across the seven-channel object shown in Fig. 2 (top row). Note the crossover between positive and negative velocity components at medium channel diameters as visualized in Fig. 8. The different slopes with different voltages indicate that the cyclic flow is enhanced by stronger voltages. **(b)** Comparison of simulated and measured data of the mean EOF velocity along the channel axes. The slopes are similar, but

the deviation between the two data sets is due to the fact, that the simulation refers to a two-dimensional system without electro-osmotic driving forces at the bottom and at the top.

Figure 10: **(a)** Experimental EOF velocity maps in an open three-electrode configuration for two different polarities of the applied voltages. The reservoirs at which the electrodes are placed are indicated by the bar-like compartments. The electrostatic potentials at the electrodes are given relative to the electrode at the top. The main EOF direction follows the steepest electrostatic potential gradient. Reversing the polarity of the right-hand electrode changes the mean flow direction as indicated by the curved arrows. The gray shade code of the EOF velocity is given at the bottom. **(b)** Vector representation of the detail areas marked by the dotted squares in (a). **(c)** Computer simulations of the EOF velocity distribution in two dimensions under otherwise equivalent conditions.

Figure 11: Simulated maps of the magnitudes of different transport quantities in the two-dimensional percolation cluster shown in Fig. 2 bottom. The marked areas are detailed on the right-hand side in vector representation. The matrix is rendered in gray. The electrodes are not shown for simplicity. **(A)** Electric current density, j, in the absence of EOF (i.e. for a non-polar matrix). **(B)** EOF velocity, $v_{\mathrm{EOF,open}}$, in an open polar matrix, i.e. with permeable electrodes. The electric field strength is assumed to be 83 V/cm. **(C)** EOF velocity, $v_{\mathrm{EOF,closed}}$, in a closed polar matrix. The electrodes are assumed to be impermeable. **(D)** Flow velocity, v_{PIF}, caused by a hydrostatic pressure gradient in the open system.

Figure 12: Experimental maps of the magnitudes of different transport quantities measured in quasi two-dimensional percolation model objects as shown in Fig. 2 bottom. The field-of-view is 4 cm x 4 cm. The matrix is rendered in black. The marked areas of 0.8 mm × 0.8 mm are detailed on the right-hand side in vector and in trajectory representation. The latter means that the velocity vector arrows are bent along the local streamlines, and the length of the curvilinear vectors is proportional to the mean magnitude along the arrow. **(A)** EOF velocity, v_{EOF}, in the polar matrix. The electric field strength was 83 V/cm. **(B)** Electric current density in the presence of EOF, j_{EOF} (polar matrix). **(C)** Electric current density in the absence of EOF, j (non-polar matrix). **(D)** Flow velocity caused by an external pressure gradient in the open system, v_{PIF}. Typical maximum values for the velocity and electric current density are $v_{max} = 4.5$ mm/s and $j_{max} = 5$ mA/mm^2, respectively.

Figure 13: Verification of the Helmholtz/Smoluchowski equation (see Eq. (5)) for EOF in the percolation cluster shown in Fig. 2 (bottom). The mean magnitude of the flow velocity is plotted versus the voltage across the cluster of size 6 cm (electrode distance). Both the simulated (squares) and the experimental (circles) data can be described by a linear function (solid straight line). This line is compatible with a zeta potential of about -100 mV. The conductivity of the electrolyte solution ($CaCl_2$) was 2.44×10^{-4} S/m.

Figure 14: Vortices of different transport quantities in 0.8 mm x 0.8 mm areas at positions 1 or 2 of the percolation cluster shown at Fig. 2 c, bottom. **(A)** Two-dimensional simulation of the flow velocity, $\vec{v}_{PIF}$, driven by an external pressure gradient at position 1 in vector representation. **(B)** Experimental EOF velocity, v_{EOF}, at position 2 in trajectory representation. **(C)** Experimental electric current density, j_{EOF}, in the presence of EOF at position 2 again in trajectory representation.

Figure 15: Comparative simulations of the relative PIF and ICD transport quantities $j_{ICD} / j_{\max}$ and $v_{PIF} / v_{\max}$, respectively, in a two-dimensional test structure consisting of 10 parallel channels of varying widths *d* but identical thickness. A similar object is shown in Fig. 2 top. The ICD data can be described by a linear function of *d*, whereas the PIF data follow a d^3 law.

Figure 16: Simulations of two-dimensional random site percolation networks with porosities ranging from p=0.55 (below the threshold value p_c=0.5962) to p=1 (no obstacles). The top row represents the computer generated networks with the pore space in white. The bottom row shows EOF velocity maps in streamline representation, where the matrix is not shown again.

Figure 17: Simulated mean EOF velocity magnitude versus the porosity of closed two-dimensional random-site percolation clusters. The data have been evaluated from EOF velocity maps such as shown in Fig. 16 bottom. The crossover at the percolation threshold is obvious.

Figure 18: Histograms of the EOF velocity magnitude simulated in closed random-site percolation clusters of various porosities (see Fig. 16). Above the percolation threshold, the

data refer to the percolating cluster, below to all isolated clusters. The histograms of isolated clusters and of percolating clusters far above the percolation threshold do not show the power law regime (solid line) characteristic for percolating clusters for $p \approx p_c$.

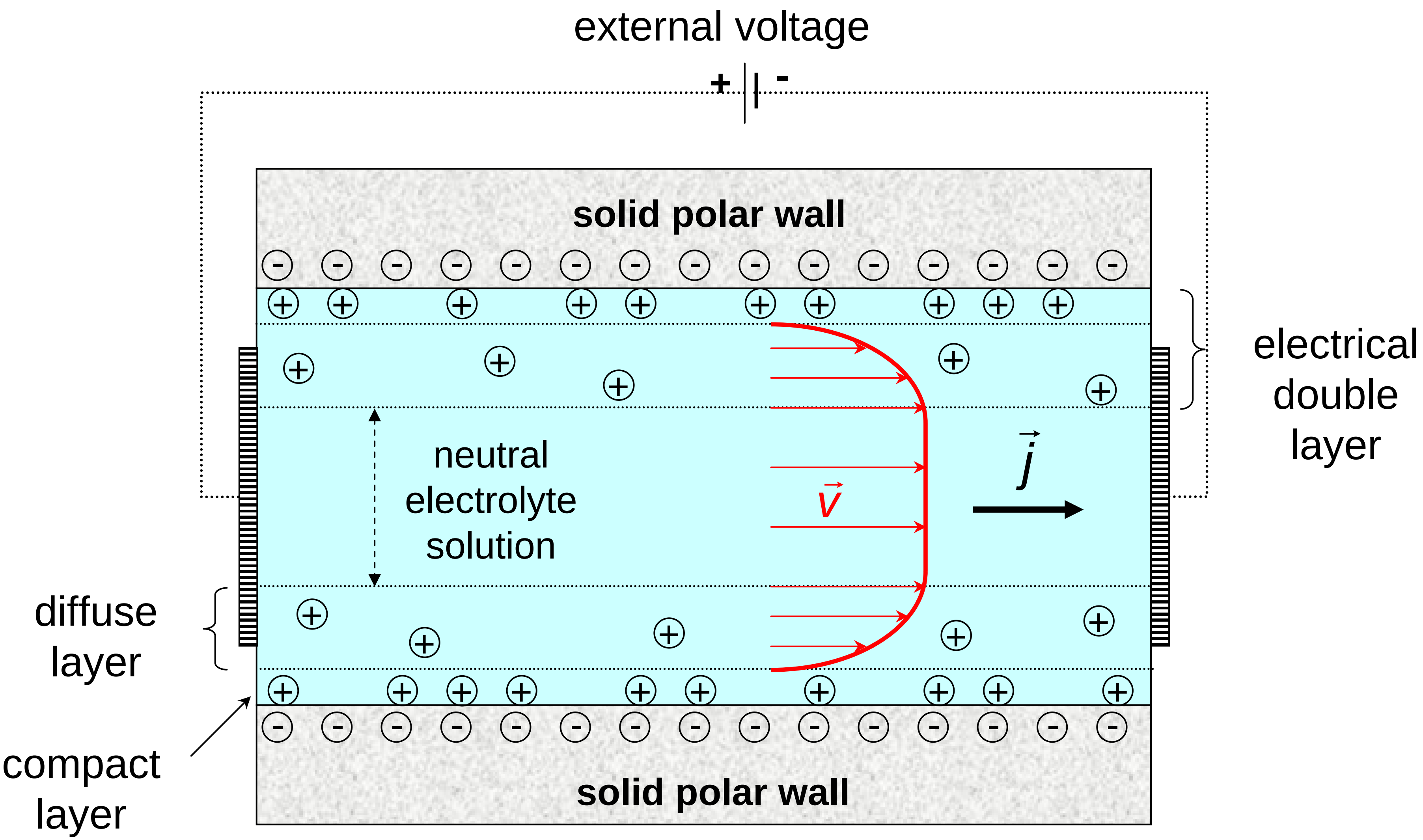
external voltage
+
-
solid polar wall
electrical double layer
neutral electrolyte solution
$\vec{v}$
$\vec{j}$
diffuse layer
compact layer
solid polar wall

Fig.1

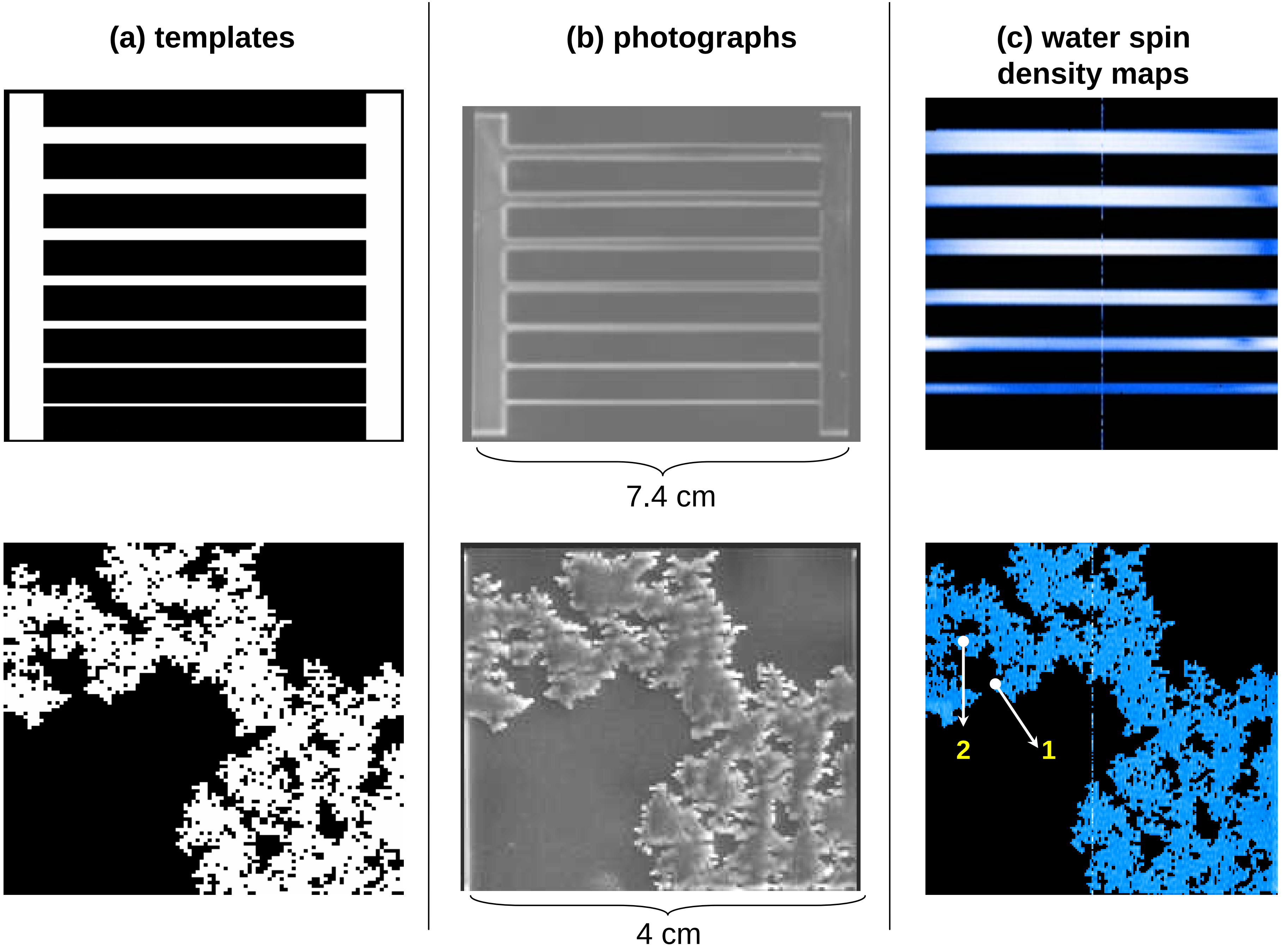
(a) templates
(b) photographs
(c) water spin density maps
7.4 cm
2
1
4 cm

Fig. 2

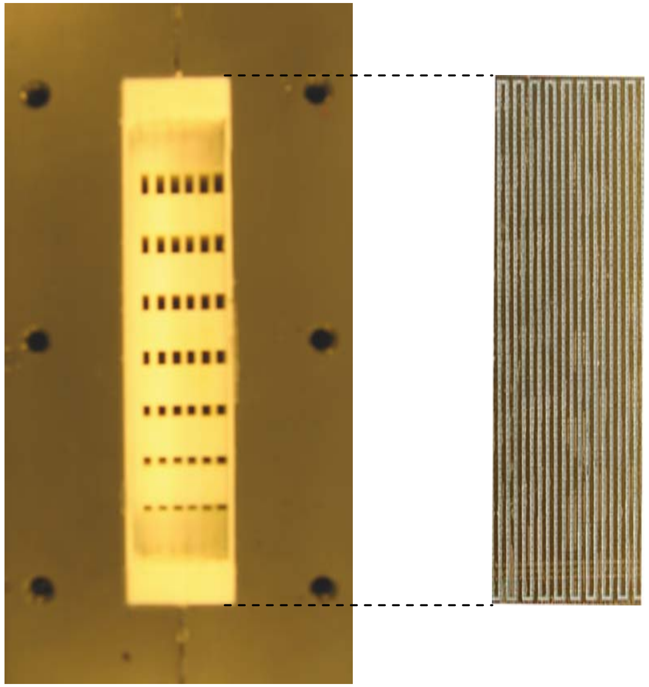

Fig. 3

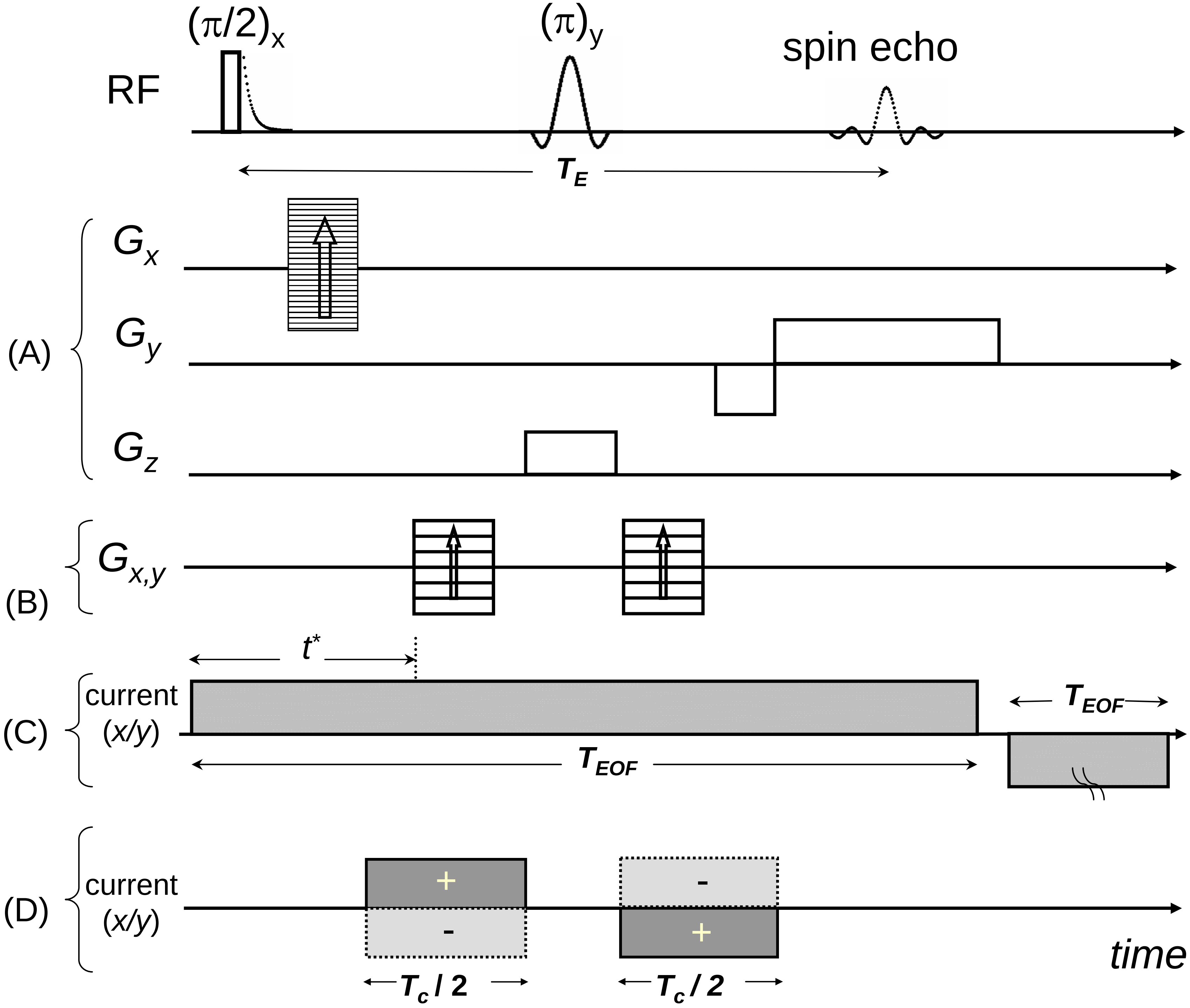

(π/2)x
(π)y
spin echo
RF
TE
Gx
Gy
(A)
Gz
Gx,y
(B)
t*
current
(x/y)
(C)
TEOF
TEOF
+
-
-
+
current
(x/y)
(D)
time
Tc / 2
Tc / 2

Fig. 4

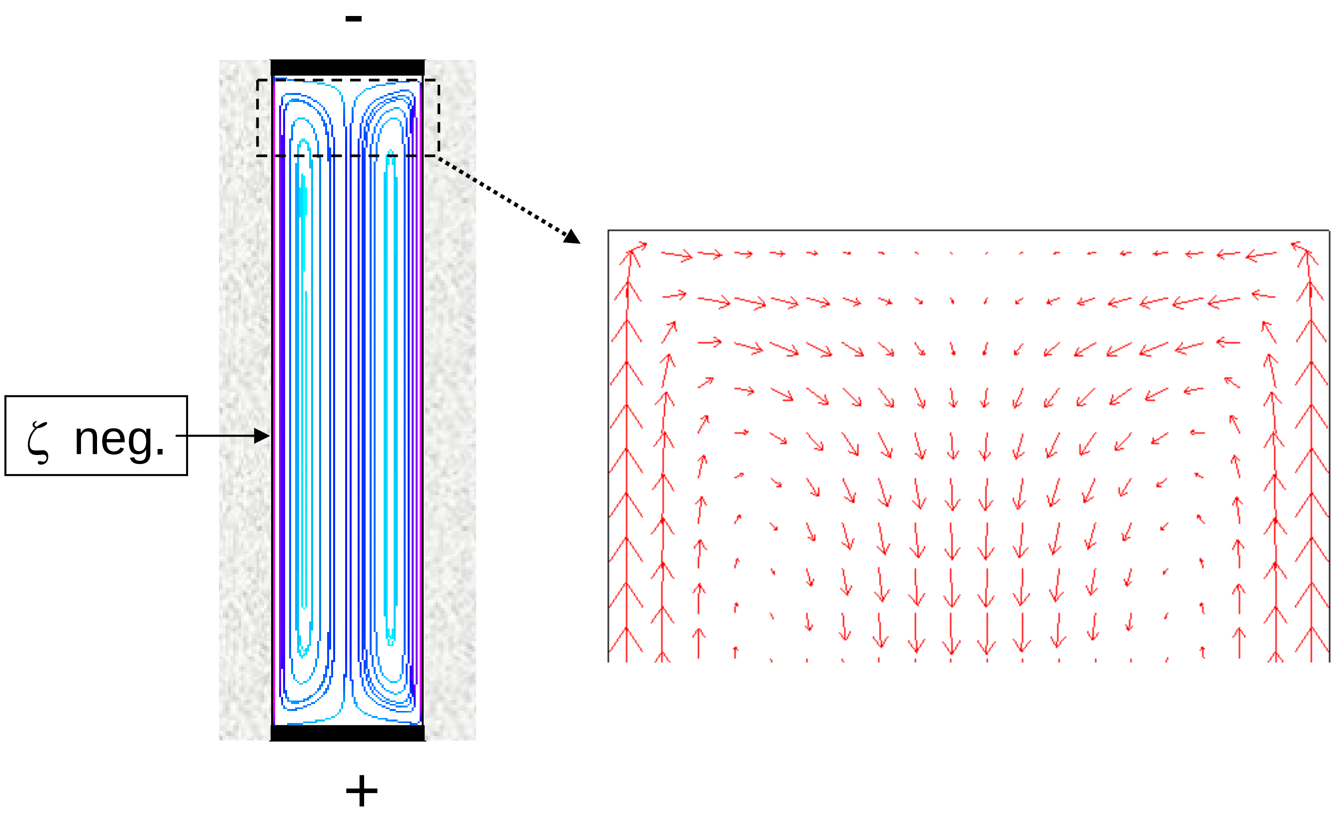

Fig. 5

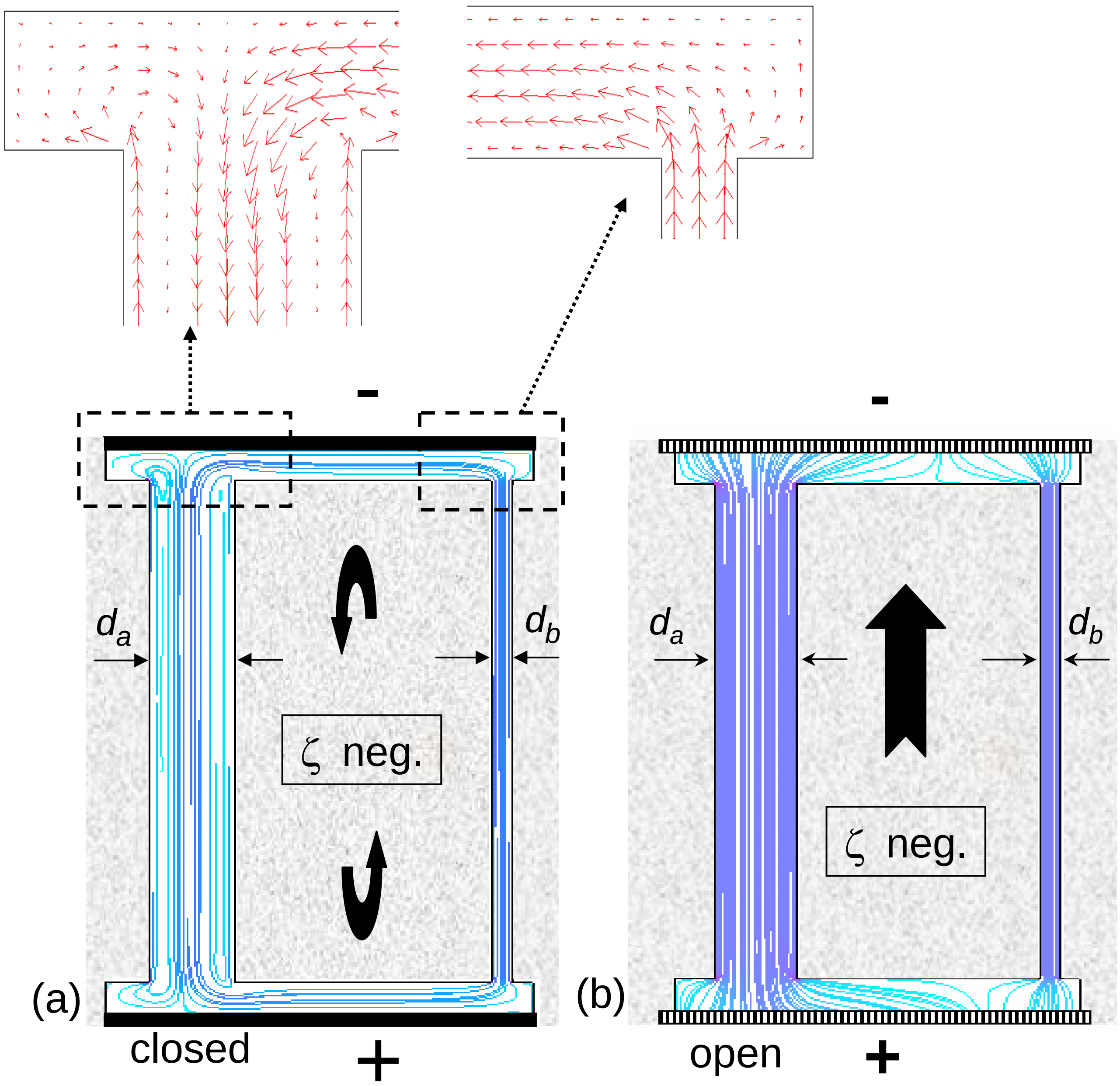
-
(a)
closed
+
d_a
d_b
ζ neg.
-
(b)
open
+
d_a
d_b
ζ neg.

Fig. 6

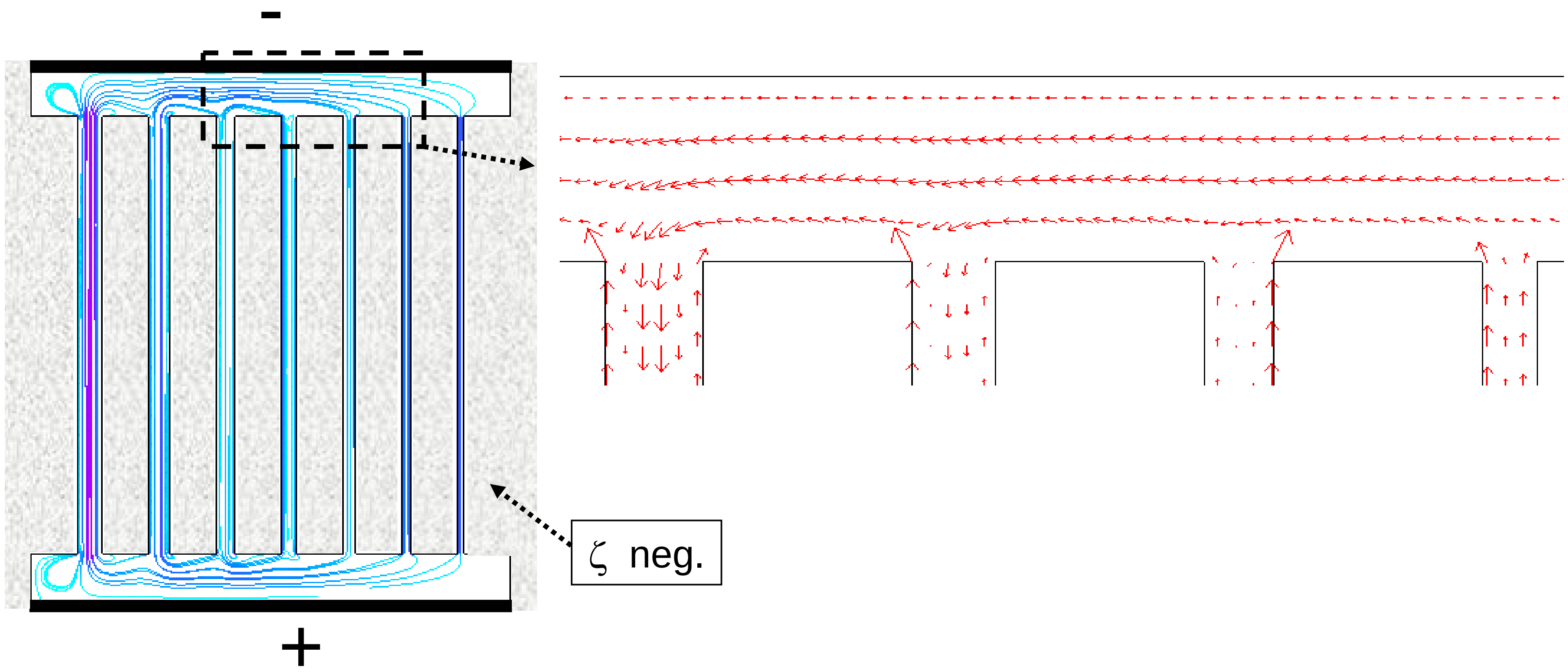

Fig. 7

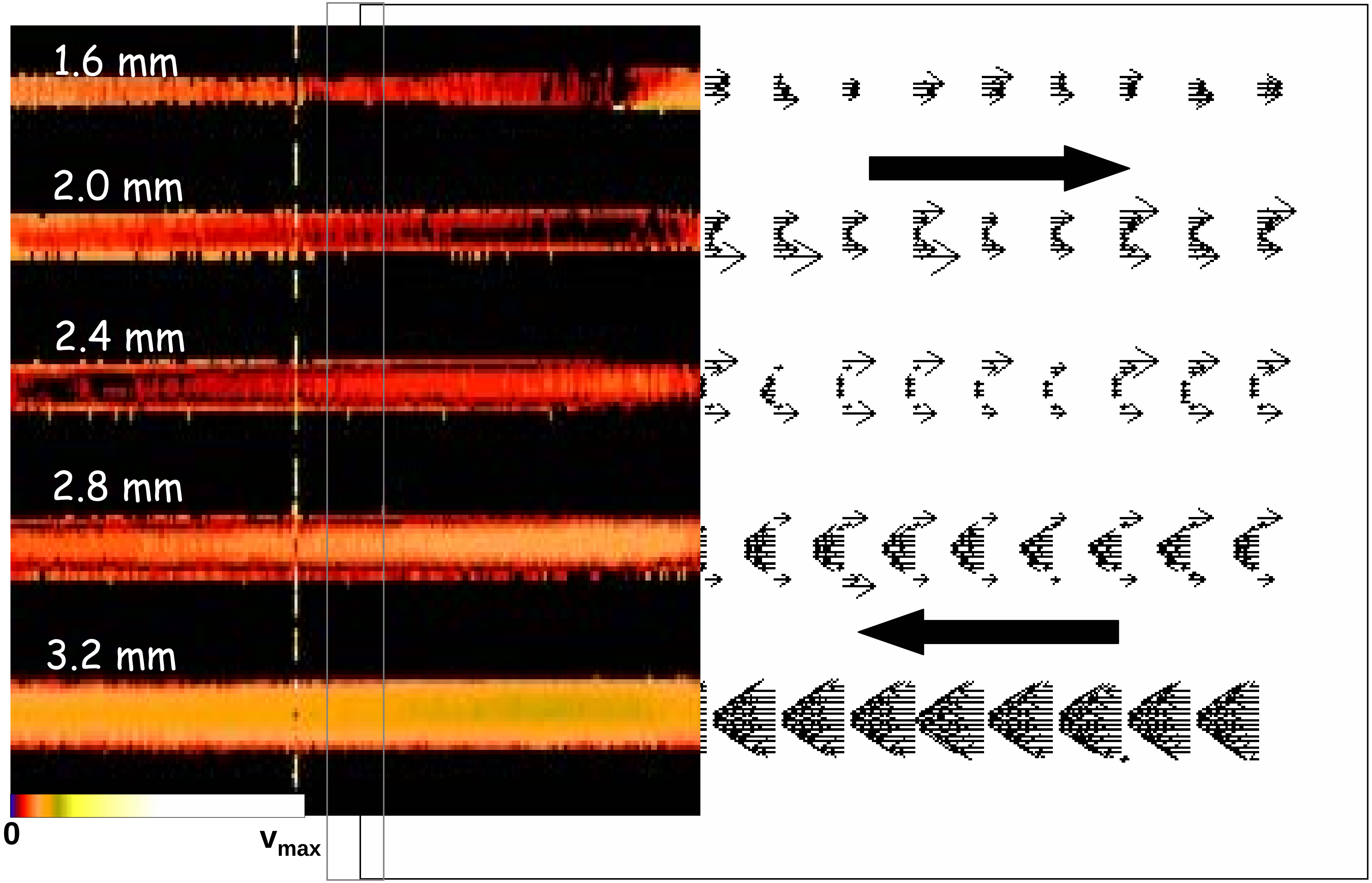

Fig. 8

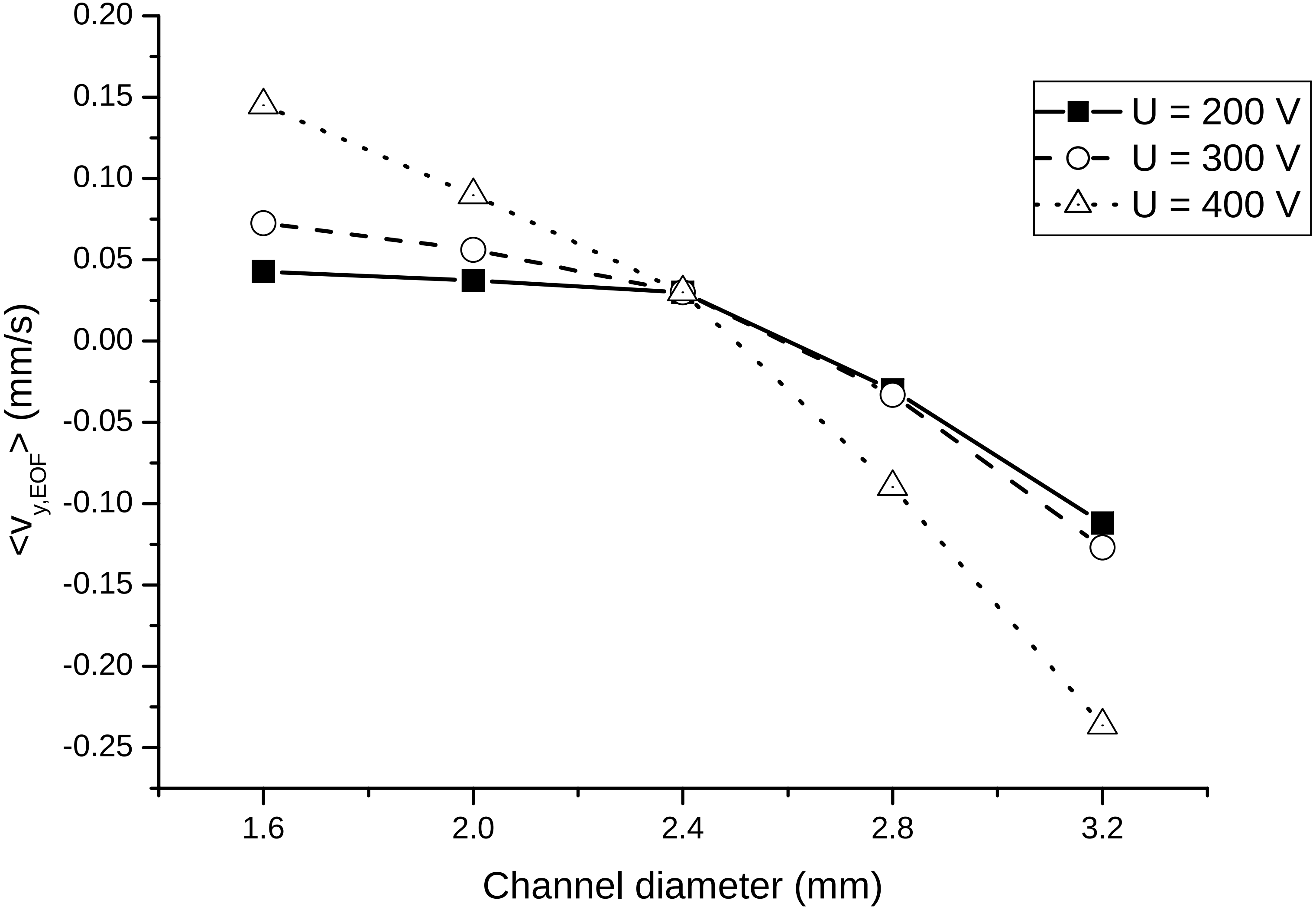
0.20
0.15
0.10
0.05
0.00
-0.05
-0.10
-0.15
-0.20
-0.25
<v_y,EOF> (mm/s)
1.6
2.0
2.4
2.8
3.2
Channel diameter (mm)
U = 200 V
U = 300 V
U = 400 V

Fig. 9a

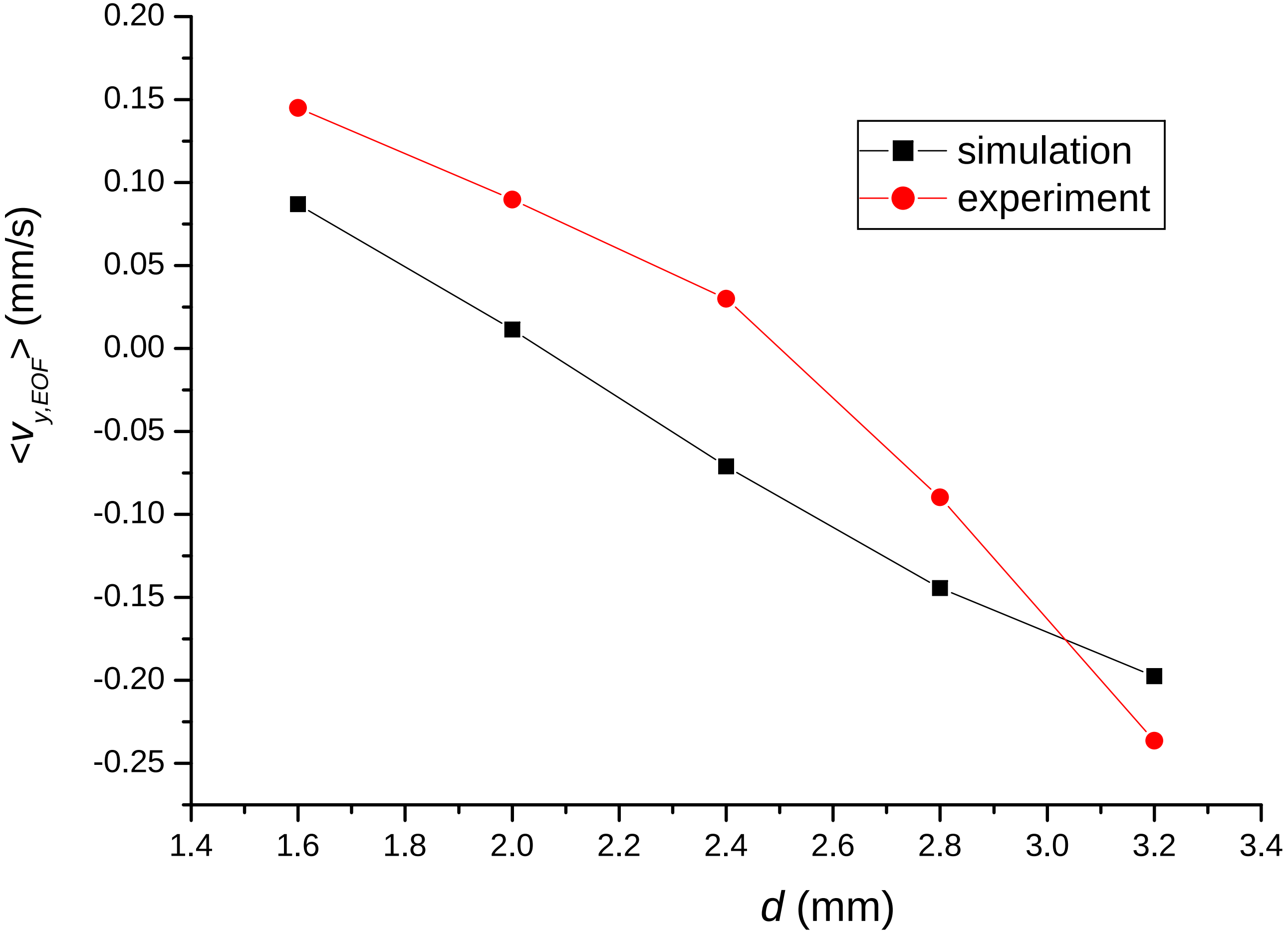
0.20
0.15
0.10
0.05
0.00
-0.05
-0.10
-0.15
-0.20
-0.25
$<v_{y,EOF}>$ (mm/s)
1.4
1.6
1.8
2.0
2.2
2.4
2.6
2.8
3.0
3.2
3.4
d (mm)
simulation
experiment

Fig. 9b

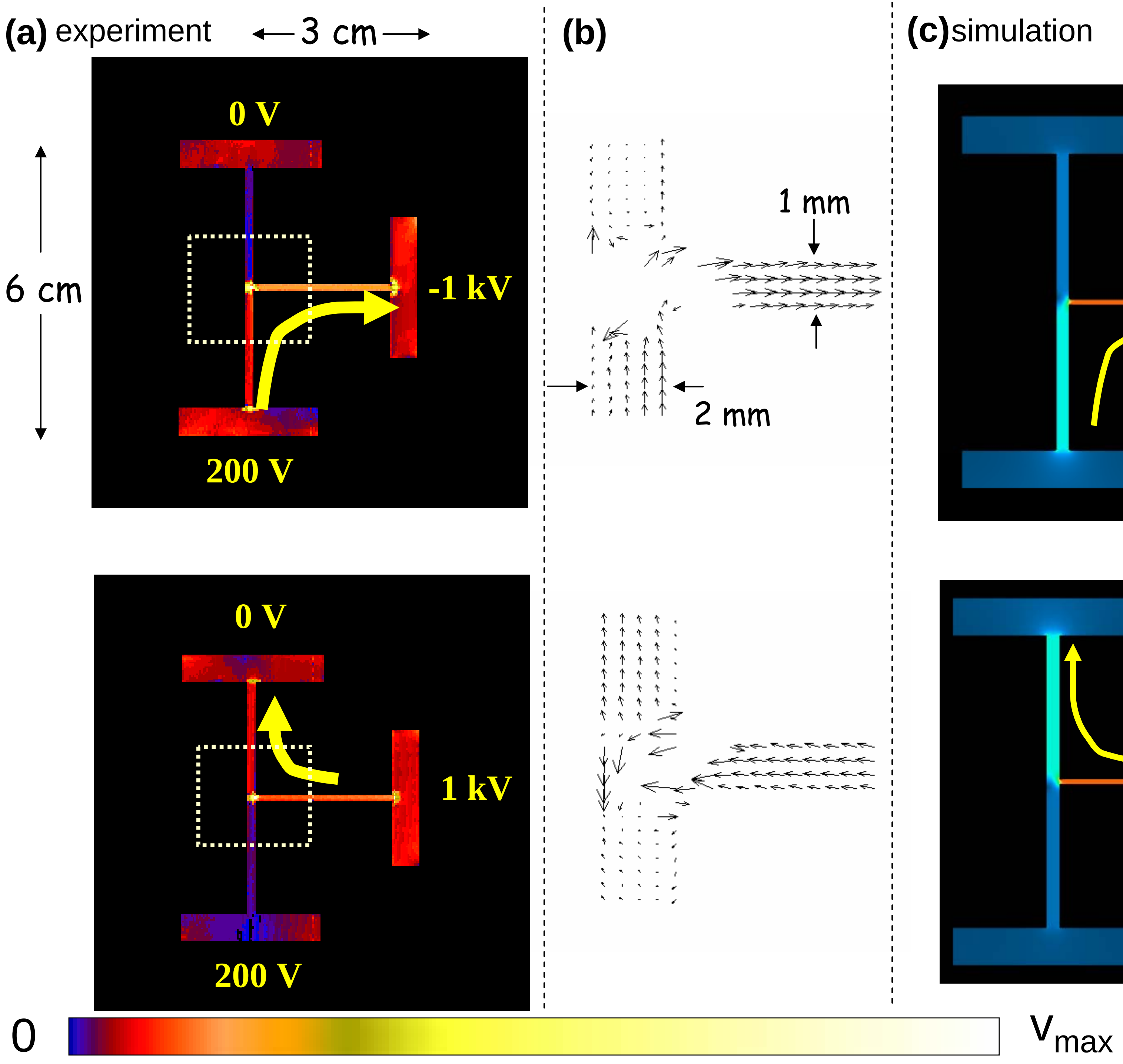
(a) experiment
3 cm
6 cm
0 V
-1 kV
200 V
0 V
1 kV
200 V
(b)
1 mm
2 mm
(c)simulation
0
V_{max}

Fig. 10

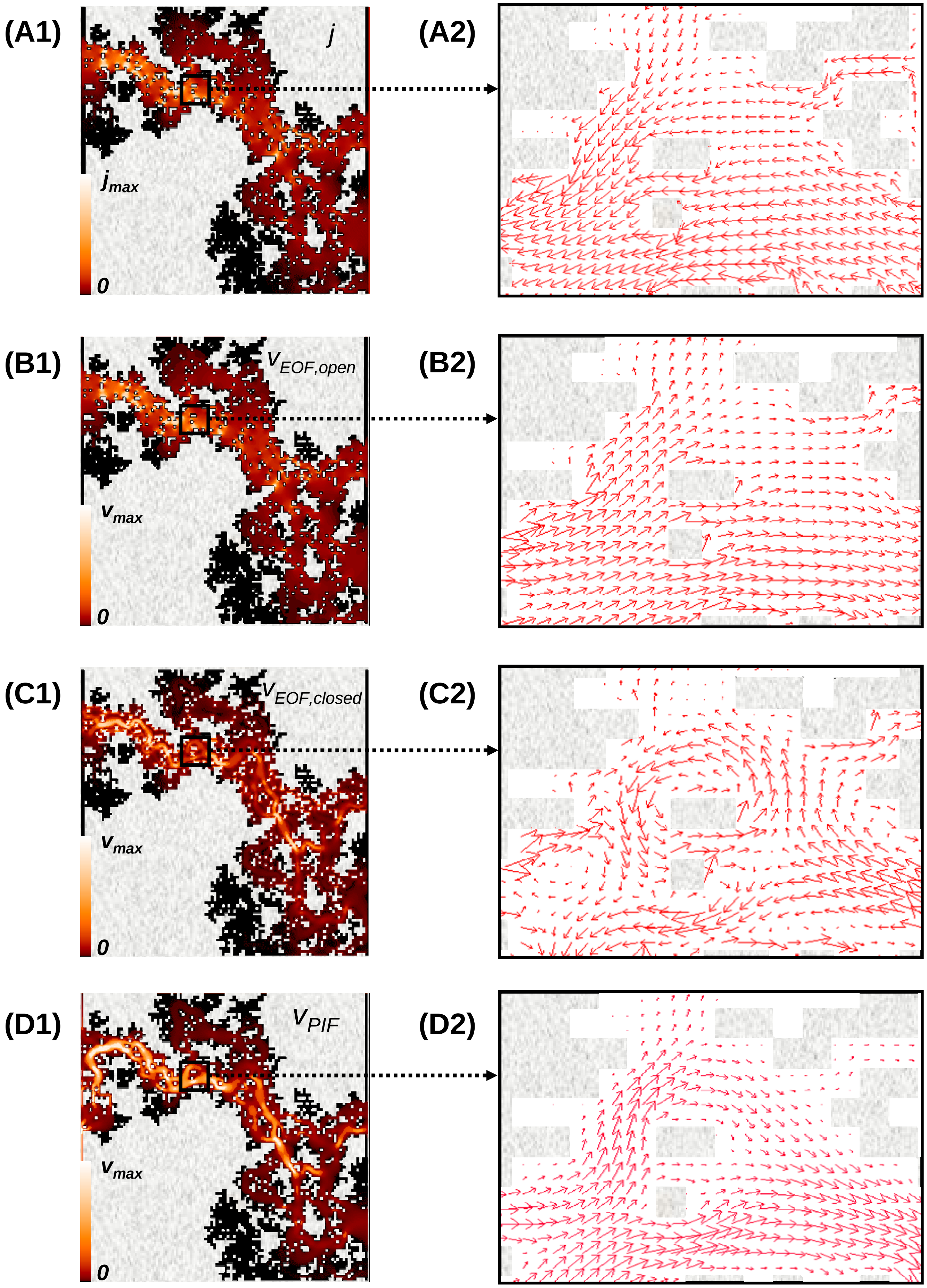
(A1)
j
j_max
0
(A2)
(B1)
V_EOF,open
v_max
0
(B2)
(C1)
V_EOF,closed
v_max
0
(C2)
(D1)
V_PIF
v_max
0
(D2)

Fig. 11

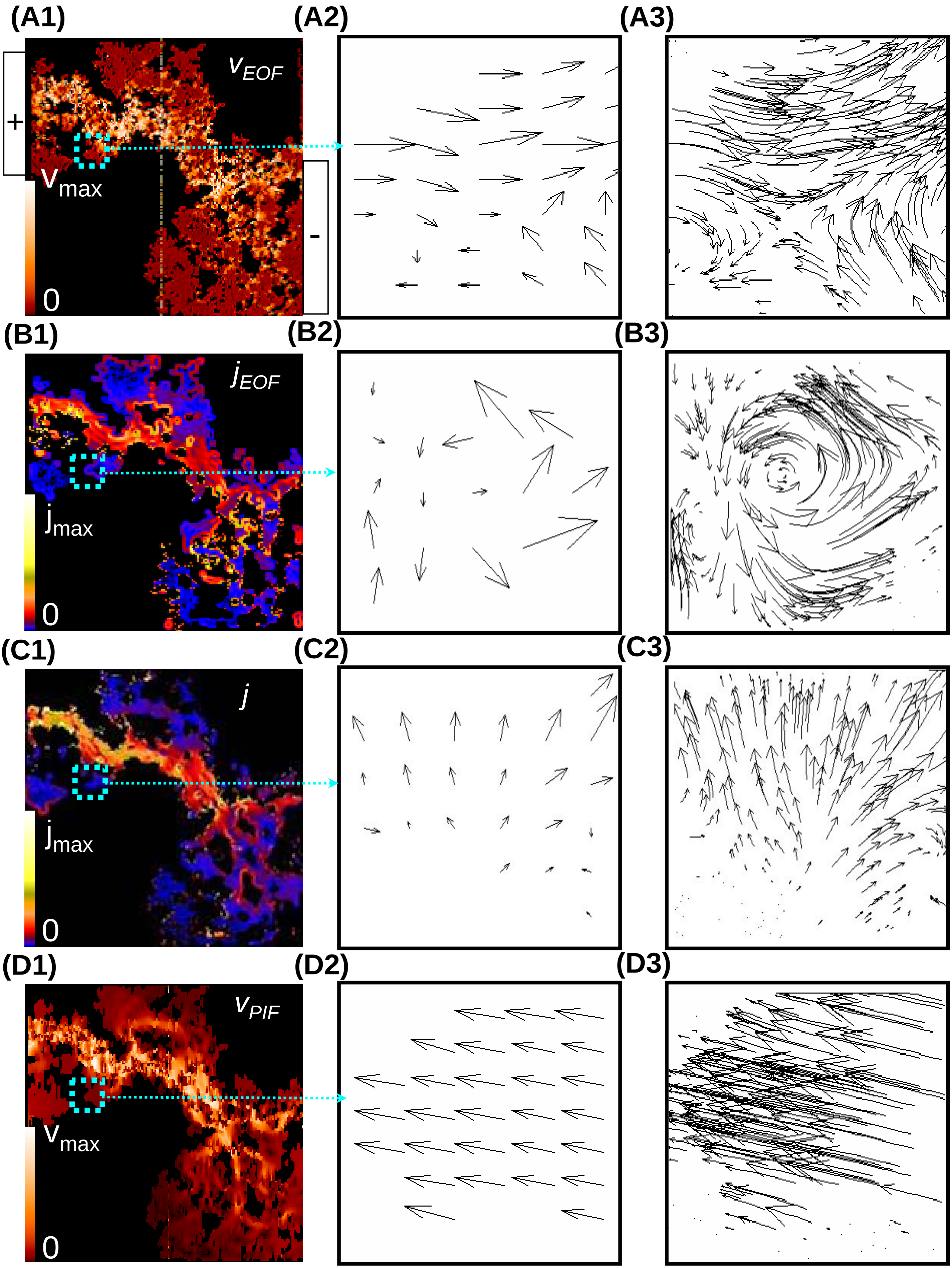
(A1)
(A2)
(A3)
v_{EOF}
+
-
v_{max}
0
(B1)
(B2)
(B3)
j_{EOF}
j_{max}
0
(C1)
(C2)
(C3)
j
j_{max}
0
(D1)
(D2)
(D3)
v_{PIF}
v_{max}
0

Fig. 12

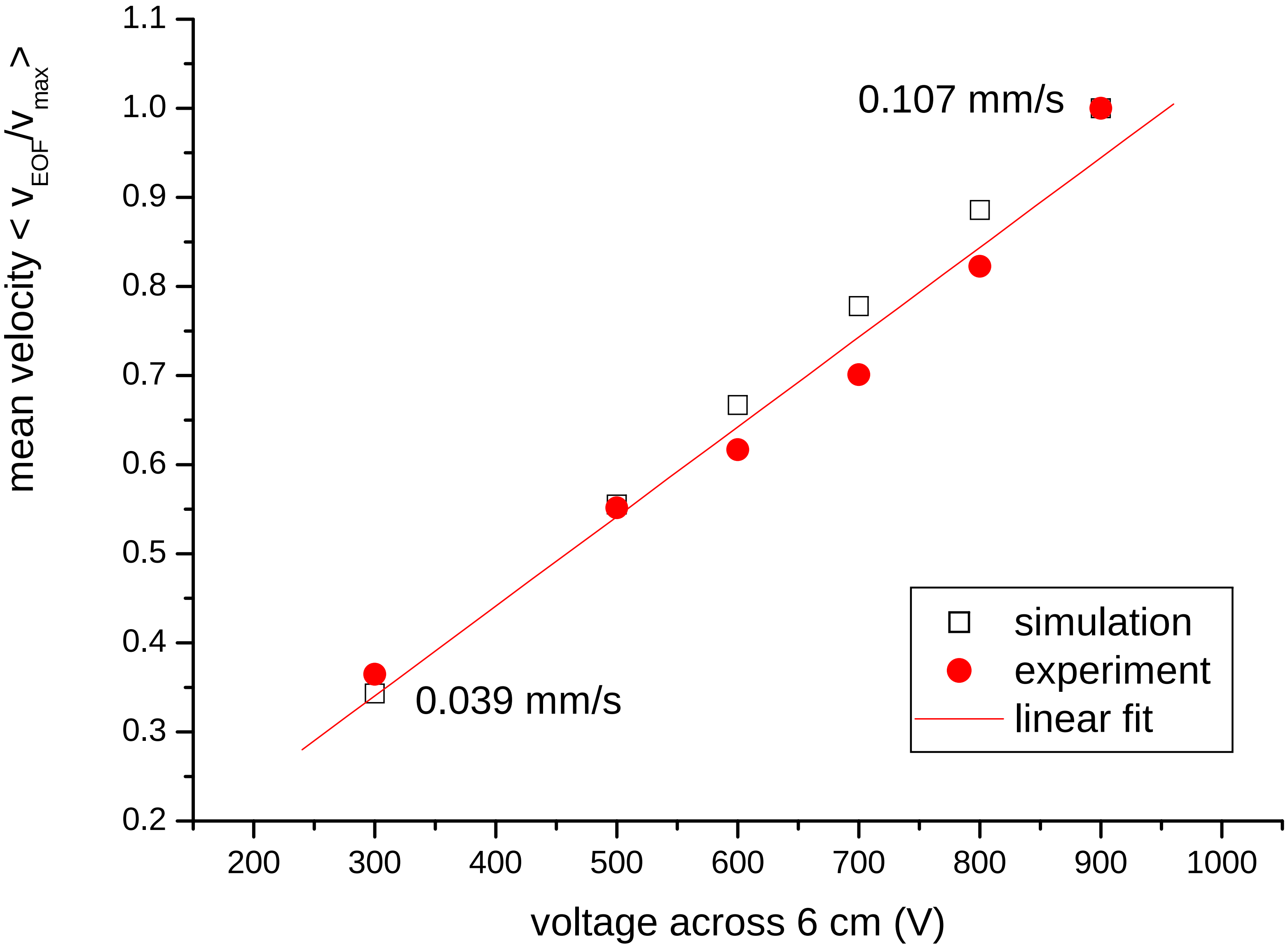
mean velocity $< v_{EOF}/v_{max} >$
1.1
1.0
0.9
0.8
0.7
0.6
0.5
0.4
0.3
0.2
200
300
400
500
600
700
800
900
1000
voltage across 6 cm (V)
0.107 mm/s
0.039 mm/s
□ simulation
● experiment
linear fit

Fig. 13

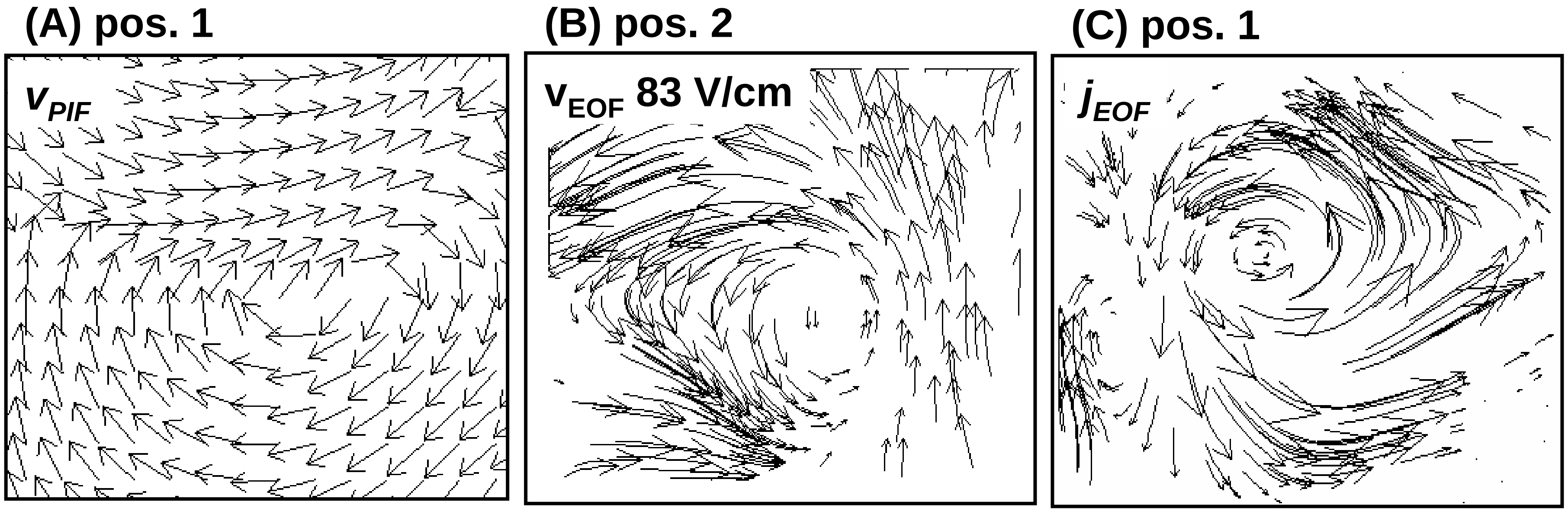
(A) pos. 1

(B) pos. 2

(C) pos. 1

Fig. 14

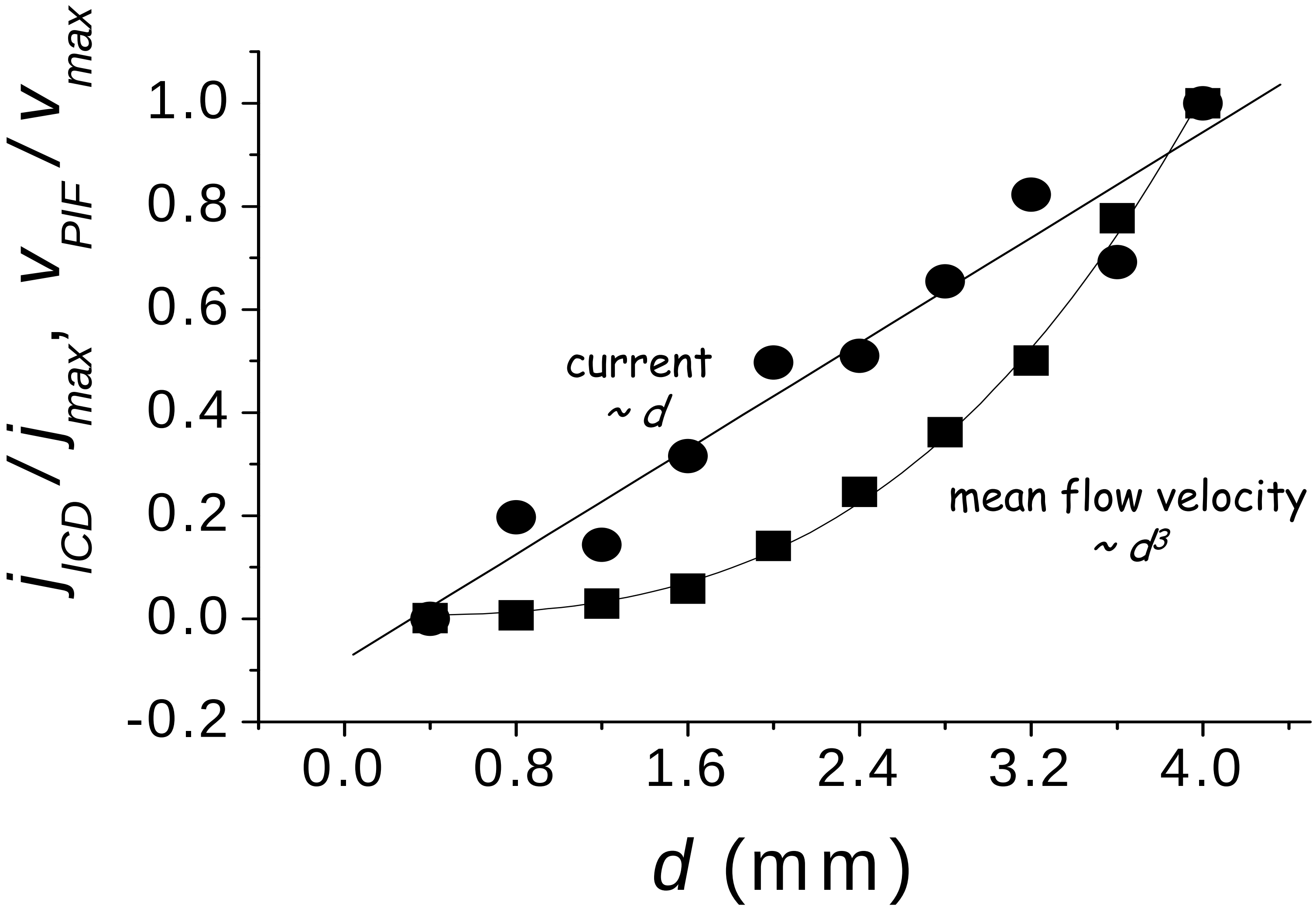
j_{ICD} / j_{max}, v_{PIF} / v_{max}
1.0
0.8
0.6
0.4
0.2
0.0
-0.2
0.0
0.8
1.6
2.4
3.2
4.0
d (mm)
current
~ d
mean flow velocity
~ d^3

Fig. 15

random site percolation networks ($p_c = 0.5962$)

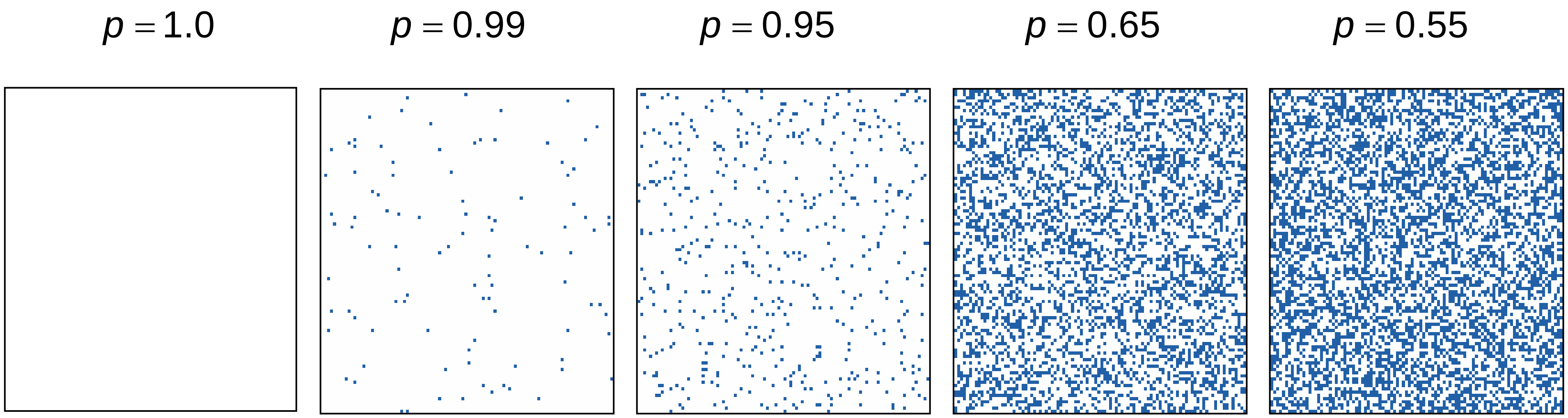
$p = 1.0$
$p = 0.99$
$p = 0.95$
$p = 0.65$
$p = 0.55$

EOF streamlines (sim.)

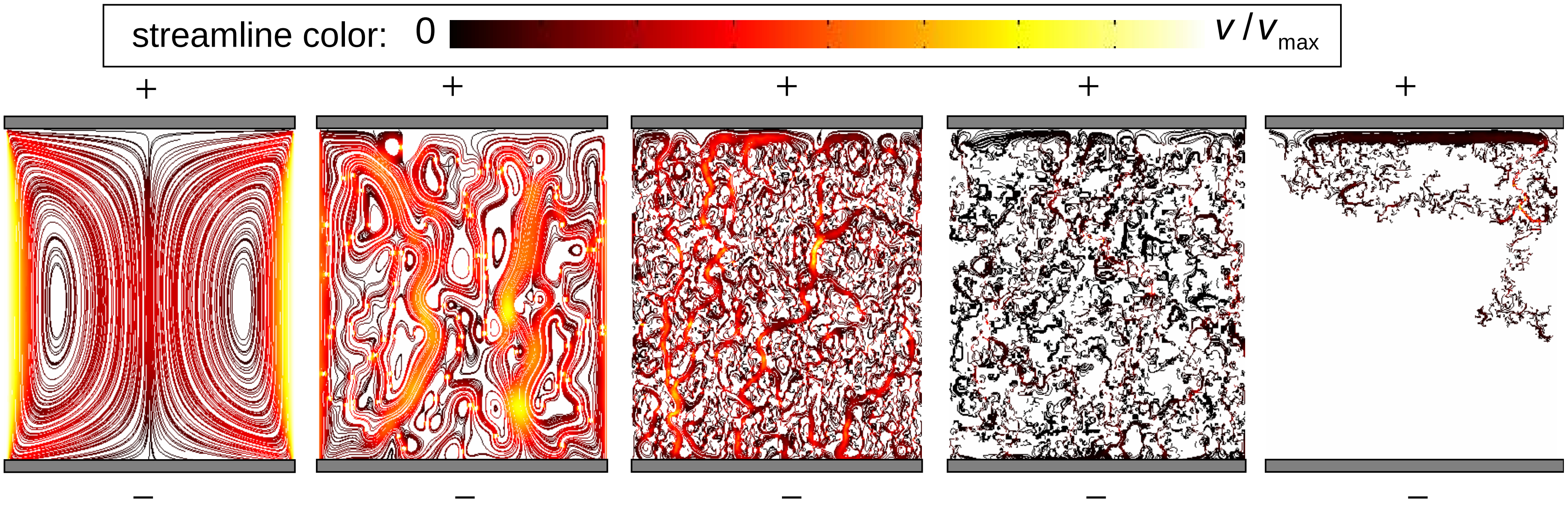

Fig. 16

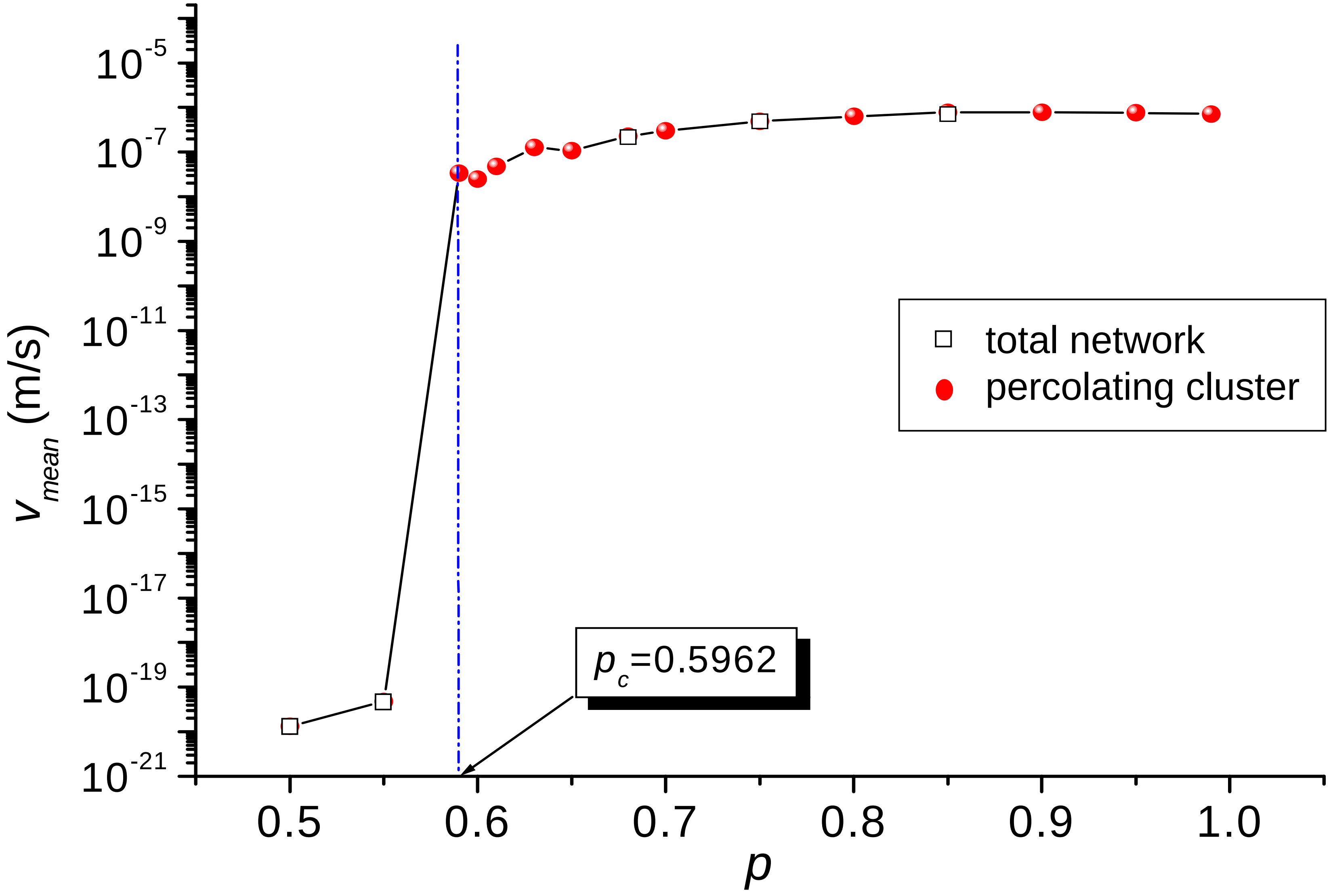
10^{-5}
10^{-7}
10^{-9}
10^{-11}
10^{-13}
10^{-15}
10^{-17}
10^{-19}
10^{-21}
v_{mean} (m/s)
0.5
0.6
0.7
0.8
0.9
1.0
p
□ total network
● percolating cluster
p_c=0.5962

Fig. 17

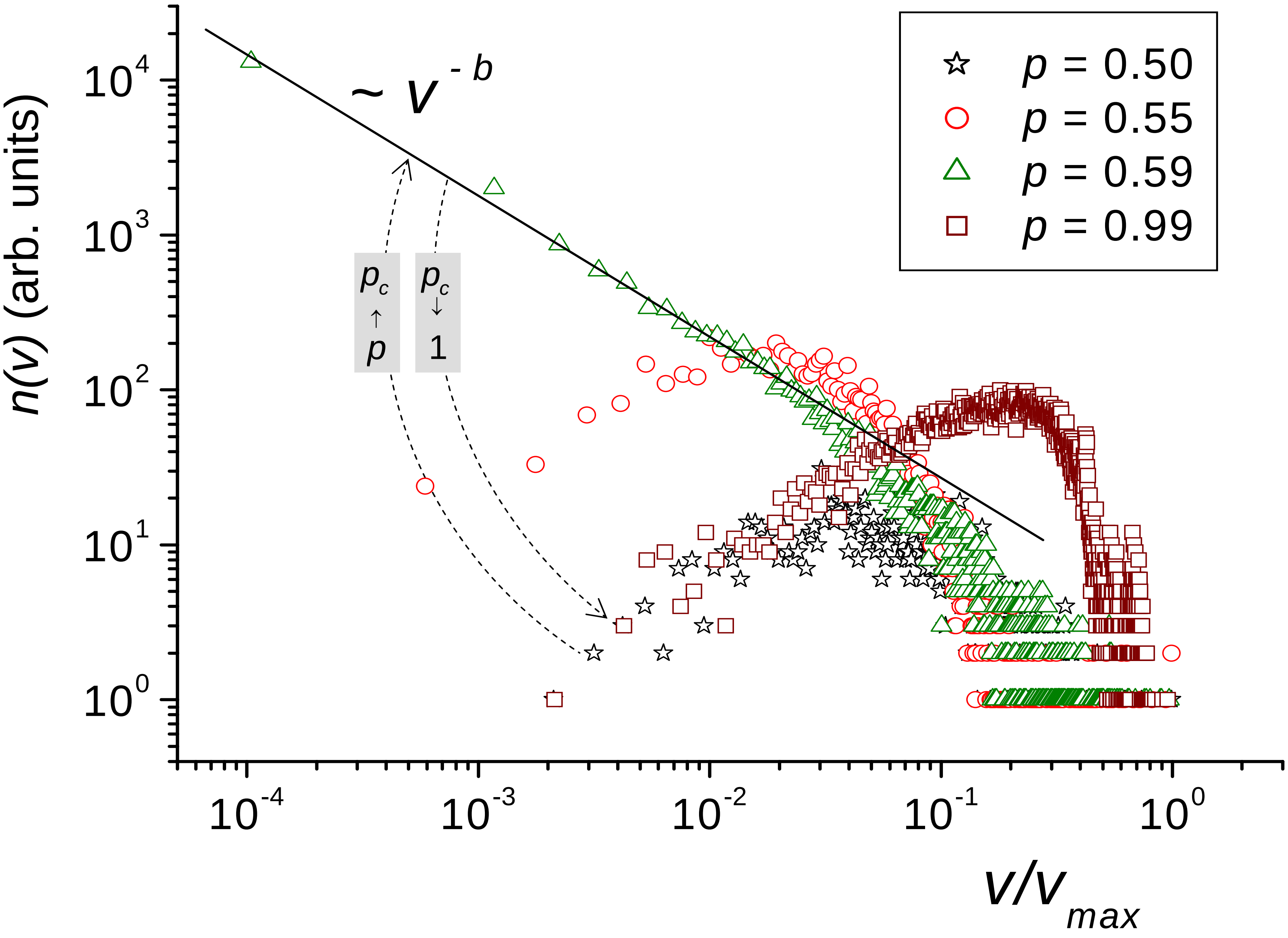

n(v) (arb. units)
10^4
10^3
10^2
10^1
10^0
10^-4
10^-3
10^-2
10^-1
10^0
v/v_max
~ v^-b
p_c ↑ p
p_c ↓ 1
☆ p = 0.50
○ p = 0.55
△ p = 0.59
□ p = 0.99

Fig. 18

Acknowledgements

Five years ago I started my PhD thesis here in the Sektion Kernresoanzspektroskopie. For starting I have to give all my thanks to Prof. Ardelean Ioan from Technical University of Cluj-Napoca, Romania. I hope that I fulfilled his trust all over these years.

The other person whom I have to thanks is Prof. Dr. Rainer Kimmich. My Doktorvater here in Ulm for 5, now short, beautiful years. We accomplish a lot together. I also want to thank him especially for the opportunity which he gave me to come in closed contact with the students. I hope I did my job as Übungsleiter as he expected.

My thoughts were or course always with my family there in Romania. My father Alexandru, my mother Ana (she always wanted a doctor in the family), my brother Alexandru-Ioan, and of course my grandmother, Rozalia. They have been always a strong support for me. Of course that I have to mention the newest members of the family: my wife's brother Eliza and the two beautiful children of them, Alexandra and Rares-Bogdan.

My specials friends and colleges here in Ulm: Christoph, mein Mitbewohner- do not worry – once we will have our restaurant. Patrick and his family, Robert and all my friends from Sunday, the Romanian football team: Joseph, Detlef, Rares, Horst, and all the others.

The technical support was here at the University of Ulm of five stars. I have to thank first to our technician Hans Wiringer – he took always care of my computers and not only. My special friend from the Elektronikwerkstatt, Herr Robert Sproll – we had good times and made good work together and for that I am thankful. My friend from the Mechanikwerkstatt – Herr Feierabend and Herr Gruchmann. Do not forget the Galvanikmesiter. All of them thank you! Without you I would be lost!

I thanks also to all actual and former members of the Sektion: Frau Kast, Birgitt, Carl-Heinz, Esteban, Germann, Elke, Markus, Atilla, Elmar, Farida, Siddarth, Surijani,

I will always remember the fantastic Heidi Group: Carlos – my best friend here at the university, Markus and Ravinath. How much money we spend all this years there? Thank you!

If I forgot somebody I will be excused. The list is always long: Sorin, Liviu, Sergiu, Roxana, Ioana, Jiorel, Calin, Gicu, Tataie, Arnold, Mizuki, Daniel, Dre, Cecilia, Aura, Corina and many, many others. Thank you for your support and understanding.

The last person which I have to thanks is my future wife, Maria.18 August 2007 Maria and me we will get married in my home town Dej. As thanks all of you are kindly invited to

take part at this celebration. I thank her for all her support and loved. I love you too (sorry, I can not say it in polish).

Personal Information

Name: Bogdan Buhai
Address: Universität Ulm, Sektion Kernresonanzspektroskopie, Albert-Einstein-Allee 11, 89081 Ulm, Germany
Phone: +04 731 5024518
Email: bogdan.buhai@uni-ulm.de
Date of birth: 21.08.1977
Place of birth: Dej, Romania

Education and Professional Activities

1992-1996	“Alexandru Papiu Ilarian” High School, Dej, Romania
1996-2001	Graduate at the Technical University of Cluj-Napoca. Major course of study: Applied Sciences – Physical Engineering
2001	Final study for graduation in the Physics Department of the Technical University of Cluj-Napoca. Diploma thesis: “*The study and the projection of catalytic sensors for liquid petroleum gas*”. Diploma thesis advisor: Lecturer Dr. M. Barlea.
2001-2004	Scientific employee at the Division for Nuclear Magnetic Resonance, University of Ulm, Germany. (Sektion Kernresonanzspektroskopie). PhD Thesis: „ *Investigation of combined electro-, hydrodynamic phenomena in percolation clusters with NMR tomgraphy experiments and CFD simulations*“. Thesis advisor: Prof. Dr. Rainer Kimmich.
2004-2006	Scientific employee (full-time) at the Division for Nuclear Magnetic Resonance, University of Ulm.

Teaching experience

1996-1999	Pedagogic lecture at the Technical University of Cluj-Napoca
2004 SS	Tutor in the seminar „Basics of physics IV“, University of Ulm
2004/05 WS	Tutor in the advanced laboratory course „Methods of Molecular Physics I“, University of Ulm
2005 SS	Technical director of the advanced laboratory course „Methods of Molecular Physics II“, University of Ulm

2005 SS	Assistant Senior in the laboratory course „Basics of Physics I“, University of Ulm
2006 SS	Assistant Senior in the seminar „Basics of Physics IV“, University of Ulm
2006/07 WS	Assistant Senior in the seminar „Basics of Physics I“, University of Ulm

Prizes and awards

2002-2005	PhD Fellowship in the frame of the GRK 328 program of the University of Ulm
2003	Poster Prize at the AMPERE XI NMR School, Zakopane, Poland
2004	“Ernst Award” at the occasion of the joint meeting of the German and British Magnetic Resonance discussion groups, Aachen, Germany

Languages

Romanian (native speaker),

English (very good – spoken, written, comprehension)

German (very good – spoken, written, comprehension)

French (basic knowledge)

Professional Area of Expertise

Construction and design of catalytic sensors for gas detection: 2 years in a private company “Senerg Applied Research”, Cluj, Romania

Nuclear Magnetic Resonance: Magnetic Resonance Imaging

Computer Aided Design (CAD): AutoCad (Certificate released by Autodesk International 1997), Gambit

Computational Fluid Dynamics (CFD): Fluent Suite, Femlab, FIDAP

Programming skills: C++, FORTRAN, IDL (Interactive Data Language)